DESIGN AND CONTROL OF A ROPELESS ELEVATOR WITH LINEAR SWITCHED RELUCTANCE MOTOR DRIVE ACTUATION SYSTEMS

By

Hong Sun Lim

Dissertation submitted to the faculty of the Virginia Polytechnic Institute and State University in partial fulfillment of the requirements for the degree of

Doctor of Philosophy

In

Electrical and Computer Engineering

APPROVED:

Dr. Krishnan Ramu, Committee Chair

Dr. Jamie De La Reelopez

Dr. Douglas K. Lindner

Dr. Daniel J. Stilwell

Dr. Carl L. Prather

March 23, 2007

Blacksburg, Virginia

Keywords: Linear Switched Reluctance Motor, Elevator, Force Distribution Function, Force Control, Current Control, Measurement Disturbance, Disturbance State Observer, Extended State Observer, Nonlinear Controller, Acoustic Noise, EMI

DESIGN AND CONTROL OF A ROPELESS ELEVATOR WITH LINEAR SWITCHED RELUCTANCE MOTOR DRIVE ACTUATION SYSTEMS

By

Hong Sun Lim

Prof. Krishnan Ramu, Chairman

The Bradley Department of Electrical and Computer Engineering

ABSTRACT

Linear switched reluctance motor (LSRM) drives are investigated and proved as an alternative actuator for vertical linear transportation applications such as a linear elevator. A one-tenth scaled prototype elevator focused on a home elevator with LSRMs is designed and extensive experimental correlation is presented for the first time.

The proposed LSRM has twin stators and a set of translator poles without back-iron. The translators are placed between the two stators. The design procedures and features of the LSRM and the prototype elevator are described. The designed LSRM is validated through a finite element analysis (FEA) and experimental measurements. Furthermore, a control strategy for the prototype elevator is introduced consisting of four control loops, viz., current, force, velocity, and position feedback control loops. For force control, a novel force distribution function (FDF) is proposed and compared with conventional FDFs. A trapezoidal velocity profile is introduced to control vertical travel position smoothly during the elevator's ascent, descent, and halt operations. Conventional proportional plus integral (PI) controller is used for the current and velocity control loops and their designs are described. The proposed control strategy is dynamically simulated and experimentally correlated. Analytical and experimental results of this research prove that LSRMs are one of the strong candidates for ropeless linear elevator applications.

However, the proposed FDF is assuming that the feedback current signals are ideal currents indicating actual phase currents without any measurement disturbances mainly arising from sensor noise, DC-link voltage ripple, measurement offset, and variations in the plant model. Meanwhile, real control systems in industry have measurement disturbance problems. Phase current corrupted by measurement disturbances increases torque or force ripple, acoustic

noise and EMI. Therefore, this dissertation also presents a novel current control method to suppress measurement disturbances without extra hardware.

The controller is based on an extended state observer (ESO) and a nonlinear P controller (NLP). The proposed method does not require an accurate mathematical model of system and can be implemented on a low-cost DSP controller. The proposed ESO is exploited to estimate the measurement disturbances on measured phase currents, and the proposed NLP compensates for the measurement disturbances estimated by the ESO. The performance of the proposed current control is validated through extensive dynamic simulations and experiments. Moreover, this rejection of measurement disturbances results in a reduction of force ripple and acoustic noise. Due to superior and robust current control performance, it is believed that the proposed method can be successfully applied into other motor drive systems to suppress measurement disturbances with the same promising results without extra hardware.

Trust in the Lord with your all heart
And do not lean on your own understanding.
In all your ways acknowledge Him,
And He will make your paths straight.
(Proverbs 3:5-6)

ACKNOWLEDGEMENTS

This dissertation is the result of three and half years of work and I have been accompanied and supported by many people. It is a pleasant aspect that I now have the opportunity to express my sincere gratitude to all of them.

I would like to express my deep and sincere gratitude to my advisor, Dr. Krishnan Ramu for his invaluable support and encouragement throughout my Ph.D. course. He is very enthusiastic and motivated as well as a creative person, seeking only high quality work. His continued guidance and incomparable advice helped me a lot in staying on the right track. Thanks to him I could successfully finish this dissertation in less than four years. I owe him lots of gratefulness.

Special thanks must also go to Dr. Jamie De La Reelopez, Dr. Douglas K. Lindner, Dr. Daniel J. Stilwell, and Dr. Carl L. Prather for their concerns and efforts in reading and providing me with valuable comments on this research and the framework of this dissertation. Their generous encouragement and support has been a great source of inspiration.

My colleagues in the Center for Rapid Transit Systems deserve my sincere thanks for their kind help in developing the ropeless LSRM elevator: Nimal Lobo, Keunsoo Ha, Cheewoo Lee, Jaehyuck Kim, and Ethan Swint. Especially I would like to thank Nimal who substantially contributed to the design and development of the elevator in Chapter 2. I cannot imagine the result of this work without his genuine help.

I wish to extend my warmest thanks to Dr. Han-Kyung Bae for his generous help and valuable advice during developing and testing of the elevator. He used to spend a long time on the phone discussing some hardware and software issues on the DSP controller.

I gratefully acknowledge the Naval Postgraduate School, NPS for the financial support and Dr. Leonard A. Ferrari at NPS for his kind assistance and help.

I owe my deep and loving thanks to my wife Suk Jin, my son Su Min, and my daughter Da Min. They are my joy, comfort and best friends. They give me strength and encouragement when I feel tired and discouraged. I thank them for being with me all the time and for understanding me during difficult times. Without them, I could not finish this work. I also feel a deep sense of gratitude to my mother who has been left alone since my father passed away when I was in high school. I know that she prays for me and my family every single day. I cannot find any words to express my heartfelt gratitude to her. I am also greatly indebted to my in-laws who have always kept me in their prayers and been a constant support.

Before concluding, I cannot forget the One who showed me the way to eternal life through Jesus Christ who died on the cross for my sin and rose again. He is my God the Father. He has guided and provided me with all I needed. He has made a wonderful way for me throughout these three and half years. I believe that He will make a new way for me and work in ways I cannot see. All honor and glory be unto Him!

God will make a way,
Where there seems to be no way
He works in ways we cannot see
He will make a way for me
He will be my guide
Hold me closely to His side
With love and strength for each new day
He will make a way, He will make a way.

By a roadway in the wilderness, He'll lead me
And rivers in the desert will I see
Heaven and earth will fade
But His Word will still remain
He will do something new today.

By Don Moen

Hong Sun Lim.

March 23, 2007
Blacksburg, Virginia

TABLE OF CONTENTS

LIST OF FIGURES

LIST OF TABLES

NOMENCLATURE

Symbol	Description (Abbreviation)
BDO	Binary Disturbance Observer
EMF	ElectroMotive Force
ESO	Extended State Observer
FEA	Finite Element Analysis
LSRM	Linear Switched Reluctance Machine
MMF	MagnetoMotive Force
NLP	Nonlinear Proportional Controller
PI	Proportional-Integral
PID	Proportional-Integral-Derivative
PWM	Pulse Width Modulation
RSRM	Rotating Switched Reluctance Machine
SMO	Sliding Mode Observer
SRM	Switched Reluctance Machine

Symbol	Description (Chapter 1)	Unit
i_k[1]	Instantaneous phase winding current	A
w_{sp}	Stator pole width of LSRM	m
w_{ss}	Stator slot width of LSRM	m
w_{tp}	Translator pole width of LSRM	m
w_{ts}	Translator slot width of LSRM	m
x	Position	m
I_p	Peak phase winding current	A
F_e, F_{ek}	Total and phase propulsion force	N
F_{mot}, F_{reg}	Motoring and regenerative electromagnetic force	N
L_k	Inductance of each phase winding	H
$\frac{\partial L_k}{\partial x}$	Changing rate of self inductance with respect to position	H/m

[1] $k=a,b,c,d$

Symbol	Description (Chapter 2)	Unit
a_a	Acceleration of the translator	m/s^2
a_c	Cross-section area of a conductor in the winding	m^2
a_d	Deceleration of the translator	m/s^2
d_c	Diameter of a conductor in the winding	m
f	Frequency	Hz
f_f	Form factor or packing factor	
g	Air gap length	m
h_r	Height of the rotor pole	m
h_s	Height of the stator pole	m
i_{ac}	Phase A core loss currentwinding resistance	Ω
i_m	Magnetizing current	A
k	Ratio of the stack length of core lamination to the bore diameter	
k_1	$\pi^2/120$	
k_2	Variable dependent on the operating point ($=1-L_u/L_a^s$)	
k_d	Duty cycle ($=\theta\cdot m\cdot N_t/360$)	
k_e	Efficiency of SRM	
m	Number of phases	
n	Total number of stator poles of the LSRM	
t_a	Acceleration time of the translator	s
t_d	Deceleration time of the translator	s
v_m	Maximum linear velocity	m/s
w	Thickness of the wedge to hold the phase windings	m
β_s	Stator pole angle of the RSRM	° (Degree)
β_r	Rotor pole angle of the RSRM	° (Degree)
ϕ	Magnetic flux	Wb
λ	Flux linkage of the phase winding	Wb·Turn
θ	Power factor angle	° (Degree)
θ_c	Core loss angle	° (Degree)
μ_0	Permeability of the free space	H/m

A_g	Cross-section area of the air gap during the pole alignment	m^2
A_r	Cross-section area of the rotor pole	m^2
A_s	Cross-section area of the stator pole	m^2
A_{sp}	Specific electric loading	AT/m
A_y	Cross-section area of the stator yoke	m^2
B_g	Flux density of the air gap	T
B_s	Flux density of the stator pole	T
C_{ry}	Thickness of the rotor yoke	m
C_{sy}	Thickness of the stator yoke	m
D	Bore diameter of the RSRM	m
D_o	Outer diameter of the RSRM stator lamination	m
F_a, F_d, F_f	Instantaneous acceleration, deceleration, and friction forces	N
F_{ea_max}	Maximum phase A propulsion force	N
F_{err_max}, F_{err_min}	Maximum and minimum propulsion forces	N
FF	Winding fill factor	
H_g	Magnetic field intensity in the air gap	A/m
I_p	Peak phase winding current	A
J	Maximum allowable current density in the winding	A/m^2
L	Stack length of the magnetic core laminations of the RSRM	m
L_{a_max}, L_{a_min}	Maximum and minimum phase A inductance	H
$L_k(i_k,x)$	Inductance for one phase with all magnetic flux paths	H
L_m	Magnetizing inductance	H
L_t	Total length of the LSRM stator (track)	m
L_u	Unaligned inductance per phase	H
L_w	Stack length of the magnetic core laminations of the LSRM	m
M	Mass of the translator assembly or vehicle	Kg
N_h	Number of horizontal layers of the phase winding	
N_r	Rotating speed of the RSRM	rpm
N_s	Number of stator poles of the RSRM	
N_{sc}	Number of stator sectors of the LSRM	
N_t	Number of rotor poles of the RSRM	

N_v	Number of vertical layers of the phase winding	
P	Maximum power capacity of the LSRM	W
R_a	Phase A winding resistance	Ω
R_c	Phase A core loss resistance	Ω
T_{ph}	Number of winding turns per phase	Turns
V_c	AC Voltage across the inductance	V
V_{as}	AC Voltage source	V
W_s	Stored energy in the magnetic field	Joule

Symbol	**Description (Chapter 3)**	**Unit**
f_k	Torque distribution function	
g_k	Force function	
$i_k^* \, (i_k)$	Commanded (actual) phase current	A
p_{ik}	Instantaneous phase input power	W
p_{ak}	Air gap phase input power	W
v_k	Phase voltage	V
θ	Mechanical angular displacement or rotor position	° (Degree)
$\omega^* \, (\omega)$	Commanded (actual) angular speed	rpm
ω_c	Current loop bandwidth	rad/s
ω_v	Velocity loop bandwidth	rad/s
$\lambda_k^* \, (\lambda_k)$	Commanded (actual) phase flux linkage	A
ζ_c	Current loop damping ratio	
ζ_v	Velocity loop damping ratio	
C	Friction coefficient	N/m/s
F_L	Load force	N
K_{ic}	Integral gain of the current control loop	
K_{iv}	Integral gain of the velocity control loop	
K_r	Converter gain	V/V

K_{pc}	Proportional gain of the current control loop	
K_{pv}	Proportional gain of the velocity control loop	
K_r	Converter gain	V/V
M	the vehicle mass	Kg
L_k	Phase inductance	H
$\frac{\partial L_k}{\partial i_k}$	Changing rate of inductance with respect to phase current	H/A
R_s	Winding phase resistance	Ω
$T_e^* \left(T_e\right)$	Commanded (actual) electromagnetic torque	N-m
$T_k^* \left(T_k\right)$	Commanded (actual) phase electromagnetic torque	N-m
W_c	Coenergy	joule

Symbol	**Description (Chapter 4)**	**Unit**
b	Constant plant parameter	
$f(\cdot)$	Plant uncertainties	
$fal_i(\cdot)$, $g(\cdot)$	Nonlinear Function	
k_i, α	Nonlinear function gains	
k_{pc}	Constant proportional gain of the NLP current controller without Nonlinear function	
u, u_0	Control input	V
$w(t)$	Unknown external and/or internal mesurement disturbances	
x_i [2]	States	
y	Plant output	
z_i	Estimates of states	
$\beta_{0i,}$	Observer gains	
δ	Error boundary of nonlinear function gains	
K_D	Derivative gain of PID controllers	
K_I	Integral gain of PID controllers	

[2] $i=1,2,3,4$

K_{iv}	Integral gain of the velocity control loop	
K_P	Proportional gain of PID controllers	
K_{pc}	Variable proportional gain of the NLP current controller including Nonlinear function	
L_M	Average phase inductance	H
ΔL	Unknown variation of phase inductance	H
R_M	Average phase resistance	Ω
ΔR	Unknown variation of phase resistance	Ω

CHAPTER 1
INTRODUCTION

1.1 Introduction

Linear motion with rotary motors and linear mechanical interfaces has backlash due to gears and problems such as hysteresis [2]. Linear motors eliminate the need for rotary to linear mechanical interfaces resulting in simpler and robust conversion of electrical input into linear motion [7]. With linear motors additional benefits of quietness and reliability are obtained. Consequently, linear motors have been gaining considerable interests and have been applied in conveyor systems, people mover, sliding doors, and air port baggage handling, to mention a few [3].

The linear technologies with different motors have been also explored for the vertical applications such as an elevator application [13]-[19] because conventional traction geared rope elevators have many drawbacks in case of the skyscrapers of 200-400 meters high. With conventional elevators, the space occupancy of the total floor space would be more than 30 percent in 250 meters-high building [4]. Furthermore, the rope is mostly steel wire and causes control problems for the much higher building of more than 500 meters due to its mass and vertical vibration and so on. In this respect, linear electric motors are suitable for the vertical applications with less limitation on height of building and space occupancy.

In recent years, linear switched reluctance motors (LSRM) have been introduced as an attractive alternative to other linear motors such as linear induction motors and linear synchronous motors because of their simple and robust construction with concentric windings on only one side, stator or translator, and consequently less thermal problem and easy maintenance, and finally low cost. Moreover, the windings are always in series with a switch so that, in case of a shoot through fault, the inductance of the winding can limit the rate of change of rising current and provide enough time to initiate protective relaying to isolate the faults. Further, the phases of the LSRM are independent and even in case of one winding failure, uninterrupted operation of the motor drives is possible although with reduced power output. In other words, a failure in one phase in LSRM or in the converter typically affects only the damaged phase and the other phases can continue to run independently. It shows that LSRM has a high-grade fault tolerance. With these advantages, LSRMs have been emerging in various linear applications recently [5]-[12]. For instance, a horizontal linear transportation system is presented with a new converter topology and force control method using force distribution functions (FDFs) in [5], and a high precision position application such as precision manufacturing automation is introduced with a proposed robust position control strategy in [6]. Reference [7] describes a cylindrical type linear actuator using an LSRM. Lee *et al.* presented a ‘MegLev’ application using LSRM technology in [8] and [11]. Liu *et al.* [12] introduced a micro-LSRM focusing on a microelectromechanical (MEMS) system application.

Furthermore, LSRM technologies have been coupled with various design procedures of LSRMs for each different application [8]–[10]. For a horizontal moving system with levitation actuators, the design procedure of the presented LSRM topology is detailed in [8]. For an manufacturing automation application, a 3-D modeling of an LSRM with magnetic-flux decoupled windings is described in [9]. Moreover, a new LSRM topology focused on a high-force density is presented in [10] and it is a double-sided and double-translator without back iron on the translators and on stator in the middle.

However, up to this point, vertical propulsion applications such as an elevator using LSRMs have remained largely unexplored until a possibility of the vertical transportation system using LSRMs has been researched by the author *et al*. in [1]. The author investigated and proved that LSRM would be an attractive alternative for a full scale ship elevator with a payload of 10,000lb using a suitable LSRM topology as well as an effective force control strategy with a novel FDF method. The LSRM topology proposed in [1] consists of twin stators and no back iron on translators to reduce the mass of translators on a vertical moving vehicle. Meanwhile, linear induction motors and synchronous motors have been already presented in [13]-[14] and [15]-[18], respectively, as primary propulsion of vertical transportation systems. Linear synchronous motors have to use the amateur coil on stator side and permanent magnet on the moving vehicle. Thus, linear synchronous motor is expected to be more expensive and also cause discomfort of passengers due to the strong permanent magnet on the vehicle. In addition, to reduce the high temperature on the permanent magnet below its operating temperature, the vehicle needs to carry a cooling system which increases the mass of the vehicle. Linear Induction motor are also not suitable for elevator applications due to their low efficiency [4]. Linear induction motors have a large air gap and hence sufficient thrust can only be generated with a high current in a secondary conductor. Thus, metallic plates may overheat, even to the point of melting. From these perspectives, LSRMs are very competitive for the vertical applications due to absence of windings on one side, stator or translator. By these advantages, this research has been motivated and successfully accomplished. It will be discussed in detail in this dissertation.

This chapter consists of several sections. In the next two sections, the operation principle of a typical LSRM is described and various configurations of candidate LSRMs for vertical travel applications are presented. Then, earlier research works on control strategies are reviewed, and expected problems in applying LSRM technologies to a vertical propulsion vehicle such as an elevator are defined. Finally, the objectives and contributions as well as the scope of this research are summarized at the end of this chapter.

1.2 Operation Principle

The concept of an LSRM stems from its predecessor: the rotary switched reluctance motor (RSRM). The only difference between the two configurations is that the RSRM produces rotational torque and an LSRM produces linear force. In fact, one can assume an LSRM is merely a “rolled out” version of a RSRM.

A *reluctance motor* is an electric motor in which translational force production occurs by the tendency of the moving part to move towards a separate stationary point where the inductance of the excited winding is maximized. The *switched* aspect describes the switching of winding excitations at different phases to achieve a continual motion. The last and only misleading term in LSRM is *linear*. By no means does an LSRM have any linear characteristics. The only linear aspect of an LSRM is that its translator and stator is laid out in a straight and parallel fashion. For a better understanding of the operation of an LSRM, consider Fig. 1.1 which

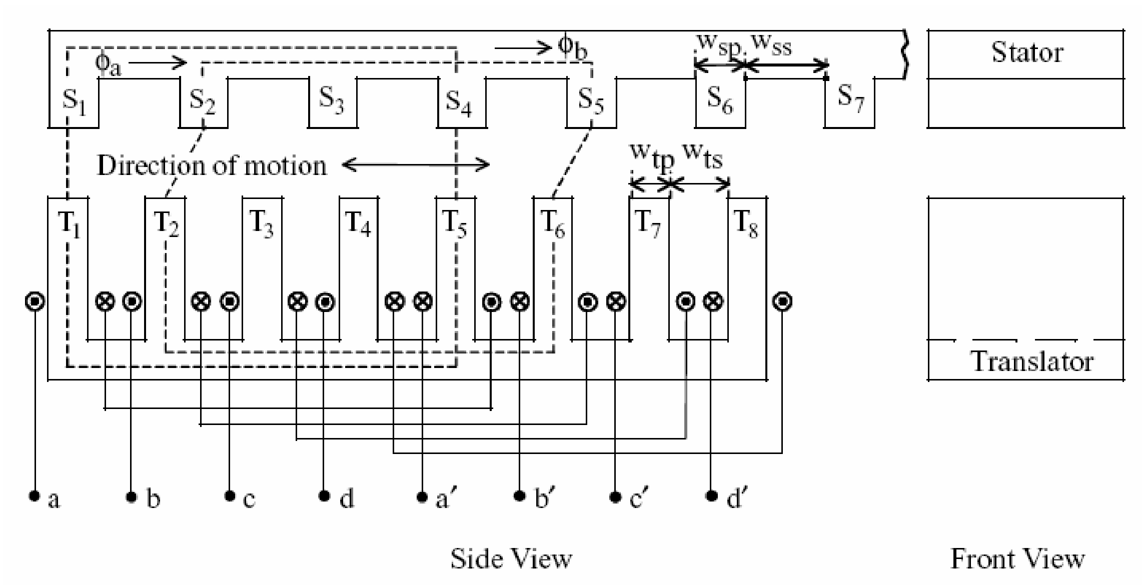

Fig. 1.1 Longitudinal 8/6 LSRM [11]

(Used by permission of Dr. Krishnan Ramu)

depicts an 8/6 design. The numbers represent the number of poles on each rail. Therefore, an 8/6 design means there are 8 poles on the translator (bottom rail) and 6 poles on the stator (top rail). In an LSRM system, the translator is the moving part and the stator is the stationary part. The part that houses the windings is known as the intelligent piece. With the 8/6 design shown, the intelligent piece would be the translator and the dummy piece would be the stator.

A *phase* constitutes a pair of opposite poles that will have its windings excited at the same time. With an 8/6 design, there are four phases. Thus, using the motor shown in Fig. 1.1, poles T1 and T5 represents the first phase (phase A), poles T2 and T6 is the second phase (phase B), poles T3 and T7 is the third phase (phase C), and poles T4 and T8 is the fourth phase (phase D). By having a phase switched on, the generated fluxes become additive and form a complete flux loop. When a phase is said to be in an *aligned position* (or *fully aligned*), the translator poles of that phase are perfectly aligned with the stator poles. In Fig. 1.1, the translator poles of phase A (T1 and T5) is fully aligned with stator poles S1 and S4. The path of the flux during phase A excitation is denoted as 'ϕa'. In the aligned position, the inductance is at its maximum because the magnetic reluctance of the flux is at its lowest. On the other hand, when a phase is not in an aligned position, it is known as *unaligned position*. From Fig. 1.1, phase B is an example of an unaligned position. If the windings of phase B were to be excited at the current state, the translator will develop the tendency to move towards the right until it poles reaches an aligned state. That is, T2 and T6 become aligned with S2 and S5, respectively.

In order for the translator to keep continual motion, the windings of each phase must be *switched* on and off at the correct intervals. Assuming the translator is currently situated as shown in Fig. 1.1 and moving to the right, the correct order of phase excitation is phase B, C, D, A, and repeat. In other words, because phase B in an unaligned state, its inductance is not at its maximum. Therefore, the flux path of phase B (shown as a dashed line labeled as 'ϕb') will move towards the direction in which maximum inductance can be attained. Once phase B becomes fully aligned its windings get switched off and phase C gets switched on. Phase C will then move towards the right to achieve maximum inductance and then get switched off, which prompts phase D to switch on. The whole switching mechanism gets repeated until the translator is at its desired position.

The operation of LSRM is based on the inductance profile of the motor. The inductance of the motor is related to motor dimensions such as the stator and translator pole and slot widths, excitation currents and translator position. Assuming that the magnetic circuit is linear and therefore the inductance characteristics are independent of stator current excitation, a relationship between the motor dimensions and inductance, shown in Fig. 1.2, is derived. The inductance of a phase winding is its self-inductance. Five translator positions are significant to derive the inductance profile and they are given as

$$x_1 = \frac{w_{ts} - w_{sp}}{2}$$

$$x_2 = x_1 + w_{sp} = \frac{w_{ts} + w_{sp}}{2}$$

$$x_3 = x_2 + (w_{tp} - w_{sp}) = w_{tp} + \left(\frac{w_{ts} - w_{sp}}{2}\right) \tag{1.1}$$

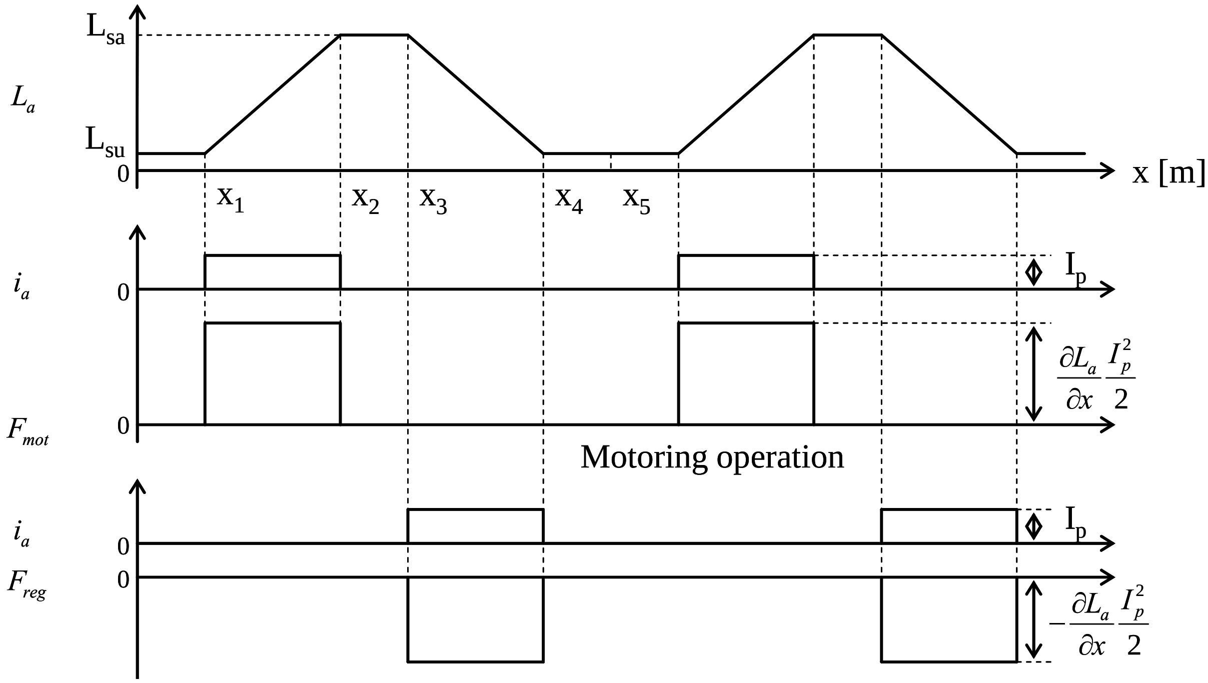

Fig. 1.2 Inductance profile and propulsion force generation in LSRM [11]

(Used by permission of Dr. Krishnan Ramu)

$$x_4 = x_3 + w_{sp} = w_{tp} + \left(\frac{w_{ts} + w_{sp}}{2}\right)$$

$$x_5 = x_4 + \frac{w_{ts} - w_{sp}}{2} = w_{tp} + w_{ts}$$

where w_{tp} is the width of the translator pole, w_{ts} is the width of the translator slot, w_{sp} is the width of the stator pole, and w_{ss} is the width of the stator slot as shown in Fig. 1.1. Between x_2 and x_3, there is complete overlap between stator and translator poles, and inductance during this interval corresponds to the aligned value and is a maximum. As there is no change in the inductance in this region, zero propulsion force is generated in this region with an excitation current in the winding. The phase A propulsion force equation is given by,

$$F_{ea} = \frac{1}{2} i_a{}^2 \frac{\partial L_a(x, i_a)}{\partial x} \tag{1.2}$$

But it is important to have this flat inductance region to give time to commutate the current and hence to prevent the generation of a negative force. The unequal stator and translator pole widths contribute to the flat-top inductance profile. On the other hand, the regions corresponding to $0 \sim x_1$ and $x_4 \sim x_5$ have no overlap between stator and translator poles. These positions have the minimum phase inductance known as unaligned inductance. The rate of change of inductance is zero and hence these regions also do not contribute to propulsion force production.

1.3 LSRM Topologies for Elevator Application

Since most research effort on SRMs has been focused on rotary SRMs, LSRMs have not attracted considerable interests until 1990's. Only a few literatures are available on the research of LSRMs [1], [5]-[12], [19]-[21], [23]-[34], [37]-[40]. Moreover, LSRMs for vertical applications have remained unexplored until the author *et al.* [1] investigated the possibility of applying LSRMs into vertical application as an alternative to conventional linear motors, such as linear induction motors and linear synchronous motors [13]-[18]. For this reason, various possible topologies for vertical applications are shown and discussed in this section.

First of all, earlier design works need to be classified and investigated so that several possible types can be selected as candidates of an elevator application. According to the flux path type, configurations of LSRM are divided into two categories: longitudinal type and transverse type as shown in Fig. 1.3. As a common LSRM configuration, longitudinal flux path type LSRMs have been prevalently selected for research in many literatures [1], [5]-[6], [8]-[12], [19], [26]-[30], [33]-[34], [38]-[40]. Meanwhile, the transverse flux path type LSRMs have been exploited by Takayama *et al.* [24]-[25] and Liu *et al.* [37]. In addition, cylindrical LSRM configurations have been presented by Corda *et al*. [7], [31]-[32].

For vertical applications, however, all conventional LSRM topologies used for horizontal applications are not suitable because vertical travel applications need more compact, lighter moving parts (or translators), lower acceleration, and easier installation to the moving vehicle than horizontal ones. Hence, with these design factors plus control strategies taken into consideration, several candidates for the vertical applications are proposed in this section as shown Fig. 1.4. Among four LSRM configurations shown in Fig. 1.4, Type 1 in Fig. 1.4(a) is most commonly used for linear motion applications as mentioned in the beginning. Type 3 in Fig. 1.4(c) has been designed and experimentally applied to another horizontal travel application [10]. Meanwhile, Type 2 in Fig. 1.4(b) is a configuration which combines two translators back-to-back and needs one more stator and has not been tried yet in any applications.

Since translators are moving parts of the LSRM and have to be installed on a moving vehicle, the weight of the translators has to be considered as an important design factor. As discussed by the author *et al.* [1], the previous topologies from Type 1 to Type 3 cannot meet specifications for vertical travel applications, such as an elevator: Type 1 is most robust configuration, but it needs long stack (depth of translators) length and windings to produce a required propulsion force. The long stack length increases the mass of translator and windings, and decreases force density (propulsion force per mass). Hence, Type 1 is too heavy to be applied to vertical moving parts. Type 2 is just like Type 1, but it is more compact configuration than Type 1. Concerning Type 3, it needs more parts (translators and stators without back iron) and causes much complicate construction work although it is high force density configuration. For that reason, the author *et al.* [1] proposed a new topology, Type 4, and it is verified as the most suitable configuration for vertical applications in terms of force density, mass of translators including windings and normal force generated between translators and stators, and requires relatively simple construction work compared with Type 3. The more details about four different candidates are discussed in [19]. As a result, Type 3 is chosen and exploited as the LSRM configuration for an elevator application for this research.

1.4 State of the Art

LSRM Topology for Vertical Applications: In earlier works, LSRMs have been commonly exploited for horizontal applications [5]-[8], [11]-[12], while other linear motors have already been explored in vertical travel application [13]-[18]. However, conventional LSRM configurations shown in literature [5]-[11], [24]-[34], [37]-[40] are not suitable for vertical applications due to heavy mass of moving parts (translators), low force density

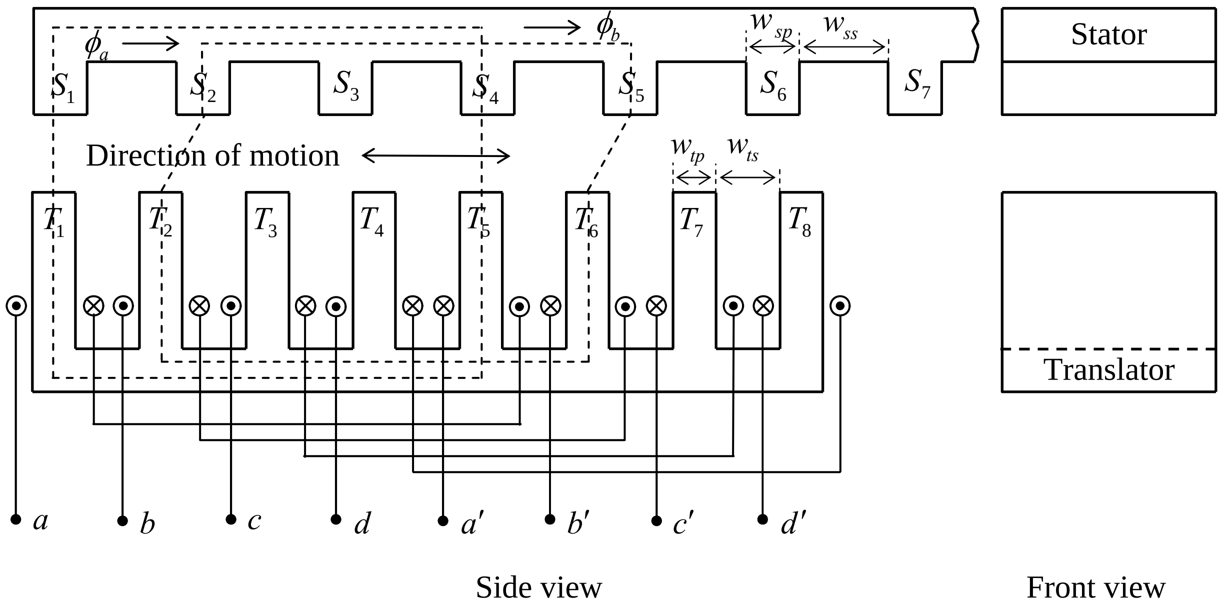

(a) Longitudinal LSRM configuration.

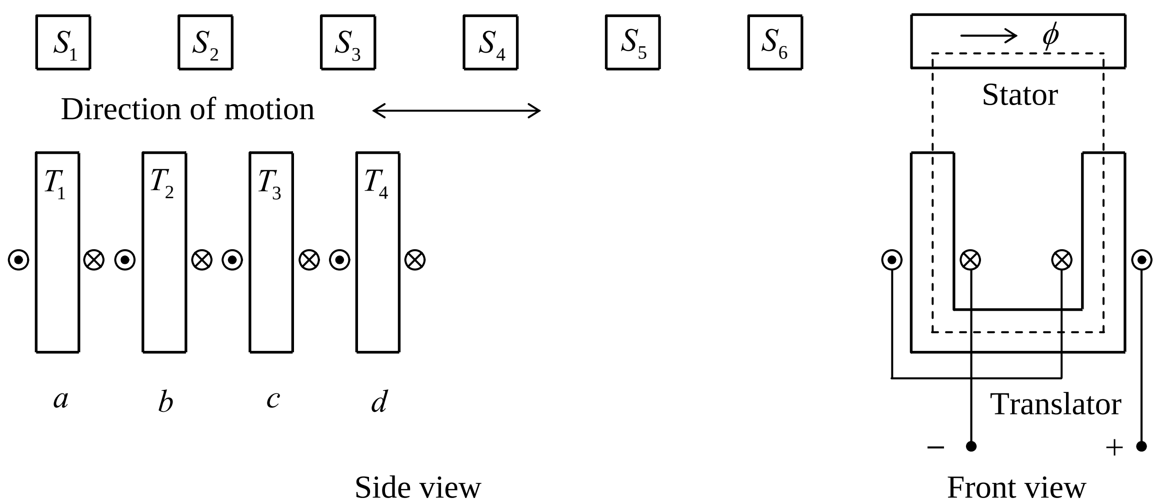

(b) Transverse LSRM configuration.

Fig. 1.3 LSRM configurations according to flux path type: Longitudinal and Transverse type [11] (Used by permission of Dr. Krishnan Ramu)

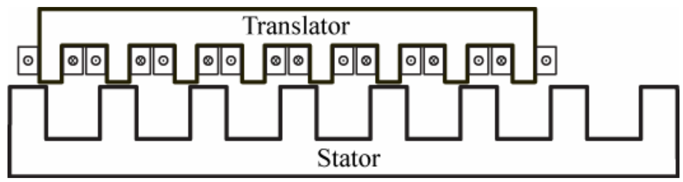

(a) TYPE 1

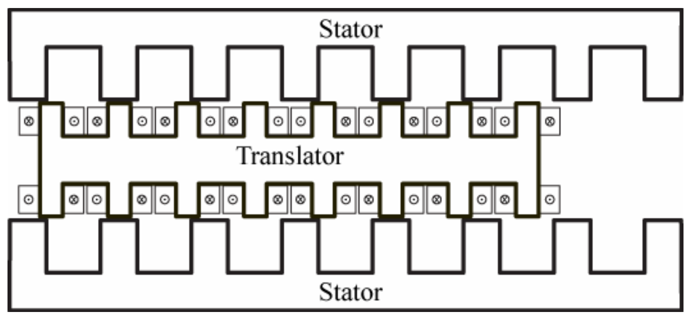

(b) TYPE 2

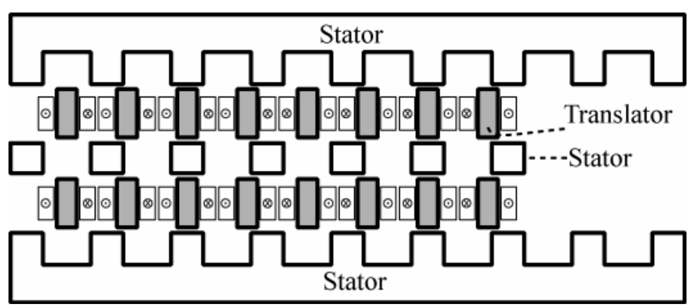

(c) TYPE 3

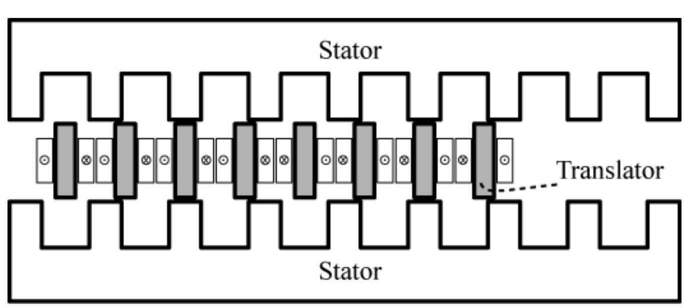

(d) TYPE 4

Fig. 1.4 LSRM topologies for an elevator application (propulsion force per moving part mass) and complexity of construction [10], and hence a new LSRM topology for vertical travel application is required. In addition, vertical travel applications need only two-quadrant operation (motoring, positive breaking) due to the acceleration of gravity while horizontal applications needs four-quadrant operation (motoring, regenerating or breaking) without the effect of the acceleration of gravity. Two-quadrant operation needs to be considered as one of important design factors and needs symmetric force profiles as presented by the author *et al.* in [1].

Corda *et al.* [7] shows that LSRM has a very high normal force of attraction between stator and translator poles while rotary SRMs have the normal force neutralized by same force acting between the diametrically opposite pair of stator and rotor poles. The high normal force is a serious mechanical problem to be considered at the design stage of LSRM construction structure for vertical travel application so that the normal force might be significantly reduced or cancelled by strong mechanical structure or symmetric normal force like rotary SRMs. In addition, installation problem needs to be included in some ways that the flux path in translators is not blocked and at a same time the total mass of translators is light since translators will be mounted on the moving vehicle as active parts of LSRMs.

Force Control: From the literature of Ishii [4], one of serious problems in conventional traction geared rope type elevator is vertical vibration which is mainly caused by torque ripples of electric motors. Since LSRMs have been known for high force ripple, force ripple must be suppressed to apply LSRMs to an elevator application. For this goal, several control strategies have been proposed in [5], [6], [21], [36], and [41]-[45]. The basic idea is to distribute the desired propulsion force to two adjacent phases during predetermined commutation interval using the force distribution function (FDF). Based on inductance profiles, Schramm *et al.* [21] proposed the phase current optimal profiling in the sense of minimum stator copper loss. Due to the finite bandwidth of current control loop, significant torque ripple accompanied this control scheme during commutation. Husain *et al.* [41] and Ilic-Spong *et al.* [42] introduced a sinusoidal function and an exponential function as a torque (or force in LSRMs) distribution function, respectively. Wallace *et al.* [43] and Gan *et al.* [6] used a simple function of linearly increasing outgoing phase currents and linearly decreasing incoming phase currents during commutations accepting possible torque (or force) error. Kim *et al.* [44] proposed a torque distribution function, which could minimize the rates of change of currents over commutation intervals. Recently, Bae *et al.* [5] and [36] propose an efficient FDF using the rate of change of inductance and its combination, and successfully applied the proposed FDF into a rotary SRM as well as LSRMs. However, there is a problem in adopting Bae *et al.*'s FDF because inductance of LSRMs for an elevator application is too high to apply the proposed nonlinear FDF function. The FDF function renders the phase current not to respond fast enough to track the current command. As a result, to the contrast of the horizontal LSRM application presented in [5] and [11], force ripple in case of vertical LSRM applications is very high when the FDF is used and the results are presented in [1]. Therefore, the need of a new force control method has emerged to diminish the force ripple during commutation, and hence to make LSRMs competitive and suitable primary propulsion source of a linear elevator.

Current Control: Current control is very important because propulsion force is generated directly by phase line currents as given in Eq. (1.2). Current controllers in LSRMs have been developed with various control techniques [47]-[50]. Bae *et al.* [47] and [48] proposed a new converter switching scheme to reduce the current (and force) ripple using a unipolar converter switching method with the decoupling of the induced emf and a new dynamic FDF model with mutual inductance considered, respectively. Lin *et al.* [49] proposed a high performance current control using on-line parameter estimation to adjust the current control gain according to the estimated inductance value. Wei *et al.* [45] introduced another current ripple reducing methods called PSCC, 90-degree phase-shift current control. It is similar to Bae *et al.* [48] in the sense of increasing the chopping frequency by double without increasing physical converter switching frequency. The difference is that Wei *et al.* directly changed the DSP register value according to the operation mode to make the switching strategy possible. Meanwhile Bae *et al.* made a virtual opposite sign of voltage command to the actual voltage command from the current error and effectively doubled the switching frequency. These current control schemes, however, do not take into account uncertain or unmodeled parameters, such as noise and offset of current sensors; switching noise of PWM converter; DC-link ripple; voltage drop of switching devices; and variations in plant model parameters. These uncertain and unmodeled parameters are called measurement disturbances in this research. Phase currents corrupted by measurement disturbances cause conventional current controllers to generate line currents with large ripples, and hence to make undesirable force ripples as presented by the author *et al.* [46]. Moreover, the noisy currents increase acoustic noise, which is one of main drawbacks of (L)SRMs. Therefore, the effect of measurement disturbances on current control should be analyzed by way of simulations and experiments. Based on the analysis, an effective and robust current control method needs to be presented to compensate for undesirable measurement disturbances so that LSRM actuation systems are more reliable and become acceptable for propulsion applications.

In addition, the current controllers described in [48] and [50] use a variable control gain in proportional plus integral (PI) controller to achieve high performance SRM drives. Variable control gains need accurate nonlinear motor parameters, such as inductance with respect to position and current. Thus, if the stored or estimated motor parameters are not correct, the controller cannot work properly and sometimes can cause high peak currents, resulting in damage of control systems and motors. In case of elevator applications, this problem should be avoided. In this respect, an efficient model-independent nonlinear controller needs to be taken into account to achieve reliable control system as well as easy implementation.

1.5 Objectives and Contributions

A Prototype Ropeless LSRM Elevator Development: Earlier reviews provide that many electrically propelled linear actuation systems normally use either linear induction or linear synchronous motors. LSRMs, however, have many advantages over the conventional linear motors: low manufacturing cost, more reliable, fault tolerant motor topology, less thermal problem, and easy maintenance. These advantages make LSRMs very attractive alternative to the other linear motors and hence very competitive candidates for vertical transportation applications as well. Nonetheless, LSRMs have remained unexplored for vertical applications while there are many literatures about horizontal transportation applications. In this regard, the design, analysis and development of a prototype LSRM for a vertical application such as an elevator are very valuable and hence are presented in this dissertation. This study is the first of its kind to propose and investigate the feasibility of the linear elevator using LSRMs with a novel force control strategy.

Novel Measurement Disturbance Rejection Current Control: Conventional current controllers do not consider the effect of corrupted phase currents due to the measurement disturbances, mainly arising from noise and offset of current sensors, switching noise of PWM converter, DC-link ripple, voltage drop of switching devices, and variations in plant model parameters. Measurement disturbances, however, need to be seriously taken into account and analyzed to enhance performance and robustness of current and force control, and hence to improve reliability of LSRM actuation systems. Moreover, to achieve high performance current control PI current controllers use variable P gains which include variable nonlinear motor parameter of self-inductance with respect to position and phase current. As discussed in previous section, a model-dependent controller is not desirable in the sense of reliability and implementation of control methods. Therefore, a new model-independent current control method using an extended state observer (ESO) and a nonlinear P controller (NLP) is proposed to estimate measurement disturbances and compensate for it. As a result, it is expected to enhance current and force control performance. Furthermore, acoustic noise and EMI are expected to decrease because of ripple reduction in force and current.

Research work in this dissertation makes the following contributions.

1) The most suitable four-phase (8/6) LSRMs with four 1.06-m-long stators and 1.5mm air gap between stators and translators for a prototype elevator is chosen, designed and implemented. The analyses on four candidates of the LSRM topology for this application are detailed in [19]. Features of the designed LSRMs are also described according to each part: translator and stator.

2) A prototype elevator with a size of 22 x 26 x 50 inches using the designed LSRMs is developed and presented. It consists of two LSRMs whose windings are connected in series, and the LSRM has been installed on each side to make the vertical moving system more stable and tolerant compared with one side actuated system. Setup and structure for the prototype elevator are described according to each part with pictures.

3) A superior force control technique with a novel FDF method for the prototype elevator is derived, implemented, and proved by way of dynamic simulations and experimentas.

4) PI controllers for the current control loop and velocity control loop are described, analyzed, employed, and validated through dynamic simulations and experiments. For position control, a trapezoidal velocity profile is applied during moving as well as halt.

5) A novel and model-independent current controller to reject measurement disturbances contained in phase currents is proposed, analyzed and validated through dynamic simulations and experiments. It is based on an extended state observer (ESO) and nonlinear P controller (NLP). The convergence proof of the proposed current control is derived in the Appendix B. It is believed that the proposed current control method can be successfully applied into other motor drive systems in the presence of measurement disturbances.

6) The prototype LSRM elevator is demonstrated successfully at different velocities from 0.15m/s to 0.3m/s as well as with different payloads of 23kg and 32kg including the vehicle mass. The correlation between dynamic simulations and experimental results is established.

7) A DSP-based control system has been realized to execute the control strategy for the prototype LSRM elevator. An asymmetric half bridge power converter for each phase is used, adopting a unipolar switching strategy presented in [47] and [48].

1.6 Scope and Organization

Scope of This Research

The present study has the following scope:

(a) The designed elevator is a prototype to validate that the LSRM technology is an attractive alternative to conventional linear motors, such as linear induction and linear synchronous motors for vertical applications. For the prototype elevator, any break systems at stop or in case of failure of power supply are not provided because comparison and validation can be achieved during operation of ascent and descent. In the future study, safety tests with break systems need to be explored for industrial applications.

(b) The surface of the stator poles is not perfectly flat due to welding of laminations. As a result, the air gap between stators and translators is not constantly maintained at 1.5mm in all travel position from bottom to top during ascent and descent of the vehicle. In this research, the comparison between dynamic simulations and experimental results assumes that the air gap is 1.5mm in all travel position.

(c) At the design stage of the LSRM, the normal force was not considered. Due to high normal force, however, stators tend to bend inwardly toward translators. The air gap between stators and translators is heavily affected by the normal force during operation. The prototype LSRM uses metal pieces to connect four stators to rigid elevator structure frames on each side so that the air gap can be maintained at 1.5mm during operation. Thus, it is assumed that the air gap is not affected by the normal force in this study.

Organization of This Dissertation

This dissertation is organized as follows. Chapter 2 describes a design procedure of a suitable LSRM topology for two different elevator applications, and shows correlation between simulation results of finite element analysis (FEA) and measurement data of the LSRM in terms of force and inductance. Chapter 3 presents control strategies for the prototype: PI velocity control with a velocity profile, force control with a novel FDF method and PI current control with gain scheduling with respect to position. In addition, it explains converter topologies and a unipolar switching strategy applied for the prototype LSRM elevator. Dynamic simulations with the control strategies are presented at the end of the chapter. In Chapter 4, a novel and robust current control algorithm is proposed to reject measurement disturbances contained in phase feedback currents. It consists of a proposed extended state observer (ESO) and nonlinear P controller (NLP). The proposed control method is verified by dynamic simulations and experiments. In addition, FFT analysis results are provided to prove reduction of acoustic noise and EMI effect. Chapter 5 provides a comprehensive summary of the major conclusions arising from this research work. The chapter ends with some suggestions on possible areas of further research work. Appendix A describes the derivation of the proportional and integral gains of the system presented in [47]. Appendix B derives the convergence proof of the proposed control algorithm based on the proposed ESO and NLP. In Appendix C, the specifications of the prototype LSRM elevator used in the research are given.

CHAPTER 2
DESIGN OF A LINEAR SWITCHED RELUCTANCE MOTOR FOR A ROPELESS ELEVATOR

A design procedure for a double-sided and longitudinal flux-based linear switched reluctance motor (LSRM) with no back-iron (yoke) in translators shown in Fig. 2.1 is developed for a prototype elevator in this chapter. The design procedure introduced by Lee *et al.* [8] is adopted to design the LSRM for the prototype elevator. The design procedure of Lee *et al*. utilizes the rotating switched reluctance motor (RSRM) design by converting the specifications of the linear motor into an equivalent rotating motor. The motor design is carried out in the rotary domain, which then is transformed back into the linear domain. Such a procedure brings to bear the knowledge base and familiarity of the rotary motor designers to design a linear motor effectively. This chapter contains one illustration of the given design procedure which was applied for a LSRM design for a ship elevator presented by the author *et al.* [1]. For a scaled-down prototype elevator, the dimensions from the designed LSRM for a ship elevator are shrunk and optimized into final dimensions of what is shown in this chapter. The designed LSRM is verified with finite element analysis (FEA) prior to construction of the prototype. Experimental correlation in the form of inductance vs. position vs. current and propulsion force vs. position vs. current is given to validate the analysis and design procedure in this chapter.

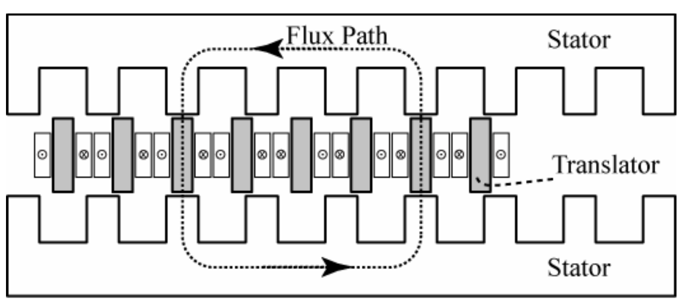

Fig. 2.1 Double-sided and longitudinal flux-based 8/6 type LSRM

2.1 Introduction

As reviewed in Chapter 1, there are two distinctive configurations of LSRMs: longitudinal type and transverse type as shown in Fig. 1.3 of the previous chapter. As a common LSRM configuration, longitudinal flux path type LSRMs have been prevalently selected for research in many literatures [5]-[6], [8]-[12], [19], [26]-[30], [33]-[34], [38]-[40]. On the other hand, the transverse flux path type LSRMs have been explored by Takayama *et al.* in [24] and [25], and Liu *et al.* in [37]. In addition, cylindrical LSRM configurations have been presented by Corda *et al*. in [7], [31], and [32].

For vertical applications, however, all conventional LSRM topologies used in horizontal applications are not suitable because vertical travel applications need more compact, lighter moving parts (or translators), lower acceleration, and easier installation to a moving vehicle than horizontal ones. With these design factors plus control strategies taken into consideration, a four-phase double-sided and longitudinal flux-based (8/6) type LSRM with active translators is proposed as the most suitable LSRM topology for the vertical applications. The details concerning the design and analysis and comparison results of candidate LSRM topologies are presented by Nimal *et al.* in [19]. The proposed LSRM is shown in Fig. 2.1 and was originally presented by the author *et al.* in [1].

On the design procedure of LSRM, there had not been a standard design procedure for LSRM [35] until Lee *et al.* proposed a new LSRM design procedure in [8]. A standard or classical design procedure begins with the power output equation relating the motor dimensions such as the bore diameter, lamination stack length, speed, magnetic loading, and electric loading. Further, the motor dimensions and their impact on performance are characterized by implicit relationships and made available in a form to enable motor design. Such a procedure allows an insight into the scaling of designs and enables the exercise of engineering judgment to select the best design with least amount of computations. These advantages are not feasible with finite element analysis (FEA). Therefore, a standard design procedure is selected for the prototype LSRM design.

Recognizing that a standard design procedure is available for a rotary SRM [51], the design of a LSRM can proceed via a rotary SRM if design specifications can be transformed from linear to rotary domain. Then the design can be recovered in linear domain by simple algebraic transformations from rotary domain to linear [8].

As discussed in the previous chapter, elevator applications, however, need a symmetric force profile due to two-quadrant operation, motoring and breaking, which is not considered for conventional horizontal travel applications. In vertical travel applications, the acceleration of gravity is always present and it acts a negative force pulling the moving vehicle down all the time during operation. As a result, LSRMs have to produce only positive force to run the moving vehicle at desired speeds whether the vehicle ascends (positive velocity, motoring operation) and descend (negative velocity, breaking operation). The standard design procedure introduced by Lee *et al.* does not consider this two-quadrant operation effect because it uses the conversion method from RSRM to a conventional type of LSRM. For this reason, The author *et al*. [1] proposed a wider stator pole width (‘w_{sp}’ in Fig. 1.1) without changing other dimensions to make a propulsion force profile symmetric once conventional LSRM dimensions are given by the standard LSRM design procedure.

2.2 LSRM Design Procedure

It describes the standard LSRM design procedure presented by Lee [11]. Design of LSRM is achieved by first translating its specifications into equivalent rotary SRM specifications. Then a rotary SRM is designed from which an LSRM dimensions and design variables are recovered by inverse translation. The design procedure is derived in this section according to Lee’s work presented in [11].

2.2.1 Specifications of the LSRM

The LSRM is to be designed for a motor stator length L_t, with a maximum linear velocity of v_m and an acceleration time t_a required to reach the maximum velocity. The maximum mass of the translator is restricted to M_t. Fig. 2.2 shows the required velocity profile of the LSRM. If the deceleration time $t_d = t_a$, the maximum acceleration is given by,

$$a_a = \frac{v_m}{t_a} \tag{2.2}$$

and the maximum deceleration $a_d = -a_a$. The instantaneous acceleration force F_a is given by,

$$F_a = M_t \cdot (a_a + a_g) \tag{2.3}$$

where a_g is the acceleration of gravity, $9.8 m/s^2$. On the other hand, the instantaneous deceleration force is given by,

$$F_d = M_t \cdot (a_d + a_g) \tag{2.4}$$

Assuming a zero instantaneous friction force, that is, $F_f = 0$, the maximum power capacity of the LSRM is given by,

$$P = F_a \cdot v_m \tag{2.5}$$

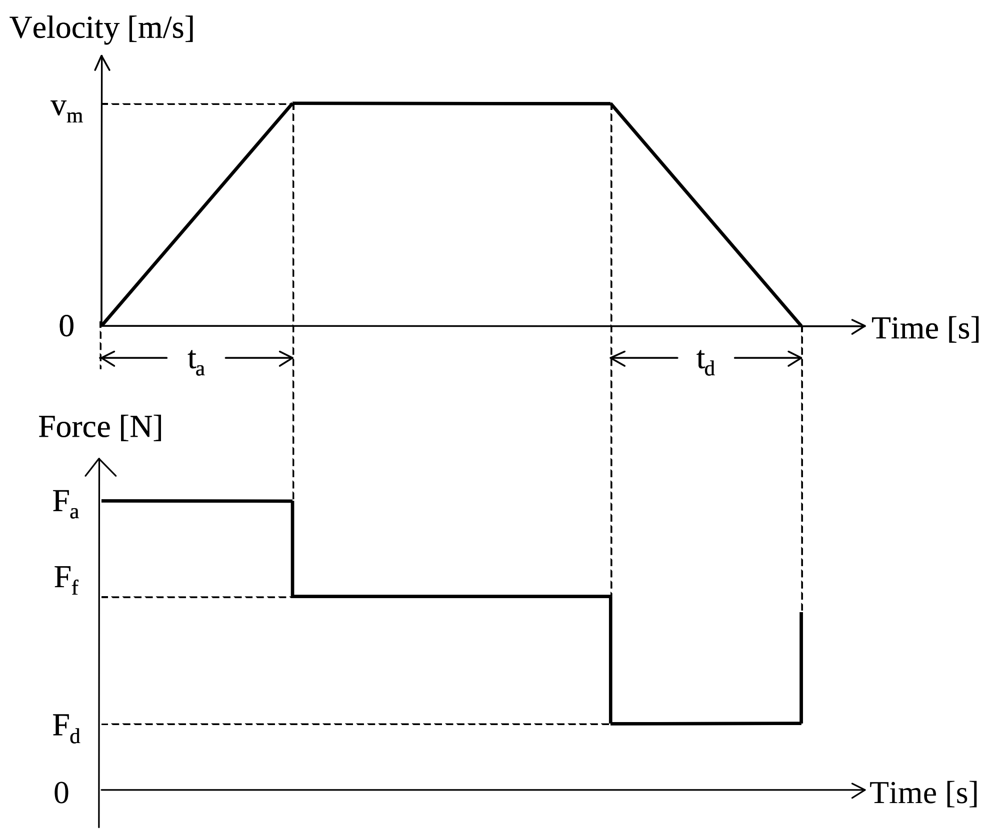

Fig. 2.2 Velocity and required force profiles of LSRM for an elevator application.

2.2.2 Design of Rotary SRM (RSRM)

An 8/6 RSRM is designed for a power capacity identical to that of the LSRM. The material is ASTM-A1011 for stator with lamination and CF1018 for translator without lamination. The RSRM has a stator pole angle of β_s and a rotor pole angle of β_r. The speed of the RSRM, N_r, in rpm, is given by,

$$N_r = \frac{v_m}{D/2} \cdot \frac{60}{2\pi} \tag{2.6}$$

where D is the bore diameter of RSRM. The power output equation of a RSRM in terms of key physical variables [46], is described by,

$$P = k_e k_d k_1 k_2 B_g A_{sp} D^2 L N_r \tag{2.7}$$

where P is the power output, k_e is the efficiency, k_d is the duty cycle determined by the current conduction angle for each rising inductance profile, $k_1 = \pi^2/120$, k_2 is a variable dependent on the operating point and is determined by using aligned saturated inductance and unaligned inductance, B_g is the flux density in the air gap at the aligned position, A_{sp} is the specific electric loading which is defined as ampere conductor per meter of stator inner periphery, L is the stack length of the magnetic core, and N_r is the speed. Setting the stack length as a multiple or sub-multiple of the bore diameter,

$$L = kD \tag{2.8}$$

and converting the rotational angular velocity to linear velocity,

$$\begin{aligned} P &= k_e k_d k_1 k_2 B_g A_{sp} D^2 \cdot kD \cdot \left(\frac{v_m}{D/2} \cdot \frac{60}{2\pi} \right) \\ &= k_e k_d k_1 k_2 k B_g A_{sp} D^2 v_m \frac{60}{\pi} \end{aligned} \tag{2.9}$$

The bore diameter is obtained from the power output equation as,

$$D = \sqrt{\frac{P\pi}{60 \cdot k_e k_d k_1 k_2 k B_g A_{sp} v_m}} \tag{2.10}$$

The air gap of the LSRM is usually much larger than that of the RSRM. In the aligned portion, the *B-H* characteristic of the magnetic material is fairly linear and the reluctance of the steel core is small when compared to the reluctance of the air gap in the aligned position. The motor flux linkage can be calculated as,

$$\phi = B_g A_g \tag{2.11}$$

where A_g is the cross-section area of the air gap and during alignment is approximately equal to,

$$A_g = \left(\frac{D}{2} - g\right)\left(\frac{\beta_r + \beta_s}{2}\right) L \tag{2.12}$$

where g is the length of the air gap. The magnetic field intensity in the air gap can be calculated as,

$$H_g = \frac{B_g}{\mu_0} \tag{2.13}$$

Assuming the existence of a large air gap, the ampere-turns required to produce the air gap magnetic field intensity is given by,

$$T_{ph} I_p = H_g \cdot 2g \tag{2.14}$$

where T_{ph} is the number of winding turns per phase and I_p is the peak phase winding current. Assuming a value for the peak phase winding current allowable in the motor, the number of turns per phase of the RSRM can be calculated as,

$$T_{ph} = \frac{H_g \cdot 2g}{I_p} \tag{2.15}$$

If J is the maximum allowable current density in the winding and m is the number of phases, the cross-section area of a conductor is calculated as,

$$a_c = \frac{I_p}{J\sqrt{m}} \tag{2.16}$$

Neglecting the leakage of flux linkages, the area of the stator pole, the flux density in the stator pole, the area of the stator yoke, and the height of the stator pole can be calculated, respectively, as,

$$A_s = \frac{DL\beta_s}{2} \tag{2.17}$$

$$B_s = \frac{\phi}{A_s} \tag{2.18}$$

$$A_y = C_{sy} \cdot L = \frac{A_s B_s}{B_y} \tag{2.19}$$

$$h_s = \frac{D_o}{2} - \frac{D}{2} - C_{sy} \tag{2.20}$$

where C_{sy} is the thickness of the stator yoke and D_o is the outer diameter of the stator lamination. The rotor pole area is given by,

$$A_r = \left(\frac{D}{2} - g\right) L\beta_r \tag{2.21}$$

If the rotor yoke has a radius equal to the width of the rotor pole, the rotor yoke width and the height of the rotor pole are sequentially calculated as,

$$C_{ry} = \frac{A_r}{L} \tag{2.22}$$

$$h_r = \frac{D}{2} - g - C_{ry} \tag{2.23}$$

This completes the analytical relationships required for the RSRM design.

2.2.3 Conversion of RSRM Dimensions to LSRM Dimensions

The bore circumference of the RSRM forms the length of one sector of the LSRM. The total number of sectors of the LSRM is given by,

$$N_{sc} = \frac{L_t}{\pi D} \tag{2.24}$$

For the number of poles N_s in the stator of the RSRM, the number of stator poles is obtained by,

$$n = N_s N_{sc} \tag{2.25}$$

The width of stator pole and the width of stator slot are given by,

$$w_{sp} = \frac{A_s}{L} = \left(\frac{D}{2}\right)\beta_s \tag{2.26}$$

$$w_{ss} = \frac{(\pi D - N_s w_{sp})}{N_s} \tag{2.27}$$

The translator pole width and the translator slot width are converted from the rotor pole area neglecting the air gap length and are given by,

$$w_{tp} = \left(\frac{D}{2}\right)\beta_r \tag{2.28}$$

$$w_{ts} = \frac{(\pi D - N_t w_{tp})}{N_t} \tag{2.29}$$

where N_t is the number of poles in the rotor of the RSRM. Now, the fill factor of the windings is verified to see if the slot size is sufficient to hold the windings. The fill factor is defined as,

$$FF = \frac{Stator\ Winding\ \ Area}{Stator\ Slot\ Window\ Area} \tag{2.30}$$

The diameter of the conductor is given by,

$$d_c = \sqrt{\frac{4a_c}{\pi}} \tag{2.31}$$

Assuming that a portion of the stator pole height is occupied by wedges to hold the windings in place given by w, the number of vertical layers of winding is,

$$N_v = f_f \frac{(h_s - w)}{d_c} \tag{2.32}$$

where f_f is the form factor or packing factor. If the number is a fraction, it is rounded off to a lower integer. The number of horizontal layers of winding is given by,

$$N_h = \frac{T_{ph}}{2N_v} \tag{2.33}$$

The stator winding area is given by,

$$Stator\ Winding\ Area = 2\frac{a_c N_h N_v}{f_f} \tag{2.34}$$

Finally, the fill factor is calculated as,

$$FF = \frac{Stator\ Winding\ Area}{Stator\ Slot\ Window\ Area} = \frac{2\dfrac{a_c N_h N_v}{f_f}}{w_{ss}(h_s - w)} = \frac{2a_c N_h N_v}{f_f w_{ss}(h_s - w)} \tag{2.35}$$

Consideration has to be given to keep the two phase windings in the slot separated also. Then the normal range of the fill factor is in the range given by $0.2 \leq FF < 0.7$. The translator length for an LSRM with 8 translator poles is then calculated as,

$$L_{tr} = 8w_{tp} + 7w_{ts} \tag{2.36}$$

Since the core stack length of the LSRM equals the stator stack length of the RSRM, the core stack length is written as,

$$L_w = L = kD \tag{2.37}$$

Finally, the following condition has to be satisfied,

$$N_s(w_{sp} + w_{ss}) = N_t(w_{tp} + w_{ts}) \tag{2.38}$$

The winding details of the RSRM and LSRM are identical in this design. This need not be the case as the duty cycle of a winding in the four-phase LSRM, $1/(4N_{sc})$ whereas that of the RSRM winding it is $1/4$. Therefore, the windings in the LSRM can have much lower copper volume but taking more losses.

2.3 Prototype Design Example

2.3.1 Four-phase LSRM Prototype for a Ship Elevator [1]

An LSRM prototype is designed for a ship elevator, with a maximum linear velocity of 0.5m/s and acceleration time of 0.25s. The payload of the vehicle including translators' assembly is 200kg per LSRM. The ship elevator consists of 24 LSRMs carrying 4,536kg and hence 200kg corresponds to the payload per LSRM. The acceleration is then given by,

$$a_a = \frac{v_m}{t_a} = \frac{0.5}{0.25} = 2\ m/s^2$$

The instantaneous acceleration force is calculated as,

$$F_a = M_t \cdot (a_a + a_g) = 200 \cdot (2 + 9.8) = 2{,}360\ N$$

The deceleration $a_d = -2m/s^2$ and the instantaneous deceleration force is given as,

$$F_a = M_t \cdot (a_d + a_g) = 200 \cdot (-2 + 9.8) = 1{,}560\ N$$

The power capacity of the LSRM is $P = F_a v_m = 2360 \cdot 0.5 = 1{,}180$W. The RSRM is assumed to have a stator pole angle $\beta_s = 18^o = 0.314$ rads and a rotor pole angle $\beta_r = 22^o = 0.384$ rads. After fine-tuning the parameters, the constants are set as follows: $k_e = 0.5$, $k_d = 1$, $k_2 = 0.7$, $B_g = 1.65$ T, $A_{sp} = 38000$, and $k = 2.3$. The bore diameter is obtained as,

$$D = \sqrt{\frac{P\pi}{60 \cdot k_e k_d k_1 k_2 k B_g A_{sp} v_m}} = 172.2\ mm$$

The stack length of the RSRM is obtained as,

$$L = kD = 0.7 \cdot 172 = 396mm \cong 400mm.$$

The stator yoke thickness C_{sy} is given by,

$$C_{sy} = \frac{D\beta_s}{2} \approx 27\ mm$$

With D_o = 2D=344 mm, the height of the stator pole h_s can be calculated as,

$$h_s = \frac{D_o}{2} - \frac{D}{2} - C_{sy} = \frac{344}{2} - \frac{172}{2} - 27 = 59\ mm$$

The rotor back-iron width C_{ry} and the height of the rotor pole h_r are then calculated as,

$$C_{ry} = \left(\frac{D}{2}\right)\beta_r = \left(\frac{172}{2}\right)0.384 \approx 33\ mm$$
$$h_r = \frac{D}{2} - g - C_{ry} = \frac{172}{2} - 1 - 33 \approx 52\ mm$$

The magnetic field intensity in the air gap is calculated as,

$$H_g = \frac{B_g}{\mu_0} = \frac{1.65}{4\pi \cdot 10^{-7}} = 1313028.3\ A/m$$

For a peak phase winding current of I_p = 8 A,

$$T_{ph} = \frac{H_g \cdot 2g}{I_p} \approx 328\ Turns/\ phase$$

Assuming a current density of J = 4.86 A/mm^2, the area of a conductor is calculated as,

$$a_c = \frac{I_p}{J\sqrt{m}} = \frac{8}{4.86\sqrt{4}} = 0.823\ mm^2$$

In active translator and passive stator structure of LSRM, the stator and rotor of RSRM corresponds to the translator and stator of LSRM, respectively. The widths of stator pole and stator slot are given by,

$$w_{sp} = C_{ry} \approx 33\ mm$$
$$w_{ss} = \frac{(\pi D - 6w_{sp})}{6} = \frac{(\pi \cdot 172 - 6 \cdot 33)}{6} \approx 57\ mm$$

The translator pole width and the translator slot width are calculated as,

$$w_{tp} = C_{sy} \approx 27\ mm$$
$$w_{ts} = \frac{(\pi D - 8w_{tp})}{8} = \frac{(\pi \cdot 172 - 8 \cdot 27)}{8} \approx 41\ mm$$

The total length of the translator is given by,

$$L_{tr} = 8w_{tp} + 7w_{ts} = 8 \cdot 27 + 7 \cdot 41 = 503\ mm$$

The core stack width of the LSRM is obtained from the stator stack length of the RSRM as,

$$L_w = L = kD \cong 400\ mm$$

Now, the fill factor of the windings is verified to see if the slot size is sufficient to hold the windings. The diameter of the conductor is given by,

$$d_c = \sqrt{\frac{4a_c}{\pi}} = \sqrt{\frac{4 \cdot 0.823}{\pi}} = 1.023\ mm$$

The closet wire size with this diameter is AWG #18. It has 1.0237mm and selected for the phase windings. Assuming the width of the wedges w = 1 mm and packing factor f_f = 0.7, the number of vertical layers of winding and the number of horizontal layers of winding are given by,

$$N_v = f_f \cdot \frac{(h_s - w)}{d_c} = 0.7 \cdot \frac{(59-1)}{1.0237} \approx 20$$

$$N_h = \frac{T_{ph}}{2 \cdot N_v} = \frac{328}{2 \cdot 20} \approx 8$$

The stator winding area is given by,

$$Stator\ Winding\ \ Area = 2\frac{a_c N_v N_h}{f_f} \cong 386\ mm^2$$

The fill factor is calculated as,

$$FF = \frac{Stator\ Winding\ \ Area}{Stator\ \ Slot\ Window\ \ Area} = \frac{386}{(59/2-1)\cdot 41} = 0.330$$

Note that the condition outlined in (2.35) is also satisfied with this design. Fig 2.3 and Table 2.1 show the final dimensions of the designed four-phase LSRM for a ship elevator [1]. The dimensions are fine tuned to be suitable for the elevator application.

Table 2.1. Dimension of the designed LSRM for a ship elevator

Stator pole width, w_{sp}	42mm	Translator pole width, w_{tp}	26mm
Stator slot width, w_{ss}	62mm	Translator slot width, w_{ts}	52mm
Stator pole height, H_s	34mm	Translator pole height, H_r	28mm
Stator back-iron (yoke), C_{sy}	34mm	Translator back-iron (yoke), C_{ry}	0mm
Stack length, L	400mm	Air gap length, g	1mm
Peak phase current, I_p	8A	Turns per phase, T_{ph}	840
Current density, J	4.86A/mm^2	Wire size (AWG)	#18

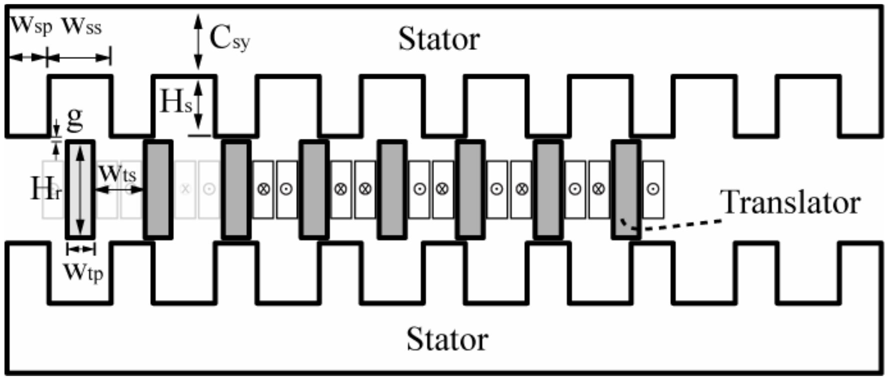

Fig. 2.3 Dimension of the designed four-phase LSRM for a ship elevator

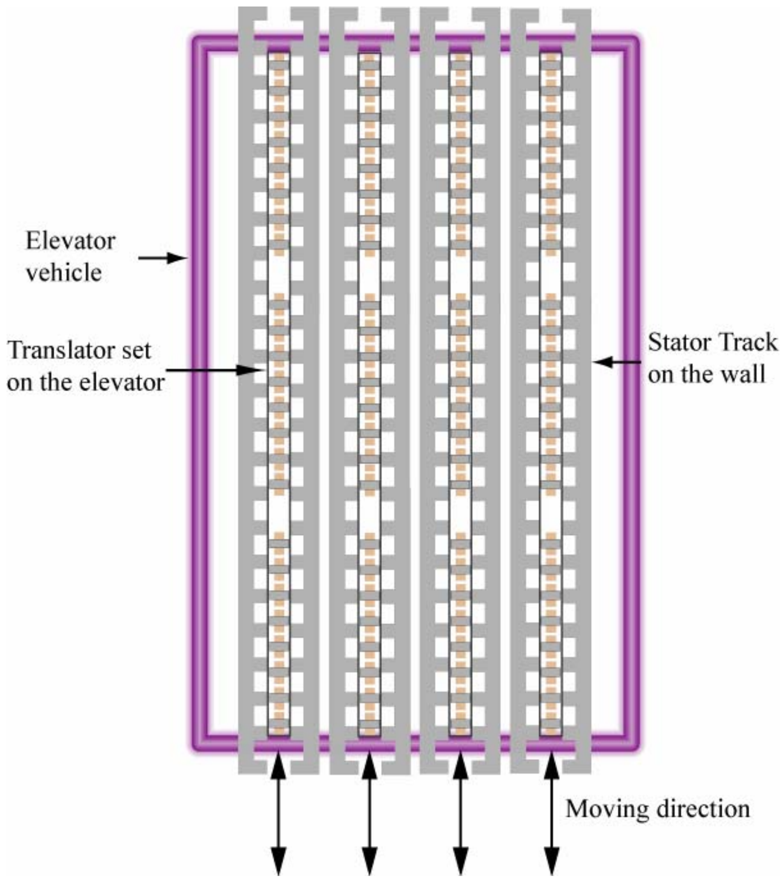

Fig. 2.4 Designed four-phase LSRM for a ship elevator :

12 LSRMs are installed on one side of the vehicle

Fig. 2.4 shows the installation of 24 LSRMs, stators and translators, on the ship elevator which is designed to carry 4,536kg in total as the payload. Each side has 12 LSRMs equally to share the required peak propulsion force, 55,000N at 0.5m/s with an acceleration of 1.98m/s^2. Hence, each LSRM is supposed to produce propulsion force of 2,300N. The stator track will be extended from bottom to top of the floor and the length will be long but dependent on the applications. The stator track will be constructed on the wall where the elevator will be placed. The translators will be mounted on the moving vehicle of the elevator. The details about mass of the translator and stator, the expected power loss as well as converter topology and control strategies to control this elevator are referred to [1].

2.3.2 Four-phase LSRM Prototype for a Scaled-down Elevator [19]

Since the prototype LSRMs for an elevator are a scaled-down version by around 1/8 of the ship elevator LSRM in terms of propulsion force, the dimension of the prototype LSRM can be obtained by shrinking the LSRM dimensions of the ship elevator. Table 2.2 and 2.3 show the specifications and dimensions of the prototype LSRM and elevator, respectively.

Table 2.2. Specifications of the prototype LSRM (8/6 type) and elevator

Number of LSRMs	2	Peak propulsion force	300N
Acceleration	1.96m/s^2	Peak phase current	12A
Air gap length	1.5mm	Rated phase current	10A
Rated payload	24kg	Rated voltage	170Vdc
Stack length, *L*	90mm	Cruising velocity	0.2m/s
Stator	1061mm	Elevator travel length	0.6m
Translator + Winding	309mm	Vehicle dimension	12”(L)x12”(W)x14”(H)
Steel type - stators	ASTM-A1011	Steel type - translators	CF1018 (non-laminated)

Table 2.3. Dimensions of the LSRM for the prototype elevator

Stator pole width, W_{sp}	21mm	Translator pole width, W_{tp}	13mm
Stator slot width, W_{ss}	31mm	Translator slot width, W_{ts}	26mm
Stator pole height, H_s	30mm	Translator pole height, H_r	48mm
Stator back-iron (yoke), C_{sy}	35mm	Translator back-iron (yoke), C_{ry}	0mm
Stack length, L	90mm	Air gap length, g	1.5mm
Peak phase current, I_p	10A	Turns per phase, T_{ph}	396
Current density, J	6.07A/mm^2	Wire size (AWG)	#18

The prototype elevator is designed to carry 24kg including the vehicle weight at the rated current of 10A. As shown in Table 2.3, the dimension of stator pole width and translator pole width is scaled down to ½ from the ship elevator LSRM. The other dimensions are dependent on wire turns (T_{ph}) which need to be adjusted to meet the required propulsion force along with rated phase current. Phase current times T_{ph} determines the magneto-motive force (MMF). For the prototype elevator, phase current and T_{ph} is set to 10A and 396 turns, respectively.

2.4 Design Verification

Design verification process, very much similar to the RSRM, includes finite element analysis (FEA) and experimental verification of the motor. FEA is made using one of the commercial software and the design is fine-tuned with these results. Based on the finalized design, a prototype motor is usually built and tested. A strong correlation between the FEA and experimental results assures confidence in the engineering analysis and design methods adopted, and enables confident scaling of the motor. A poor correlation of the results forces a designer to revisit the design methodology.

2.4.1 FEA Verification

In this section, two-dimensional FEA is used to verify the design procedure of the LSRM and the accuracy of the analytical method. The flux linkages and the inductances of the phase windings, the propulsion and normal forces developed by the motor for various excitation currents and translator positions are determined. FEA, in general, provides more accurate results than the magnetic analytical method with equivalent circuit method because it considers a large number of flux paths compared to the magnetic equivalent circuit method.

The field solution is obtained using Mawell-2D software package of Ansoft Corporation. The entire problem region is subdivided into triangular finite elements. The LSRM translator is moved from an unaligned position with respect to the stator to an aligned position at different excitation currents, and corresponding to each translator position, inductance, propulsion force, and normal force are obtained.

Fig. 2.5 shows the flux distributions inside the LSRM for the fully aligned position, one intermediate position of 12mm shifted from the fully aligned position, and the fully unaligned position of 26mm. These plots are obtained at a phase current of 10A in one phase winding. It is observed that the leakage flux lines cross the stator slot air gap to the adjacent stator poles and complete their path through the stator back-irons. The proposed LSRM has two air gaps and the translators without back-iron are placed in the middle of two stators. Thus, the translators act like bridges between two stators, and the flux densities are higher than stators. In addition, the flux densities in the excited translator poles are high for a given excitation. The flux densities in other parts of the motor are very low.

Fig. 2.6 shows the force, flux linkage and inductance profile at several different phase currents with respect to various translator positions. The force in a given direction is obtained by differentiating the magnetic co-energy of the system with respect to a virtual displacement of the translator in this direction using the calculated flux densities in each triangular element of FEA simulation. Based on this approach, the propulsion force at various currents with respect to various translator positions are calculated and shown in Fig. 2.6. The inductances are identical in all different current because the designed LSRM has a large air gap of 1.5mm and does not have any saturation problem. Hence, the experimental measurement does not need all range of current to collect different inductance data, but only one phase current are sufficient to show the measurement vs. FEA simulations as described in next section.

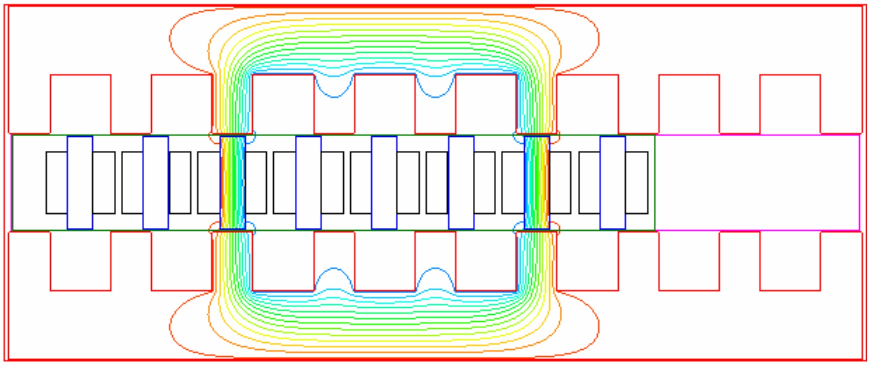

(a) Fully aligned position

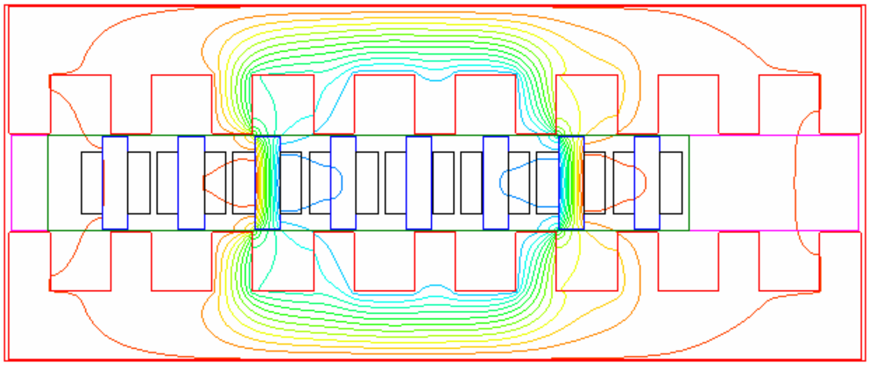

(b) Intermediate position: 12mm shifting of translator from fully aligned position

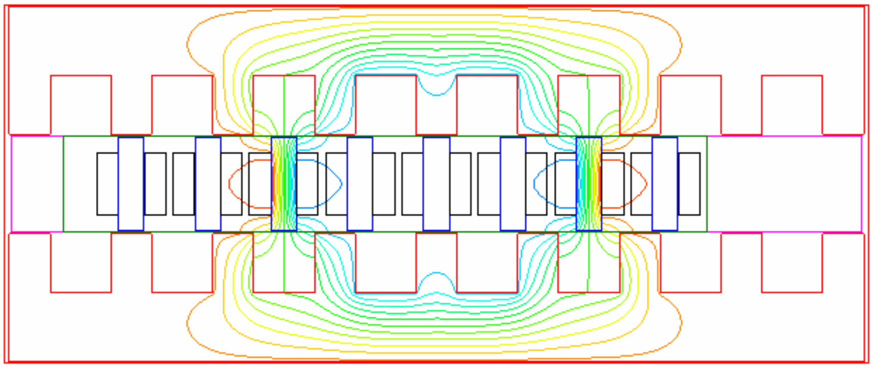

(c) Fully unaligned position: 26mm shifting of translator from fully aligned position

Fig. 2.5 Flux distribution of the four-phase LSRM prototype at rated current, 10A

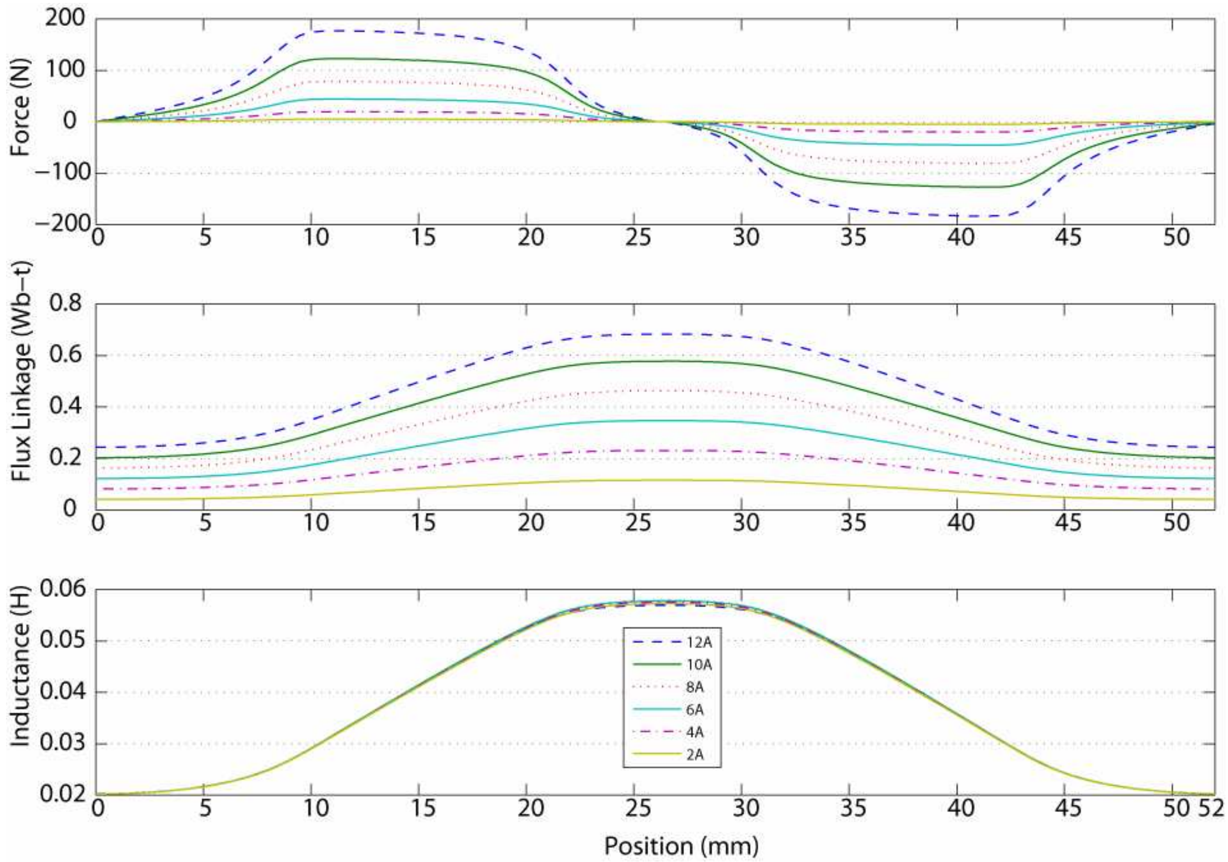

Fig. 2.6 FEA simulation results: Force, flux linkage and inductance profile

2.4.2 Experimental Setup and Measurements

2.4.2.1 Design Features of the proposed LSRM

The LSRM for the prototype elevator has unique features as a vertical propulsion motor compared with conventional horizontal LSRMs, and they are summarized below with respect to translator and stator. Their details concerning the LSRM design are described in [19]. The four-phase LSRM with six stator poles and eight translator poles is selected for the prototype elevator. The windings are on eight translator poles, rendering the translator to be active component.

A. Translator with no back-iron

An initiative study and a comparative evaluation of various topologies for a LSRM elevator are discussed in references [1] and [19], respectively. Based on the studies, the no back-iron configuration has been selected as the most suitable LSRM configuration for this vertical application, an elevator. The main features of the translator configuration are listed below:

- High propulsion force per translator
- Compact design as an attractive alternative for vertical applications
- Consideration for installation of translator poles to the vehicle
- Each pole machined from a single piece of mild steel (CF1018)

B. Stator with wider pole width

Since an elevator is a vertical propulsion application, only positive propulsion force is required due to two-quadrant operation of motoring and breaking modes, as discussed in previous chapter. Thus, the positive propulsion force shape needs to be symmetric. This is discussed by the author *et al.* [1] and shown that it is possible to achieve symmetric positive force by making the stator pole width wider than conventional ratio between stator and translator pole width ($w_{sp} \approx 1.2w_{tp}$) [20]. As for the prototype elevator, the ratio is set to approximately 1.62 (w_{sp} = 21mm, w_{tp} =13 mm). The ratio can be increased if more symmetric force profile is demanded, but it allows stator mass to increase.

2.4.2.2 Experimental Setup for the prototype elevator

The prototype elevator has two LSRMs whose windings are connected in series to reduce input current. Each side of the prototype elevator has one LSRM consisting of two stators and one translator as shown in Fig. 2.7. An LSRM is installed on each side of the prototype elevator to make vertical transportation more stable and fault tolerant. Each LSRM has been designed to carry the payload of 12kg at rated phase current, 10A. The translator needs careful installation because the poles of the translator are separated individually due to no back-iron. Thus, a spacer is installed to ensure constant separation between the poles. As shown in Fig. 2.7(c), spacer aluminum bars are equipped to ensure the same pole slot width. Additionally, the air gap spacers are provided to maintain the air gap between stators and translators.

Fig. 2.8 shows the experimental setup for the measurement of the propulsion force and phase inductance. It is measured after locking (hanging in the air) the translator using the holding plate and connectors at the desired position and energizing one phase winding with a constant DC current through a PWM power converter. For the propulsion force test, when the current reaches steady state, the load cell sensor output is recorded. This test procedure is repeated at various currents and translator (vehicle) positions. The value is measured using an S-type load cell, which is used where the load is pull or pushed in a straight line without a side load. The translator and its mechanical support are connected through the screws at each end of S-type load cell to minimize any off-center pulling or pushing.

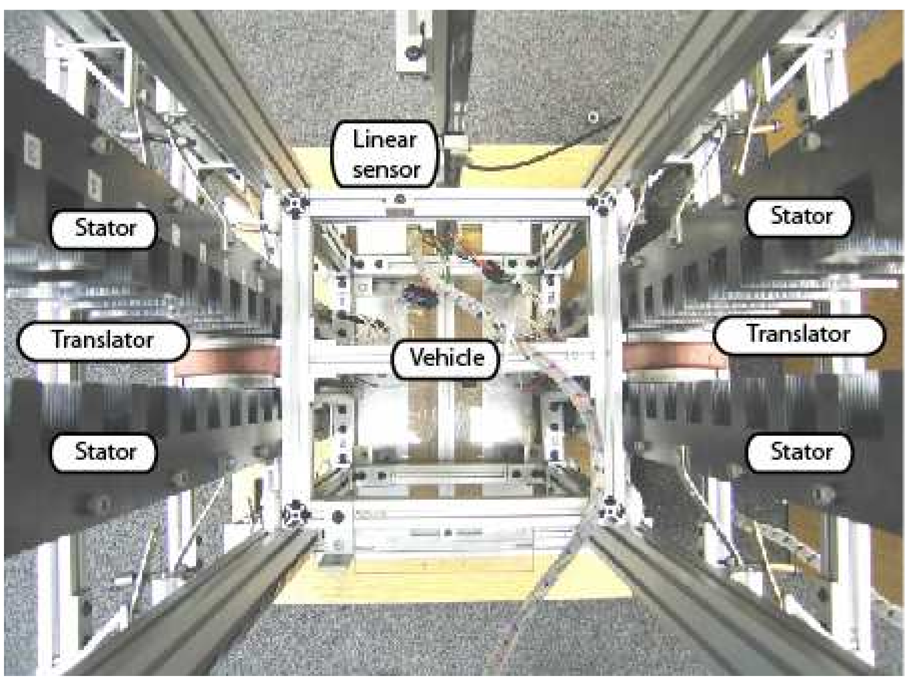

(a) Prototype elevator: Top view

Fig. 2.7 Prototype elevator setup and translator assembly

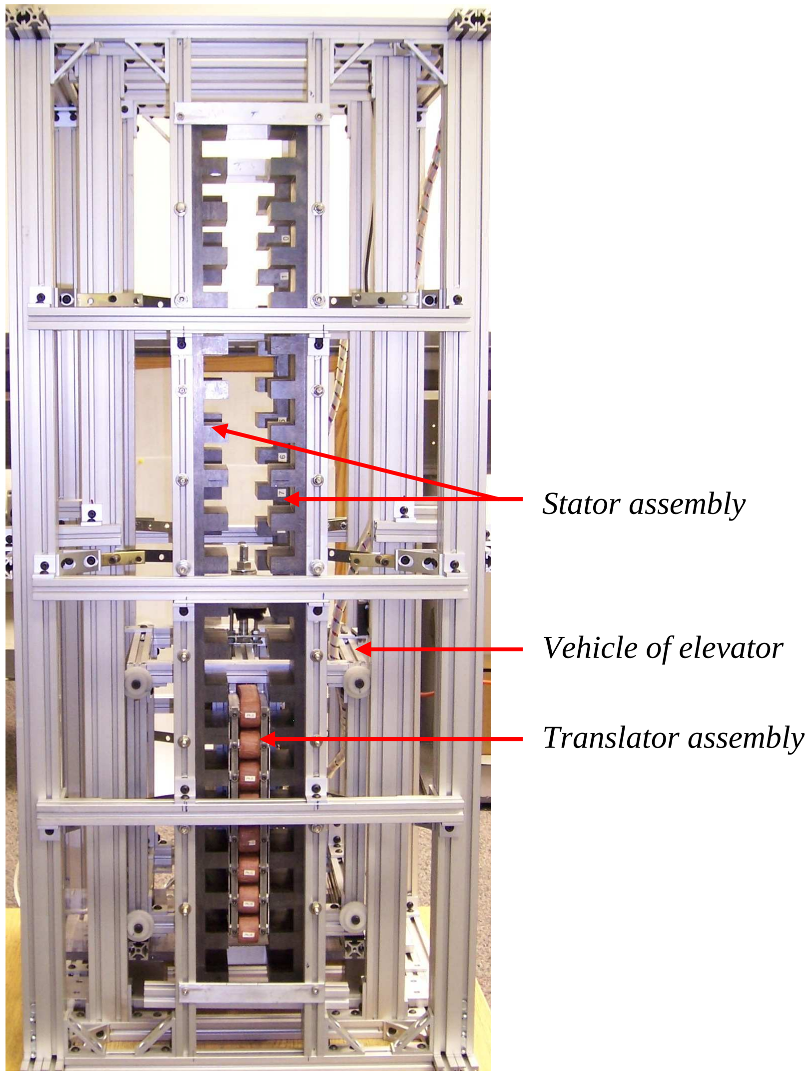

(b) Prototype elevator: Front view

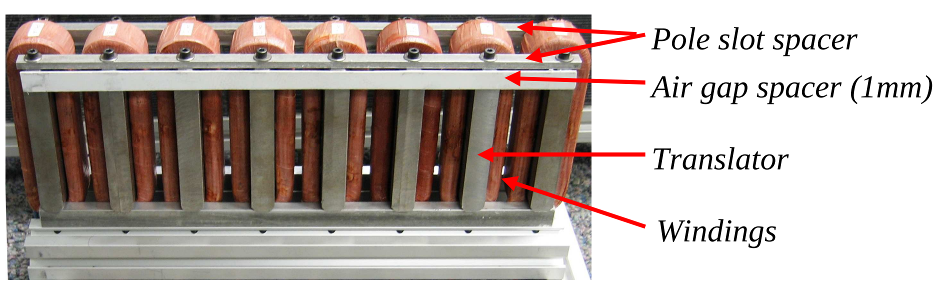

(c) Translator assembly: 8 poles

Fig. 2.7 Prototype elevator setup and translator assembly (continued)

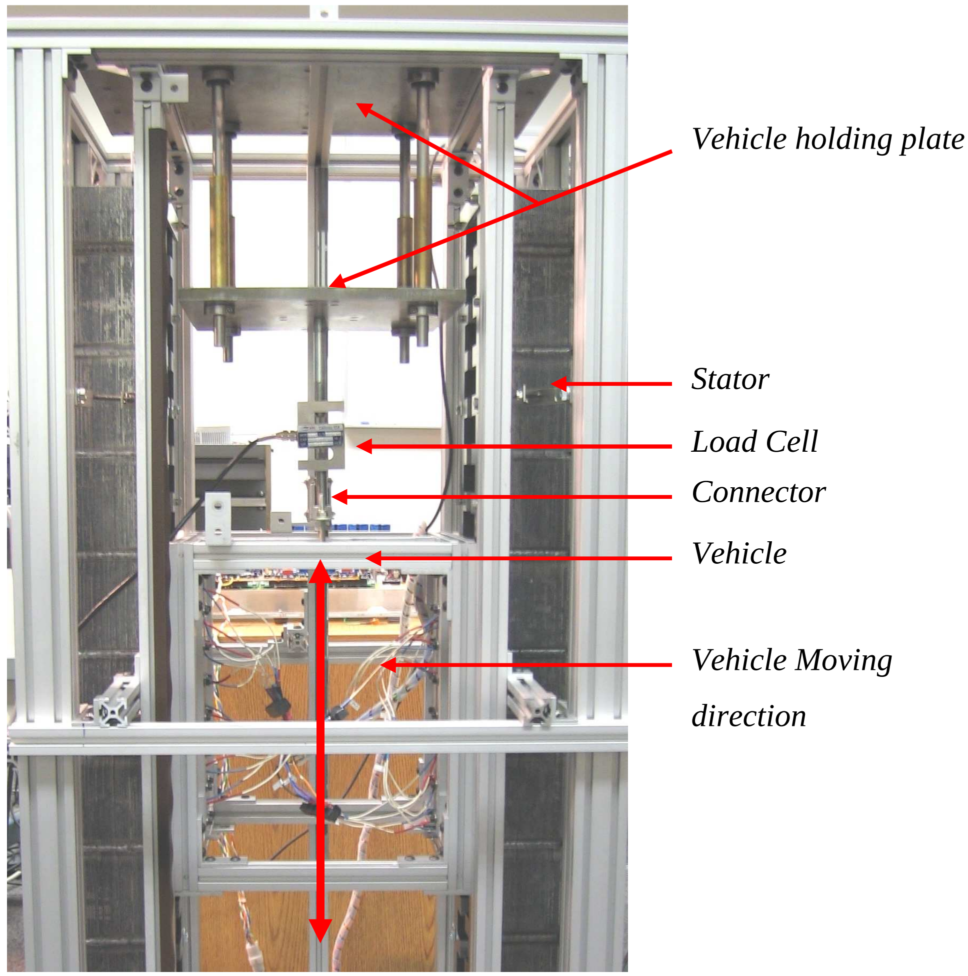

Fig. 2.8 Experimental setup for the propulsion force measurement

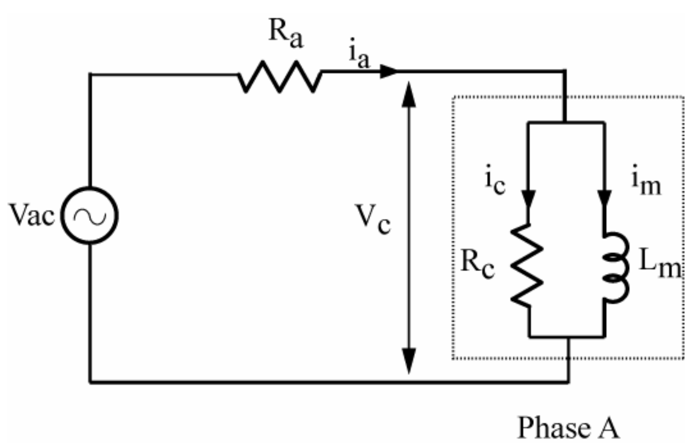

Fig. 2.9 Equivalent circuit for the phase inductance measurement

Table 2.4. Parameters in Fig. 2.9

V_{ac}	5~120Vac at 60 Hz	i_a	2A (rms)
V_c	AC Voltage across the inductance	i_{ac}	Core loss current of phase A
R_a	2.2 ohm, Resistance in Phase A	i_m	Magnetizing current
R_c	Core loss Resistance in Phase A	L_m	Phase inductance

Fig. 2.9 shows the equivalent circuit for the measurement of phase winding inductance. The measurement method using equivalent circuit model is adopted, which was used by Ha *ea al.* [52] and the symbols are explained in Table 2.4. Ha *et al.* did measurement using a special tool of *National Instrument* to calculate the instantaneous power. Afterward, the core loss power is given by subtracting the resistive loss from the instantaneous power and hence the core loss current can be found based on the literature. But, a simple method is used without any special measurement equipments for the inductance measurement.

First, power factor angle θ, a time delay between input voltage and current, and is obtained from an oscilloscope. Then AC voltage across the inductance, V_c is calculated as,

$$\begin{aligned} v_c &= V_c\angle\theta_c = V_{ac}\angle 0' - I_a R_a \angle\theta \\ &= \left[V_{ac} - I_a \cos\theta \cdot R_a\right] - jI_a \cdot \cos\theta \cdot R_a \end{aligned} \tag{2.39}$$

From Eq. (2.39), core loss angle is calculated as,

$$\theta_c = \tan^{-1}\left(\frac{-I_a \sin\theta \cdot R_a}{V_{ac} - I_a \cos\theta \cdot R_a}\right) \tag{2.40}$$

Then, core loss power and core loss resistance are given as,

$$\begin{aligned} P_c &= I_c V_c \cos\theta_c \\ &= \frac{V_c^{\,2}}{R_c} \\ &= P - I_a^{\,2} R_a \\ &= V_{ac} I_a \cos\theta - I_a^{\,2} R_a \end{aligned} \tag{2.41}$$

$$\therefore R_c = \frac{V_c^{\,2}}{P - I_a^{\,2} R_a} \tag{2.42}$$

As a result, core loss current and inductance (magnetizing) current are obtained as,

$$i_{ac} = I_{ac}\angle\theta_c = \frac{V_c}{R_c}\angle\theta_c \tag{2.43}$$

$$\begin{aligned} i_m &= I_m\angle\theta_m = I_a\angle\theta - I_{ac}\angle\theta_c \\ &= \left[I_a\cos\theta - I_{ac}\cos\theta_c\right] + j\left[I_a\sin\theta - I_{ac}\sin\theta_c\right] \end{aligned} \tag{2.44}$$

Therefore, the phase inductance, L_m, is gained as,

$$L_m = \frac{V_c}{2\pi\cdot f\cdot I_m} \tag{2.45}$$

where f is the frequency of input voltage, V_{ac}. In this case, f is 60Hz.

After the translator is locked mechanically to the desired position as shown in Fig. 2.8 for the propulsion force measurement, 60Hz voltage excitation is used to measure inductances at 2A (RMS). As mentioned earlier, the prototype LSRM has a large air gap which causes no saturation, and hence the phase inductances are same at different current up to rated current, 10A. Beyond the rated current, the inductance is getting slightly deviated from the unsaturated inductances due to the effect of saturation as the vehicle position gets close to the aligned position. The test is repeated at different translator (vehicle) position at the same current of 2A (RMS) with the alternating voltage changed due to the phase inductance change according to the vehicle position after isolating eddy current losses.

Fig. 2.10 shows the correlation of the FEA and measurement data. Fig. 2.10(a) shows the experimentally measured propulsion force and the simulated force using 2D FEA versus position at different translator (vehicle) positions and phase currents. It is shown that there is high correlation between the FEA and measured values. A slight discrepancy between the two sets of values is less than 5% which is ignorable.

Fig. 2.10(b) shows the measurement results and demonstrates correlation to the FEA results. The inductance profiles at phase currents lower than 10A as a rated value are almost identical to the profile at rated current. It is due to the fact that the air gap is usually very large in the linear motor and hence motor does not saturate within operating range of phase currents. There is high correlation in the unaligned inductance region, but there are some discrepancies up to 10% in the aligned inductance region. The error is usually attributable to the end effects, and the distortion of the magnetic properties of the core material due to punching stresses, inexact *B-H* characteristics provided by the steel manufacturers and non-uniformity of the air gap to a smaller degree. In addition, end leakage effects in unaligned position are generally severe in the fully unaligned position because the reluctance of the end paths becomes comparable to that of the air gap paths. However, the comparison results in Fig. 2.10 (b) show that more discrepancies occur around aligned position mainly due to the solid (non-laminated) steel of translator poles and the nature of the experimental setup causing non-uniformity of the air gap of 1.5mm. The comparison data of force and inductance is summarized in Table 2.5.

Table 2.5. Comparison of force and inductance values

Force (N)			Inductance (mH)		
At 10A	FEA	Measurement	At 2A (rms)	FEA	Measurement
F_{ea_max}	120	118	L_{a_max}	57.2	52.5
F_{err_max}	116	110	L_{a_min}	20.3	20.7
F_{err_min}	30	35	*Max Error*	4.7 (8.2%)	

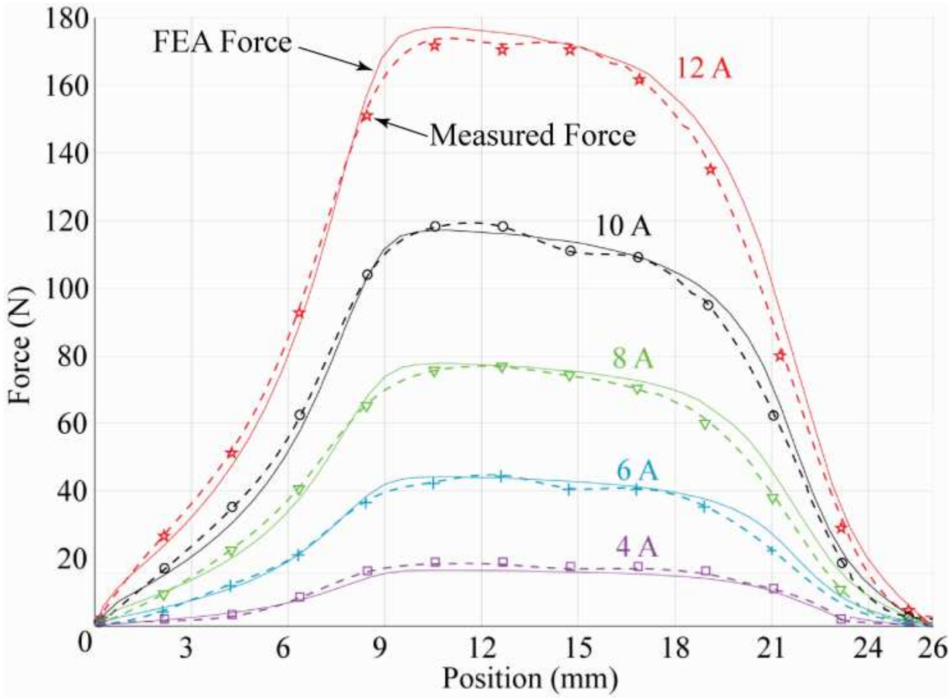

(a) Measurement and FEA simulation results of propulsion force at different phase currents

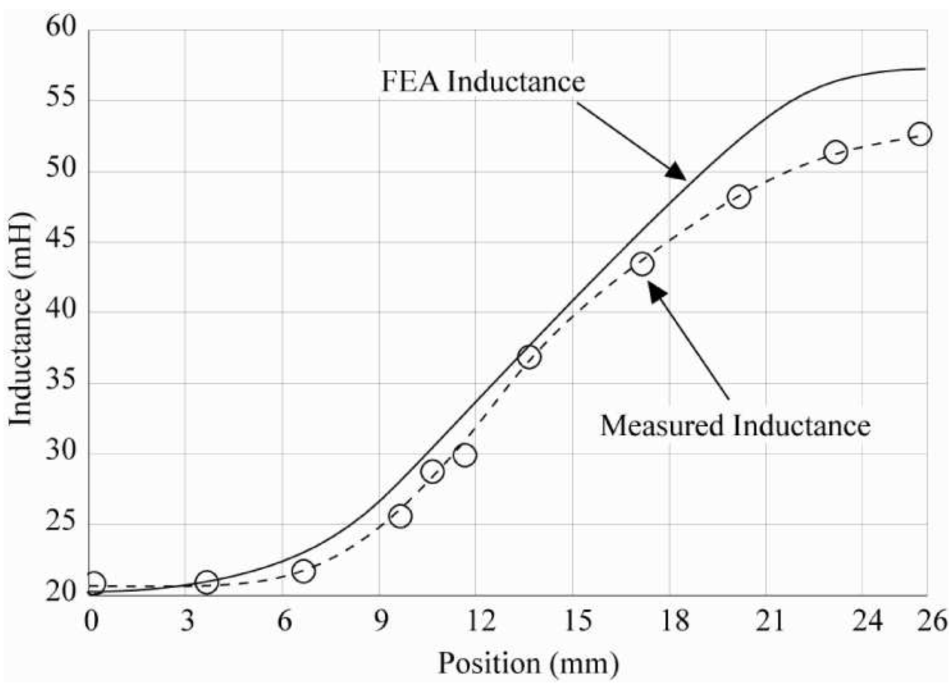

(b) Measurement and FEA simulation results of inductance at 2A, phase current

Fig. 2.10 Correlation of experimental measurement data and FEA results: Force and inductance

2.5 Conclusions

The following are considered to be original contributions out of this chapter:

1) A novel LSRM topology for a prototype ropeless elevator has been proposed and designed using the current knowledge and design procedure of rotating switched reluctance motor (RSRM) [8]. The proposed LSRM topology has no back-iron and non-laminated translator poles.
2) The prototype LSRMs are scaled down from the designed ship elevator presented by the author *et al.* [1], and optimized to be suitable for the prototype elevator which can generate the propulsion force of 300N.
3) 1.061m long, two four-phase prototype LSRMs for an elevator have been developed for the first time based on the developed design procedure.
4) A prototype elevator with a size of 22 x 26 x 50 (WxLxH) inches and a travel length of 0.68m has been built using two assembled LSRMs. Translators are installed on the moving vehicle whose size is 12 x 12 x 14 (WxLxH) inches and total weight is 20.3 kg. The rate velocity is set to 0.2m/s and the rated payload 24kg at 10A including the vehicle weight.
5) The prototype elevator has been tested with conventional asymmetric half bridge converters and proportional plus integral (PI) current controller.
6) Experimental correlation of inductances and propulsion forces to FEA simulation results has confirmed the validity of the design procedure of the LSRM.

CHAPTER 3

CONTROL OF A ROPELESS PROTOTYPE LSRM ELEVATOR WITH NOVEL FORCE CONTROL

In this chapter, control strategies for the prototype LSRM elevator are presented with a novel force control. The control system of the prototype elevator contains four parts: velocity, position, force, and current control. As mentioned by Ishii [4], conventional rope elevators have a serious problem with torque ripple generated by rotary traction motors. Torque ripple renders the cap of elevators oscillating vertically and hence torque control needs to be intensified to avoid the undesirable behavior of elevators during operation. Switched reluctance motors (SRM), however, have been known for high torque ripple, and hence SRMs have not been applied yet into vertical traverse applications. In this respect, force ripple generated in the prototype LSRMs should be considered as the most important factor to control in order to apply LSRM technology into vertical applications, such as a ropeless elevator. In this chapter, a effective force control method using a novel force distribution function (FDF) is presented to suppress force ripple during commutation, an overlapping period between turn-off of one phase and turn-on of the following phase. The proposed force control has been discussed by the author [1], and adopted in this research for an experimental validation of successful force control performance.

This chapter is organized as follows: The review of the previous control works concerning force ripple reduction is described and dynamic LSRM mathematical model is derived to draw control strategy. Then, control scheme is presented, which consists of force, current, velocity, and position control with a velocity profile. Converter topology and switching strategy for the prototype LSRM elevator are presented, and finally extensive dynamic control simulations are correlated with experimental results from the 1.27m-tall prototype elevator with two sets of LSRMs installed on each side of vehicle and structure as shown in Chapter 2.

3.1 Introduction

Since LSRMs have been known that they have large force ripple, force ripple needs to be avoided in order to apply LSRMs into an elevator application as a competitive candidate. For force and torque ripple reduction in (L)SRMs, several control strategies have been proposed in [5]-[6], [21], [36], [41]-[45]. The basic idea is to distribute a desired propulsion force to two adjacent phases during predetermined commutation interval using a force distribution function (FDF). FDF corresponds to TDF (torque distribution function) in rotating SRM (RSRM).

Based on inductance profiles, Schramm *et al.* [21] proposed the phase current optimal profiling in the sense of minimum stator copper loss. Due to the finite bandwidth of current control loop, significant torque ripple accompanied this control scheme during commutation. Husain *et al.* [41] and Ilic-Spong *et al.* [42] proposed a sinusoidal function and an exponential function as a TDF in RSRM, respectively. Since TDF is to distribute a desired torque to two adjacent phases during predetermined commutation interval, the excitation interval of a phase was increased to more than 15 degrees. These schemes can be viewed as having TDFs given in (3.4)-(3.7) such that the sum of the phase torque commands are equal to the commanded torque.

$$T_e^* = T_x^* + T_y^* \tag{3.1}$$

where,

$$\begin{aligned} T_x^* &= T_e^* f_x(\theta) \\ T_y^* &= T_e^* f_y(\theta) \end{aligned} \tag{3.2}$$

The reference angles θ_i' and θ_f' are the initial and the final angle of the commutation region, respectively. According to the approaches, the choice of the reference angles depends on the inductance profile of a specific motor. For instance, when $T_e^* \geq 0$ and $0^\circ \leq \theta < 15^\circ$ for an 8/6 RSRM,

$$0^\circ << \theta_i' < \theta_f' < 15^\circ \tag{3.3}$$

Therefore, the excitation interval of a phase was much narrower than 30 degrees and all phases were not fully utilized in their approaches. Husain *et al*. [41] proposed following TDF.

$$
\begin{aligned}
f_x(\theta) &= \begin{cases} 1 & \text{for } 0^\circ \le \theta < \theta'_i \\ \left(1 + \cos k(\theta - \theta'_i)\right)/2 & \text{for } \theta'_i \le \theta < \theta'_f \\ 0 & \text{for } \theta'_f \le \theta < 15^\circ \end{cases} \\
f_y(\theta) &= \begin{cases} 0 & \text{for } 0^\circ \le \theta < \theta'_i \\ \left(1 - \cos k(\theta - \theta'_i)\right)/2 & \text{for } \theta'_i \le \theta < \theta'_f \\ 1 & \text{for } \theta'_f \le \theta < 15^\circ \end{cases}
\end{aligned}
\tag{3.4}
$$

where,

$$k = 180 / \left(\theta'_f - \theta'_i\right) \tag{3.5}$$

On the other hand, Ilic-Spong *et al*. [42] proposed following TDF.

$$
\begin{aligned}
f_x(\theta) &= \begin{cases} 1 & \text{for } 0^\circ \le \theta < \theta'_i \\ e^{-((\theta-\theta'_i)/k)^2} & \text{for } \theta'_i \le \theta < \theta'_f \\ 0 & \text{for } \theta'_f \le \theta < 15^\circ \end{cases} \\
f_y(\theta) &= \begin{cases} 0 & \text{for } 0^\circ \le \theta < \theta'_i \\ 1 - e^{-((\theta-\theta'_i)/k)^2} & \text{for } \theta'_i \le \theta < \theta'_f \\ 1 & \text{for } \theta'_f \le \theta < 15^\circ \end{cases}
\end{aligned}
\tag{3.6}
$$

where,

$$k = \left(\theta'_f - \theta'_i\right)/5 \tag{3.7}$$

The rates of change of phase current commands were reduced during commutation as expected but by assuming an ideal inductance the resulting incorrect current commands caused torque error and by choosing relatively short commutation interval the changing rates of currents could not be reduced significantly.

For a 6/4 RSRM, instead of defining a TDF, Wallace *et al.* [43] linearly decreased the leading phase current and increased the following phase current during commutation interval. By neglecting the relationship between the output torque and the phase currents during commutation, the torque ripple was inevitable whereas the rates of change of phase currents were fixed for a given torque command. Kim *et al.* [44] proposed a TDF, which could minimize the changing rates of currents over the commutation interval. With this approach, an extensive off-line numerical calculation to obtain the optimal solution was necessary for individual RSRM and excessive memory was required to store the TDF.

Recently, Bae *et al.* [5][36] has proposed an efficient FDF using the rate of change of inductance and its combination, and successfully applied the FDF into a RSRM as well as a horizontal LSRM. However, there is a problem in adopting Bae *et al.*'s FDF because the inductance of LSRMs for an elevator application is too high to apply the proposed nonlinear FDF function. The FDF function causes the phase current not to respond fast enough to track the current command. In contrast to results of the horizontal LSRM application, force ripples of vertical LSRMs are very high in using the Bae *et al*.'s FDF and the results are presented by the author in [1]. Therefore, a new force control method is proposed in this chapter to reduce force ripple during commutation and hence to make LSRMs competitive and suitable primary propulsion source of a ropeless linear elevator.

3.2 Dynamic Model of Linear Switched Reluctance Motor

Control starts with a system model to control the system properly, and thus the system model has to contain good and extensive information showing the system's characteristics. In general, various kinds of electric motors have been modeled with different approaches, such as mathematical nonlinear equation and artificial neural networks. For this research, a mathematical model derived in [20] and [36] is used, and some parts are excerpted from [36].

3.2.1 Voltage Equations for Two-phase Excitation

With mutual inductance ignored, the voltage and flux linkage equations for a four-phase LSRM can be expressed in terms of both phase currents as follows.

$$
\begin{aligned}
v_a &= R_s i_a + \frac{d\lambda_a}{dt} \\
v_b &= R_s i_b + \frac{d\lambda_b}{dt} \\
v_c &= R_s i_c + \frac{d\lambda_c}{dt} \\
v_d &= R_s i_d + \frac{d\lambda_d}{dt}
\end{aligned}
\tag{3.8}
$$

and

$$
\begin{aligned}
\lambda_a &= L_a i_a \\
\lambda_b &= L_b i_b \\
\lambda_c &= L_c i_c \\
\lambda_d &= L_d i_d
\end{aligned}
\tag{3.9}
$$

where R_s is the winding resistance of a phase, and v_k and λ_k for $k = a, b, c, \text{and } d$ are the phase voltage and flux linkage, respectively.

If two adjacent phases are considered at a time and the phase currents of other two phases are assumed to be zero, then four-phase equation (3.8) and (3.9) can be simplified as follows.

$$
\begin{aligned}
v_x &= R_s i_x + \frac{d\lambda_x}{dt} \\
v_y &= R_s i_y + \frac{d\lambda_y}{dt}
\end{aligned}
\tag{3.10}
$$

and

$$
\begin{aligned}
\lambda_x &= L_x i_x \\
\lambda_y &= L_y i_y
\end{aligned}
\tag{3.11}
$$

where the subscript x are y are the phases in consideration and the set (x,y) is one of (a,b), (b,c), (c,d), and (d,a). Either phase x or phase y is leading and the other phase is following according to the direction of moving. For example, phase d is leading phase a in the first excitation region when the output force and the velocity are positive.

The voltage equations can be expressed in terms of either phase currents. In this subsection, phase currents are chosen as state variables. Differentiating (3.11) with respect to time *t* yields,

$$\begin{aligned} \frac{d\lambda_x}{dt} &= L_x \frac{di_x}{dt} + g_x \omega \cdot i_x \\ \frac{d\lambda_y}{dt} &= L_y \frac{di_y}{dt} + g_y \omega \cdot i_y \end{aligned} \tag{3.12}$$

where $\omega = dx/dt$ and g_x and g_y are the force functions defined as the rate of change of phase inductance according to position, $\frac{dL_k}{dx}$. Hence, substituting (3.12) into (3.10) and rearranging them yield,

$$\begin{aligned} \frac{di_x}{dt} &= -a_1 i_x - a_2 \omega \cdot i_x + a_0 v_x \\ \frac{di_y}{dt} &= -b_1 i_y - b_2 \omega \cdot i_y + b_0 v_y \end{aligned} \tag{3.13}$$

where,

$$\begin{aligned} a_0 &= \frac{1}{L_x} & b_0 &= \frac{1}{L_y} \\ a_1 &= a_0 R_s & b_1 &= b_0 R_s \\ a_2 &= a_0 \left(\frac{\partial L_x}{\partial x} \right) & b_2 &= b_0 \left(\frac{\partial L_y}{\partial x} \right) \end{aligned} \tag{3.14}$$

It can be noticed that there are a nonlinear back EMF terms in each equation in (3.13) and the current as a state variable contains a nonlinear motor parameter of phase inductance. It indicates that gain scheduling is required to achieve high performance current control. In other words, there is no need to change current controller's gain if there is an alternative current controller which is not highly dependent on the mathematical motor model. It will be discussed in Chapter 4.

3.2.2 Force Equation for Two-phase Excitation

Similarly, either phase currents can be assigned as state variables to express an output force equation. To express the output force in terms of phase currents and translator position, the output force equation is derived from the coenergy W_c. From the definition of the coenergy and the relationship given in (3.11), the differential coenergy is expressed as [53],

$$\begin{aligned} dW_c(i_x, i_y, x) &= \lambda_x di_x + \lambda_y di_y + F_e dx \\ &= (L_x i_x) di_x + (L_y i_y) di_y + F_e dx \end{aligned} \tag{3.15}$$

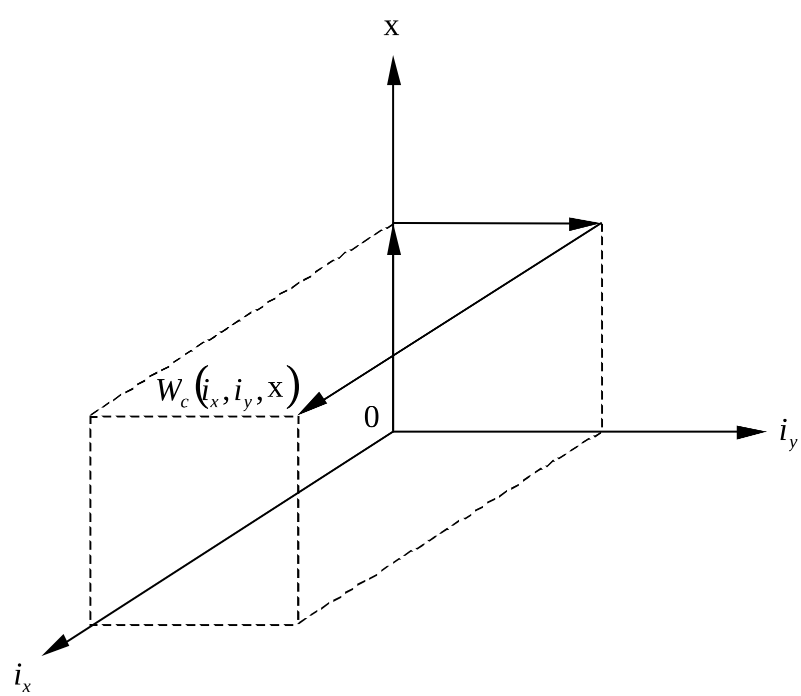

Fig. 3.1 Integration path to obtain $W_c(i_x, i_y, x)$

The coenergy can be found by integrating (3.15) along a path of integration. The most convenient integration path is to integrate over x holding i_x and i_y fixed at zero, integrate over i_y by holding i_x fixed at zero, and finally integrate over i_x as shown in Fig. 3.1. In the first part of the integration, the integral is zero because F_e is zero when both i_x and i_y are zeros. Thus, the coenergy is calculated as,

$$\begin{aligned} W_c(i_x, i_y, x) &= \int_0^{i_y} \lambda_y(0, \xi, x) d\xi + \int_0^{i_x} \lambda_x(\xi, i_y, x) d\xi \\ &= \int_0^{i_y} (L_y \xi) d\xi + \int_0^{i_x} (L_x \xi) d\xi \\ &= \frac{1}{2} L_x i_x^2 + \frac{1}{2} L_y i_y^2 \end{aligned} \tag{3.16}$$

Where ξ is an integration variable. Then, the propulsion force F_e is calculated as,

$$F_e = \left. \frac{\partial W_c(i_x, i_y, x)}{\partial x} \right|_{i_x, i_y \ fixed} = \frac{1}{2} g_x i_x^2 + \frac{1}{2} g_y i_y^2 \tag{3.17}$$

Now F_e is expressed in terms of state variables, i_x and i_y, and the rate of change of phase inductance, g_x and g_y. The force equation in terms of the phase currents is relatively simple compared to voltage equation and hence it will be used to derive the force distribution function (FDF) described in the following section.

3.3 Control Strategy for Prototype LSRM Elevator

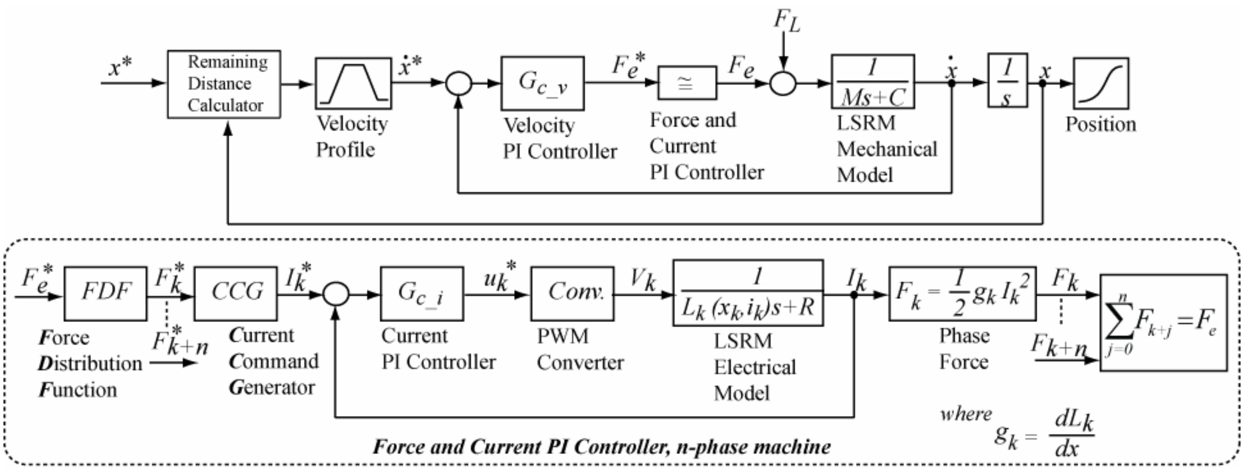

Fig. 3.2 Control block diagram for the prototype LSRM elevator.

For an elevator application, the prototype needs a precise control strategy consisting of force, current, velocity, and position control as shown in Fig. 3.2. Force control with a proposed FDF is explained and verified by comparing the proposed force control method with conventional ones in this section. A trapezoidal velocity profile is presented for position control to obtain a desired response with respect to position. A position feedback is used to give position information to the velocity profile and it is represented as ‘Remaining Distance Calculator’ in Fig. 3.2. In addition, current and velocity control with the proportional plus integral (PI) control for the prototype elevator are analyzed and explained in this section.

3.3.1 Force Control

Current control is the innermost loop followed by the force control. As shown in Fig. 3.2, force control includes a current control loop with FDF applied to generate a demanding current command. As mentioned earlier, LSRMs are known for large force ripple. However, force ripple of LSRMs needs to be suppressed to control the moving vehicle properly for a smooth ride in vertical motion applications. Otherwise, mechanical oscillations and vibrations are easily instigated so that the vehicle cannot ascend and descend properly at the desired speed. For the prototype elevator, a novel FDF is implemented because of its superior performance even in large scale (or high inductance) LSRM actuation systems [1]. The proposed FDF is compared with conventional force control algorithms in this section so that the advantages of using it can be demonstrated. First, the LSRM's dynamic equation in terms of force using (3.8) through (3.11) is introduced to derive the FDF function.

The applied voltage, v_k, to a phase is equal to the sum of the resistive voltage drop and the rate of the flux linkages and is expressed in [20] as,

$$v_k = R_s i_k + \frac{d\lambda_k(x,i_k)}{dt} = R_s i_k + \left(L_k(x,i_k)\frac{di_k}{dt} + i_k \frac{dx}{dt}\frac{dL_k(x,i_k)}{dx} \right) \tag{3.18}$$

where the phase flux linkage $\lambda_k(x,i_k) = L_k(x,i_k)i_k$ and L_k is the phase inductance dependent on position *x* and phase current i_k. *k* indicates phase a, b, c, and d. R_S is the phase resistance. From (3.18), multiplying with phase current results in instantaneous phase input power p_{ik} given by,

$$\begin{aligned} p_{ik} &= v_k i_k = R_s i_k^2 + \frac{d\lambda_k}{dt} i_k = R_s i_k^2 + i_k \left(L_k(x,i_k)\frac{di_k}{dt} + i_k \frac{dx}{dt}\frac{dL_k(x,i_k)}{dx} \right) \\ &= R_s i_k^2 + \frac{d}{dt}\left(\frac{1}{2} L_k(x,i_k) i_k^2 \right) + \frac{1}{2} i_k^2 \frac{dx}{dt}\frac{dL_k(x,i_k)}{dx} \end{aligned} \tag{3.19}$$

The last term of (3.19) is the air gap power per phase, p_{ak}, and is given as,

$$p_{ak} = \frac{1}{2} i_k^2 \frac{dx}{dt}\frac{dL_k(x,i_k)}{dx} = \frac{1}{2} i_k^2 \frac{dL_k(x,i_k)}{dx}\dot{x} \tag{3.20}$$

The air gap power is the product of the electromagnetic force per phase, F_{ek}, and translator velocity given by,

$$p_{ak} = \dot{x} F_{ek} \tag{3.21}$$

From the above equation, the propulsion force per phase is acquired by equating (3.20) with (3.21) as,

$$F_{ek} = \frac{1}{2} i_k{}^2 \frac{dL_k(x, i_k)}{dx} \tag{3.22}$$

This result shows a single phase form of the propulsion force compared to (3.17) which is for two-phase excitation and is derived from the coenergy. From (3.22), the phase current command $i_k{}^*$ is calculated as,

$$i_k{}^* = \sqrt{\frac{2F_{ek}{}^*}{g_k}} \tag{3.23}$$

where $F_{ek}{}^*$ is a propulsion force command per phase which would be excited and $g_k = dL_k(x,i_k)/dx$ is the rate of change of phase inductance with respect to position. Equation (3.23) is called CCG which is shown in Fig. 3.2. In addition, the mechanical equation is represented as the following,

$$F_e = \sum_{k=a}^{d} F_{ek} = M \frac{d\dot{x}}{dt} + C\dot{x} + F_L \tag{3.24}$$

where,

$$\begin{aligned} &F_e = generated\ \ propulsion\ \ force,\ F_L = Load\ force, M = mass \\ &C = \ friction\ coefficient\ for\ k\ =\ a, b, c, d\ phase \end{aligned}.$$

Equations (3.22) and (3.23) indicate that the required propulsion force needs to be controlled by effectively generating demanding current command through a well-behaved FDF. Next section discusses the concept of the force distribution function (FDF) and compares conventional FDFs presented by Bae *et al.* [5][36] and by Schramm *et al.* [21] with a novel FDF proposed by the author [1].

3.3.1.1 Force Distribution Function (FDF)

The block diagram shown at the bottom of Fig. 3.2 illustrates a force and current control loop. It is composed of a force distribution function (FDF), a current command generator (CCG), a current controller, and propulsion force calculators. Assuming that instantaneous phase currents are controlled accurately, the force control strategy is based on tracking the optimum FDF of each phase, which is generated using a required force command obtained from the velocity control loop. In order to achieve the required force command, the force distribution function should satisfy the following condition: the sum of the FDFs for all phases should be equal to unity at all translator positions. The relations between the force command and force distribution function are given as,

$$F_{ek}^{\ *} = F_e^* f_k \tag{3.25}$$

$$F_e^{\ *} = \sum_{k=a}^{d} F_{ek}^* = \sum_{k=a}^{d} \left(F_e^* f_k \right) = F_e^* \sum_{k=a}^{d} \left(f_k \right) = F_e^* \cdot 1 = F_e^* \tag{3.26}$$

where $F_e^{\ *}$ is the required propulsion force command and f_k is a FDF for $k=a,b,c,d$ phase. From (3.23) and (3.25), provided that an effectively distributed phase force $F_{ek}^{\ *}$ is given by using a well-devised FDF method, an efficient phase current command $i_k^{\ *}$ can be generated from the given phase force command $F_{ek}^{\ *}$ and hence high performance of force control can be achieved. In the following section, two conventional FDFs are presented and compared with the proposed FDF through dynamic simulations.

3.3.1.2 Conventional FDF: Single-phase Excitation

According to the allocation of FDF per phase, there exist two different force control strategies: that is, single-phase excitation and two-phase excitation. As one of the single-phase excitation, Schramm *et al.* [21] is chosen due to phase current optimal profiling in the sense of minimum stator copper loss. In Table 3.1, *A= 9mm, B=22mm, C=35mm, and D= 48mm* based on the prototype LSRM with a cycle of 52mm. The commutation position, A through D, is based

Table 3.1 Single-phase excitation

FDF	Implementation	Position
f_k	$f_a = 1$, $f_b = f_c = f_d = 0$	$0 \le x < A$
	$f_b = 1$, $f_a = f_c = f_d = 0$	$A \le x < B$
	$f_c = 1$, $f_a = f_b = f_d = 0$	$B \le x < C$
	$f_d = 1$, $f_a = f_b = f_c = 0$	$C \le x < D$

on the optimal position where the minimum stator copper loss takes place according to Schramm *et al.*'s method.

3.3.1.3 Conventional FDF: Two-phase Excitation

For the case of two-phase excitation, Bae *et al.* [5,36] is selected because it is reported that the FDF performs well in both case of LSRM [5] and RSRM [36]. In Table 3.2, *A= 13mm, B=26mm, C=38mm, and D= 52mm* based on the prototype LSRM with a cycle of 52mm. The commutation position, A through D, is given at the position where the phase propulsion force profile starts producing a positive force. In the table, $g_k = dL_k(x,i_k)/dx$, the rate of change of inductance with respect to position.

3.3.1.4 Proposed Force Distribution Function

Since the conventional FDF [5] of two-phase excitation has a slow response due to a heavy weight function of the FDF, a novel FDF is proposed by the author in [1] and shown in Table 3.3. The only difference between the two FDFs is the weight function: The conventional FDF uses $f_k = g_k(x)^2 / \left(g_k(x)^2 + g_{k+1}(x)^2\right)$, but the proposed one $f_k = |g_k(x)| / \left(|g_k(x)| + |g_{k+1}(x)|\right)$. Based on the equation (3.23), the proposed FDF with a combination of absolute value of g_k causes the current command to rise much quickly compared to the one of Bae *et al.* [3] for a given phase propulsion force, F_{ek}^*, and hence enables the actual phase current to be excited fast

Table 3.2 Two-phase excitation of Bae *et al*. [5,36]
(Used by permission of Dr. Bae)

FDF	Implementation	Position
f_k	$f_d = g_d(x)^2/\left(g_a(x)^2 + g_d(x)^2\right),\ f_a = g_a(x)^2/\left(g_a(x)^2 + g_d(x)^2\right)$ $f_b = f_c = 0$	$0 \le x < A$
	$f_a = g_a(x)^2/\left(g_a(x)^2 + g_b(x)^2\right),\ f_b = g_b(x)^2/\left(g_a(x)^2 + g_b(x)^2\right)$ $f_c = f_d = 0$	$A \le x < B$
	$f_b = g_b(x)^2/\left(g_b(x)^2 + g_c(x)^2\right),\ f_c = g_c(x)^2/\left(g_b(x)^2 + g_c(x)^2\right)$ $f_a = f_d = 0$	$B \le x < C$
	$f_c = g_c(x)^2/\left(g_c(x)^2 + g_d(x)^2\right),\ f_d = g_d(x)^2/\left(g_c(x)^2 + g_d(x)^2\right)$ $f_a = f_b = 0$	$C \le x < D$

Table 3.3. The proposed FDF for the prototype LSRM elevator

FDF	Implementation	Position
f_k	$f_d = \lvert g_d(x)\rvert/\left(\lvert g_d(x)\rvert + \lvert g_a(x)\rvert\right),\ f_a = \lvert g_a(x)\rvert/\left(\lvert g_d(x)\rvert + \lvert g_a(x)\rvert\right)$ $f_b = f_c = 0$	$0 \le x < A$
	$f_a = \lvert g_a(x)\rvert/\left(\lvert g_a(x)\rvert + \lvert g_b(x)\rvert\right),\ f_b = \lvert g_b(x)\rvert/\left(\lvert g_a(x)\rvert + \lvert g_b(x)\rvert\right)$ $f_c = f_d = 0$	$A \le x < B$
	$f_b = \lvert g_b(x)\rvert/\left(\lvert g_b(x)\rvert + \lvert g_c(x)\rvert\right),\ f_c = \lvert g_c(x)\rvert/\left(\lvert g_b(x)\rvert + \lvert g_c(x)\rvert\right)$ $f_a = f_d = 0$	$B \le x < C$
	$f_c = \lvert g_c(x)\rvert/\left(\lvert g_c(x)\rvert + \lvert g_d(x)\rvert\right),\ f_d = \lvert g_d(x)\rvert/\left(\lvert g_c(x)\rvert + \lvert g_d(x)\rvert\right)$ $f_a = f_b = 0$	$C \le x < D$

enough to tract the current command. Thus, the generated propulsion force, F_e, for a quickly excited phase current is able to successfully track the demanding force command, F_e*, which is coming out of velocity controller as shown in Fig. 3.2. The comparison results of the FDFs are presented in the next section. In Table 3.3, *A= 13mm, B=26mm, C=38mm, and D=52mm* based on the prototype LSRM with a cycle of 52mm. The commutation position, A through D, is given at the position where the phase propulsion force profile starts producing a positive force. In the table, $g_k = dL_k(x,i_k)/dx$, the rate of change of inductance according to position.

3.3.1.5 Comparison of the FDFs

Case 1: Single-phase Excitation [21] vs. the Proposed FDF

In Fig. 3.3, dynamic simulation results show the excellence of the proposed FDF compared with a conventional single phase excitation called optimal single phase excitation [21]. For this simulation, specification of the prototype LSRM described in the previous chapter is used. The conventional single-phase excitation with the FDF shown in Table 3.1 shows a large force error during commutation while the proposed FDF presents a negligible force error. The simulation results are summarized in Table 3.4. On the peak phase current, the phase currents are limited to a certain maximum value because of converter ratings. Hence, high peak phase currents increase the cost of converter. With the superior performance and lower current rating, the proposed FDF is utilized for an efficient force control of the prototype elevator.

Table 3.4 Comparison between the proposed FDF and conventional single-phase excitation

	Proposed FDF	Conventional excitation
Peak Force Command	112N	158N
Peak Force Error	- 4 N	- 137N
Peak Phase Current	9.7A	12.8A

Case 2: Two-phase Excitation [5] vs. the Proposed FDF

For this simulation, the specification of the LSRM described in the previous chapter for the ship elevator application is used [1]. The ship elevator as a high volume of application needs a high propulsion force of 55kN. Fig.3.4 (a) shows the result of force control using THE conventional FDF [5]. As can be seen, fluctuations of the produced force are large from the force command. It results in large force errors, up to -420 N. According to the equation (3.25), the distributed force is generated by using FDF, and then the current command is derived from the distributed force as shown in (3.23). Therefore, if the FDF has a large weight function like Bae *et al*'s FDF, the distributed force has a slow response. As a result, the current rises up slowly, and the generated force is not able to track the commanded force fast enough. Therefore, a large force error is present. Fig. 3.4 (b) shows the result of force control with the proposed FDF shown in Table 3.3 and gives a superior result to the one of force control with the conventional FDF in terms of force ripple and peak phase current. The force error is reduced down to 55 N which is roughly eight times less than the force error in using the conventional FDF. The comparison results are summarized in Table 3.5.

In summary, the simulation results from Fig. 3.3 and 3.4 indicate that the proposed FDF is a suitable method for the efficient force control in the application of elevator which needs a high propulsion force or small.

Table 3.5 Comparison between the proposed FDF and conventional two-phase excitation

	Proposed FDF	Conventional excitation
Peak Force Command	975N	1,112N
Peak Force Error	55 N	- 420N
Peak Phase Current	7A	7.9A

3.3.2 Current Control

From (3.18), the phase current equation is derived as,

$$pi_k = -a_{1k} i_k - a_{2k} \dot{x} i_k + a_{0k} v_k \tag{3.27}$$

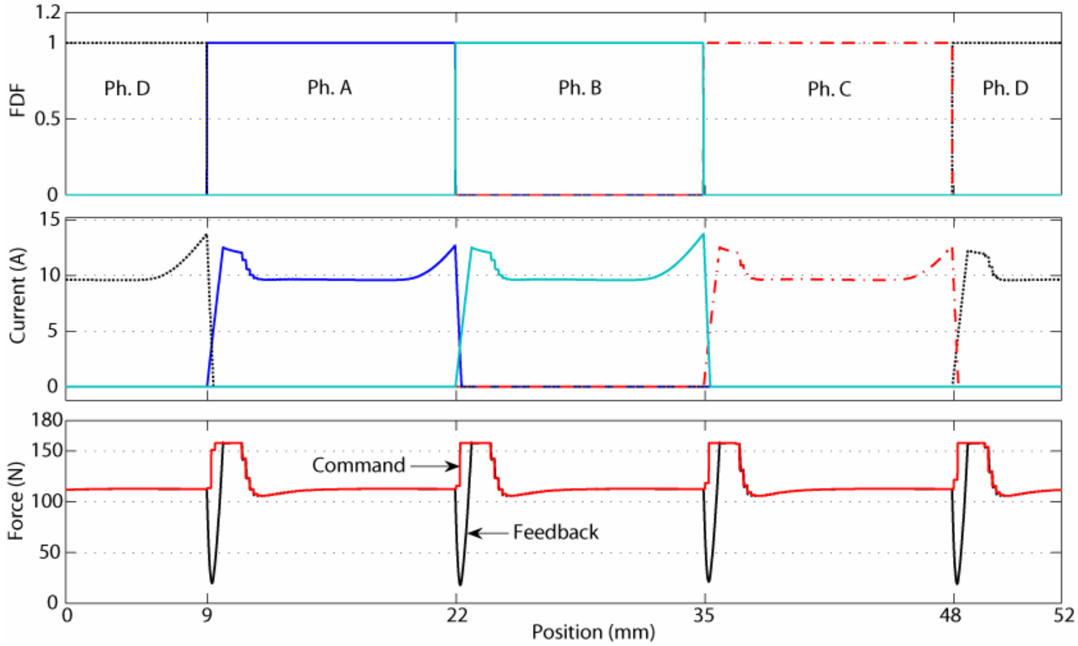

(a) Force control with a conventional FDF [21]

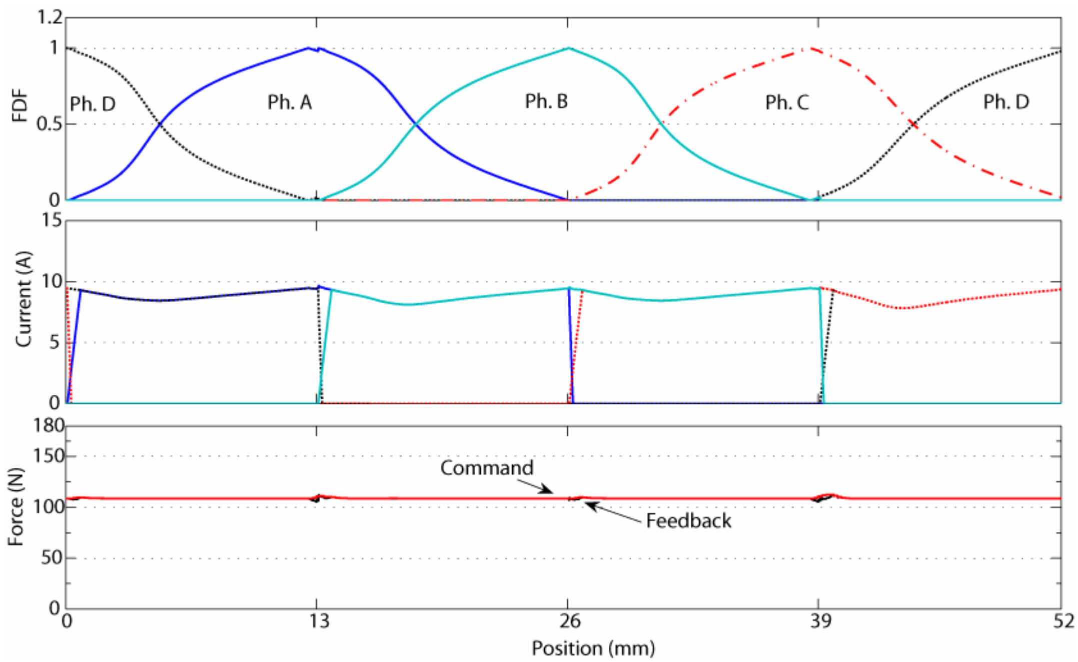

(b) Force control with the proposed FDF

Fig. 3.3 comparison of force control with a single-phase excitation FDF

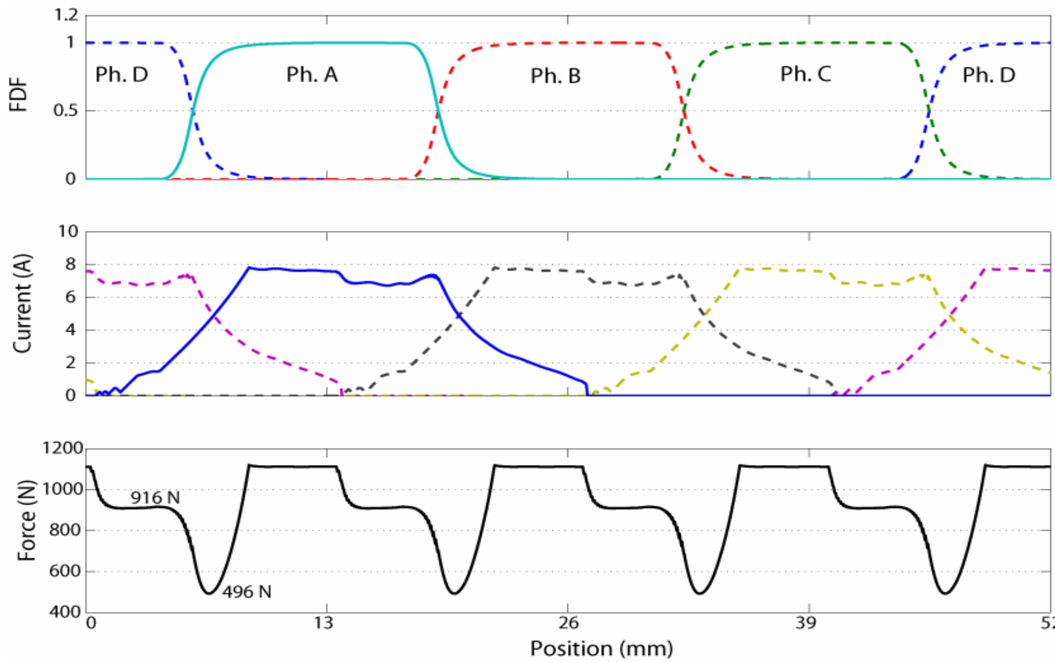

(a) Force control with a conventional FDF [5]

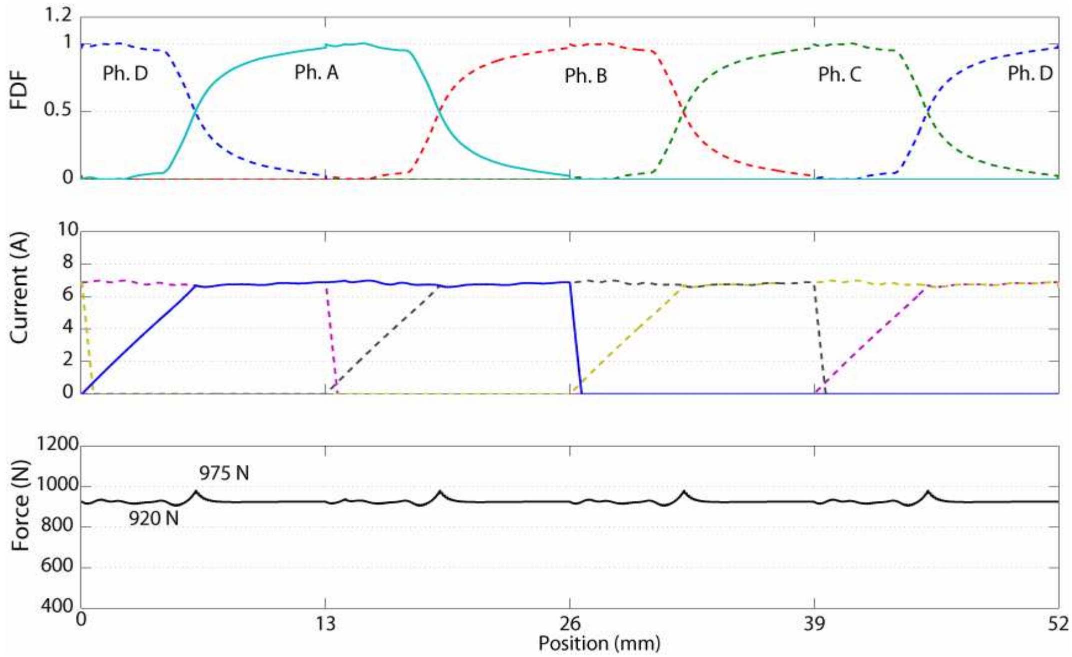

(b) Force control with the proposed FDF

Fig. 3.4 comparison of force control with a two-phase excitation FDF

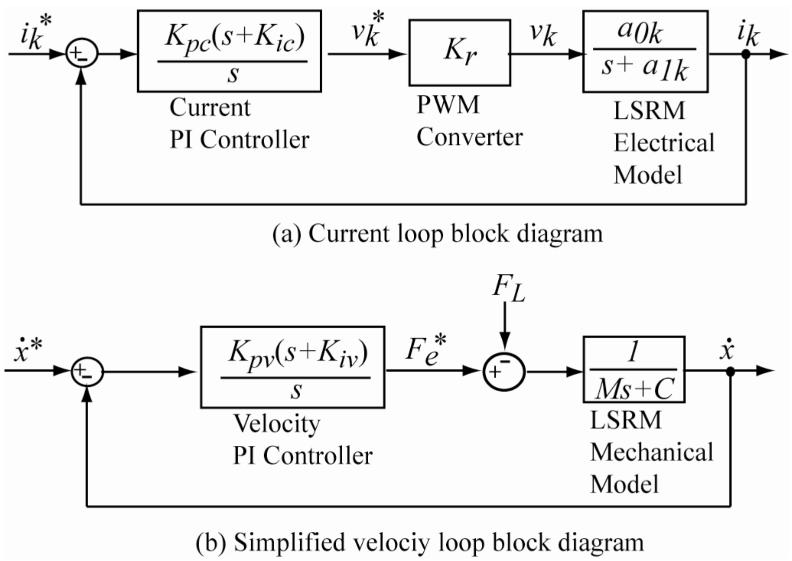

Fig. 3.5. Control block diagram with current and velocity PI controller

where $a_{0k} = 1/L_k(x,i_k), a_{1k} = R_s/L_k(x,i_k), a_{2k} = g_k/L_k(x,i_k),$ and $p=d/dt$ for $k=a, b, c, d$ phase. The input phase voltage, v_k, needs to be adjusted to control the phase current. As developed in [47], the new current control input u_k, is given as using a PI controller,

$$u_k = K_{pc}\left[\left(i_k^* - i_k\right) + K_{ic}\int_0^t \left(i_k^* - i_k\right) d\tau\right] \tag{3.28}$$

where K_{pc} and K_{ic} are the proportional and integral gains of the PI current controller, respectively. From Fig. 3.5(a), the transfer function of the current control loop is derived and simplified as,

$$G_c(s) \equiv \frac{i_k(s)}{i_k^*(s)} \cong \frac{K_1 K_{pc} s + K_1 K_{pc} K_{ic}}{s^2 + K_1 K_{pc} s + K_1 K_{pc} K_{ic}} \quad for\ a_{0k} K_r K_{pc} >> a_{1k} \tag{3.29}$$

where K_r is the converter gain and $K_1 = a_{0k}K_r$. From a given bandwidth ω_c and damping ratio ζ_c for the current control loop, the gains are derived as,

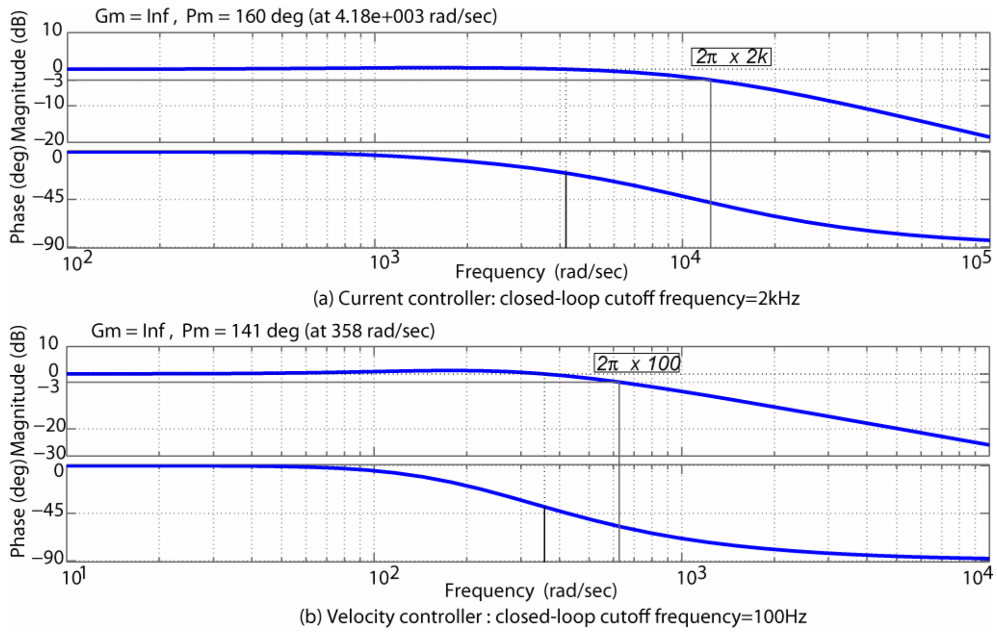

Fig. 3.6. Frequency response of velocity and current controller (**Gm** represents gain margin and **Pm** phase margin)

$$K_{pc}(x) = \frac{2\zeta_c \omega_c}{\sqrt{\left(1+2\zeta_c^2\right)+\sqrt{\left(1+2\zeta_c^2\right)^2+1}}} \cdot \frac{1}{K_1(x)} \tag{3.30.1}$$

$$K_{ic} = \frac{\omega_c}{2\zeta_c \sqrt{\left(1+2\zeta_c^2\right)+\sqrt{\left(1+2\zeta_c^2\right)^2+1}}} \tag{3.30.2}$$

As a result, the PI velocity controller gains are calculated by using the method described in [47]. For the current controller, 2kHz and 2 are selected for the bandwidth ω_c and the damping ratio ζ_c, respectively. Even though K_1 is a variable dependent on phase inductance L_k in (3.30.1), the control performance of the transfer function (3.29) does not depend on K_1 because K_1K_{pc} becomes a constant in the function. In addition, Fig. 3.7 shows that the inductance profile of the designed LSRM is almost the same up to the maximum phase current 12A due to a large air gap, 1.5mm. Fig. 3.6(a) shows the frequency response of the closed-loop transfer function (3.29) with the PI controller gains obtained for given ω_c and ζ_c, regardless of K_1. It is seen that the designed current controller is stable due to the high gain and phase margins, and the closed-loop cutoff frequency is 2kHz proving the design process discussed above.

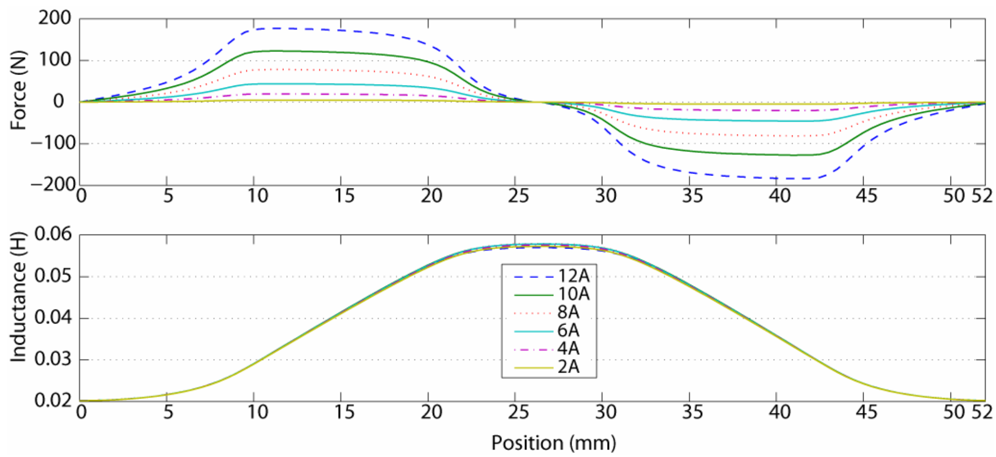

Fig. 3.7. FEA data of the LSRM: Force and inductance profiles

3.3.3 Velocity Control

Since the current loop bandwidth is much higher than the speed loop bandwidth and with the assumption that $i_k^* \cong i_k$ or $F_x^* \cong F_x$ as shown in Fig. 3.2, velocity loop is simplified as shown in Fig. 3.5(b) and the transfer function is expressed with PI controller gains as,

$$G_v = \frac{\dot{x}(s)}{\dot{x}^*(s)} \cong \frac{\dfrac{K_{pv}(s+K_{iv})}{M}}{s^2 + (\dfrac{K_{pv}}{M})s + \dfrac{K_{pv}K_{iv}}{M}} \quad for\ K_{pv} >> C \tag{3.31}$$

where K_{pv} and K_{iv} are the proportional and integral gains of the velocity PI controller, respectively. A general second order system can be derived from the simplified velocity transfer function for a given set of the desired velocity loop bandwidth ω_v and damping ratio ζ_v as described in [47]. From a given set of ω_v and ζ_v

$$K_{pv} = \frac{2\zeta_v \omega_v M}{\sqrt{(1+2\zeta_v^2) + \sqrt{(1+2\zeta_v^2)^2 + 1}}} \tag{3.32.1}$$

$$K_{iv} = \frac{\omega_v}{2\zeta_v \sqrt{\left(1+2\zeta_v^2\right)+\sqrt{\left(1+2\zeta_v^2\right)^2+1}}} \tag{3.32.2}$$

As a result, the PI velocity controller gains are calculated using the method described in previous section. Since it is known that velocity control loop is slower by five to ten times than current control loop, 100Hz is selected as the velocity closed-loop bandwidth ω_v. In addition, the damping ratio ζ_v is set to 1. Fig. 3.6(b) shows the frequency response of the closed-loop transfer function (3.31) with the PI controller gains obtained for the given values of ω_v and ζ_v. It can be seen that the designed velocity controller is stable due to the high gain and phase margins, and the closed-loop cutoff frequency is 100Hz proving the design process discussed above.

3.3.4 Position Control

Elevator system is a vertical traverse application and it needs to avoid the vibration of car acceleration. For this reason, conventional elevator uses a desired and given trajectories of jerk, acceleration, velocity, and position [55]. Thus, the position control system for the prototype elevator employs a simple trapezoidal velocity profile in order to achieve a smooth and efficient ride without any jerky motion. The trapezoidal velocity profile consists of four periods: acceleration, coast (constant velocity), deceleration, and halt. The velocity profile mode such as deceleration is determined by the ‘Remaining distance calculator’ in Fig. 3.2. For a given final distance, x^*, and the direction of the vehicle via external control switches, the distance calculator monitors and gives the position information from the linear position encoder to the velocity profile so that the profile can start acceleration to move or deceleration to stop at a desired position. For the prototype elevator, the acceleration is set to 0.4g (g=the acceleration due to gravity, 9.8 m/s^2) and the maximum velocity to 0.3m/s. (3.33.1) and (3.33.2) describe the trapezoidal velocity profile to control position in the ascending and descending cases, For ascent,

$$\dot{x} = \begin{cases} \dot{x} + \alpha, & \text{during acceleration} \\ \max \dot{x}, & \text{during coast} \\ \dot{x} - \alpha, & \text{during desceleration} \\ 0, & \text{during holding at stopped position} \end{cases} \tag{3.33.1}$$

For descent,

$$\dot{x} = \begin{cases} \dot{x} - \alpha, & \text{during acceleration} \\ \min \dot{x}, & \text{during coast} \\ \dot{x} + \alpha, & \text{during desceleration} \\ 0, & \text{during holding at stopped position} \end{cases} \tag{3.33.2}$$

where α is the cruising speed which is set to 0.2*m/s* in case of the prototype elevator.

3.4 Converter Topology

In this section, two converter topologies, which are capable of operating in two quadrants for the prototype elevator, are compared and then the suitable one is chosen. Although a number of different configurations of converters have been proposed in literatures and have been summarized in [20], two of the most popular configurations are only considered. An asymmetric half-bridge converter considered here does not contribute to a new innovation in this research, but is the most practical and commonly used configuration in (L)SRMs. It is also the most convenient configuration to test various switching strategies for (L)SRM drives. In addition, one of the switching strategies named unipolar switching strategy presented in [22] is adopted and described in this section.

3.4.1 Comparison of Converter Topologies

The converter for the prototype LSRM should have the ability to provide a positive voltage loop to increase phase current, a negative voltage loop to decrease phase current, and a zero voltage loop to maintain the desired current level. From the existing converter topologies, two most popular converter topologies for an 8/6 LSRM are the asymmetric half-bridge converters shown in Fig. 3.8. They are capable of providing the three voltage loops [54].

Both converters are capable of operating in two quadrants. The switches and freewheeling diodes for both converters should be rated to withstand the supply voltage and switching transients. However, the current ratings of the upper switches T_{ac} and T_{bd} of the shared switch half-bridge converter must be determined to carry the sum of two phase currents. The upper switches T_{ac} and T_{bd} shown in Fig. 3.8(a) are connected to two phase windings rather than one in the asymmetric half-bridge shown in Fig. 3.8(b).

With the configuration shown in Fig. 3.8(a), the number of switches and diodes is reduced to six from eight, but it has some operational limitations. The operation of upper switches T_{ac} and T_{bd} affects both the connected phase windings. This imposes a restriction on

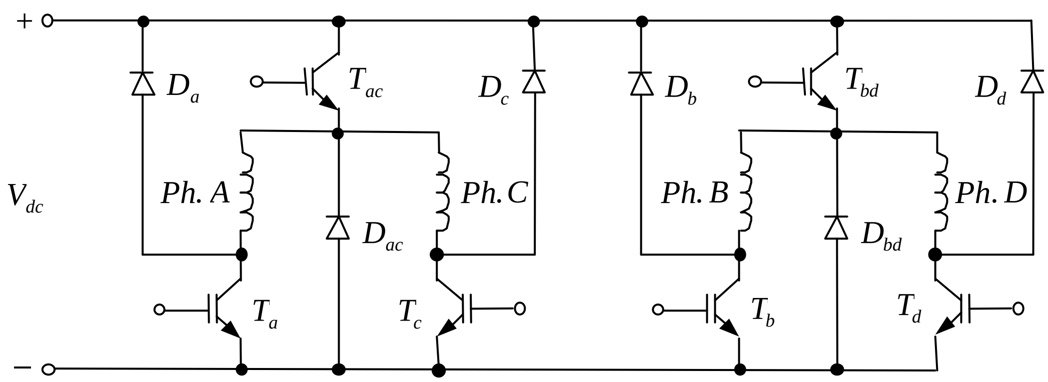

(a) Shared switch asymmetric half-bridge converter

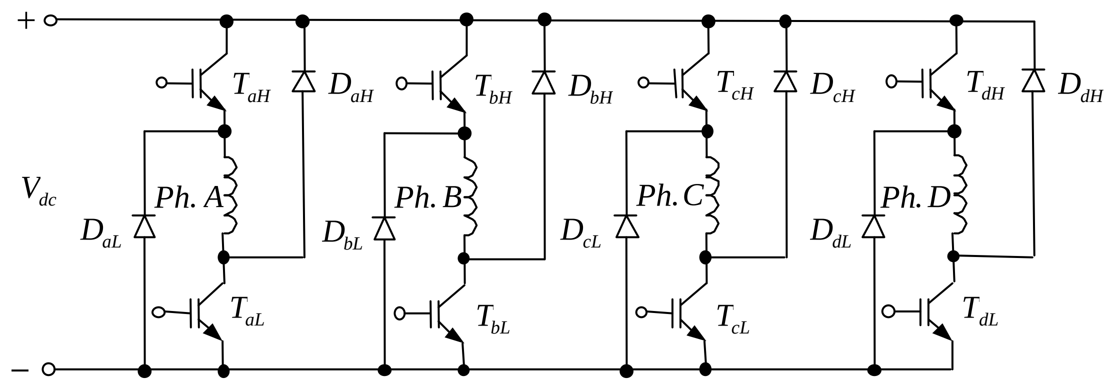

(b) Asymmetric half-bridge converter

Fig. 3.8 Possible converter topologies for the prototype LSRM

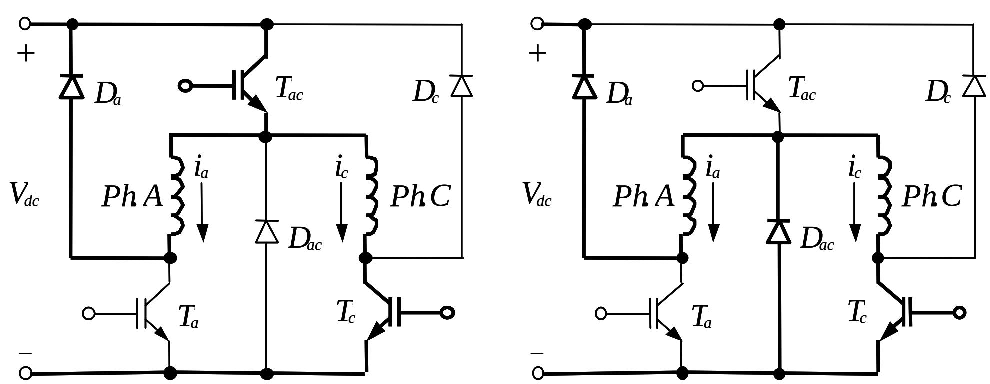

$v_a = 0$ for (T_{ac}, D_a) on
$v_c = V_{dc}$ for (T_{ac}, T_c) on

$v_a = -V_{dc}$ for (D_{ac}, D_a) on
$v_c = 0$ for (D_{ac}, T_c) on

Fig. 3.9 Example of a limited operation of the shared switch asymmetric half-bridge converter the operation of the converter because, for example, three phases cannot be operated simultaneously if the situation demands it. In other words, it is not possible to rapidly increase the current in one phase winding while rapidly decreasing the current in the other [54]. For example, when phase C is turned on while phase A current is remaining, the extinction of phase A is largely dependent on the operation of phase C as shown in Fig. 3.9. The phase A current has an increased fall time, dependent upon the chopping duty cycle of phase C. Moreover, when there is a fault in one common switch, the related two phases are not operational while the operation of each phase is independent from that of other phases in the asymmetric half-bridge converter. After reviewing the merits and demerits of these converters as shown in Table 3.6, the asymmetric half-bride converter is chosen for the prototype LSRM.

Table 3.6 Comparison of converter topologies

	Asymmetric converter in Fig. 3.8 (b)	**Shared switch converter in Fig. 3.8 (a)**
Merits	a. High fault reliability b. High control flexibility/simplicity c. Capable of various switching strategy (unipolar / bipolar…) d. Ideal for high-power application e. Equal voltage and current ratings for all power devices and diodes	a. Capable of independent phase current control b. Less than two switches per phase c. High compactness d. less sensor (two) required (only if independent control is used instead of distribution control, which means that more than two phase switches are turned on at the same time)
Demerits	a. Two devices for each phase (ex. 8 switches and 8 diodes required) b. Power loss due to the devices c. Snubber-based solution required for the minimization of power loss d. More current sensor required (four sensors)	a. Low reliability compared with asymmetric converter b. Different power ratings required for the power devices (the common switches > the phase switches) c. Applicable only to the even phase motors d. Limitation on distribution control (ex. Force distribution function)

3.4.2 Switching Strategies

To obtain less current ripple and a better frequency response in the inner current control loop of the drive system, an effective unipolar switching strategy for the half-bridge converter has been proposed by Bae *et al.* in [5] and [22], and chosen to test the prototype elevator.

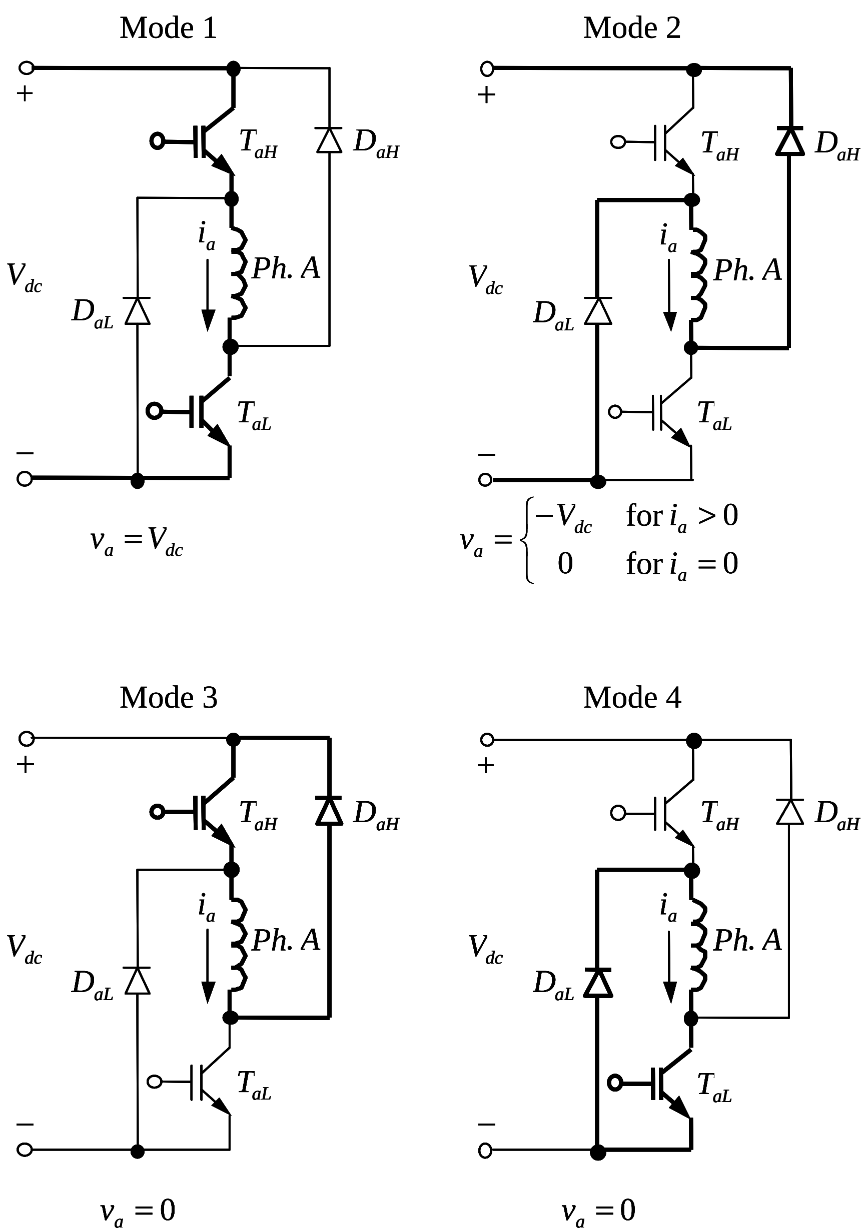

Fig. 3.10 Four possible modes of operation for phase A

With the converter shown in Fig. 3.8 (b), there are four possible modes of operation for each phase. As an illustration, these modes of operation for phase *A* are shown in Fig. 3.10. In the first mode, switches (T_{aL}, T_{aH}) are turned on with diodes (D_{aL}, D_{aH}) turned off. In this mode, v_a is equal to V_{dc} and the current in the phase winding increases rapidly, supplying energy to the phase winding. In the second mode, if $i_a > 0$, diodes (D_{aL}, D_{aH}) are turned on with switches (T_{aL}, T_{aH}) turned off in which case v_a is equal to $-V_{dc}$. Phase A current is forced to flow through both freewheeling diodes and it decreases rapidly as energy is returned from the phase winding to the supply. And if $i_a = 0$, diodes (D_{aL}, D_{aH}) and switches (T_{aL}, T_{aH}) are all turned off in which case v_a is equal to zero. In the last two modes, if $i_a > 0$ switch and diode (T_{aL}, D_{aL}) or (T_{aH}, D_{aH}) are turned on with switch and diode (T_{aH}, D_{aH}) or (T_{aL}, D_{aL}) turned off, respectively. The phase current continues to flow and decay slowly through one switch and one diode and energy is neither taken from nor returned to the DC supply. And if $i_a = 0$, diodes (D_{aL}, D_{aH}) and switches (T_{aL}, T_{aH}) are all turned off. In both cases, v_a is equal to zero.

How to exploit the modes described in Fig. 3.10 entirely depends on design specification but all possible switching strategies applicable to the converter may use some or all of the modes. The last two modes called zero voltage loops are very important in minimizing the ripple contents of the phase current at any given switching frequency. Therefore, they can reduce the hysteresis losses in the motor and the power dissipation in the DC link capacitor during any period when switches in the converter are turned on and off to reduce the net applied voltage to the phase winding.

The idea of the unipolar switching was first applied to a full-bridge converter consisting of four switches and four diodes. The full bridge converter can handle four-quadrant operation but in this application only two-quadrant operation is necessary. Therefore, with the asymmetric half-bridge converter shown in Fig. 3.8 (b) the same performance can be achieved with the unipolar switching strategy as introduced in [22]. The operational principal of the unipolar switching strategy is shown in Fig. 3.11. All possible modes are exploited in this strategy to incorporate the advantages of the conventional switching strategies presented in [8]. Due to the effectively doubled switching frequency, the ripple contents of the phase currents in the unipolar switching are enormously reduced compared to conventional switching strategies shown in [8]. In addition, fast response can be observed when the phase current is decreasing. The details are shown in [22]. The algorithm for unipolar switching and the average output voltage $[v_a]$ are as follows.

$$v_a = \begin{cases} V_{dc} & for\ v_c \geq v_{ramp}\ \&\ \text{-}v_c < v_{ramp} \\ \text{-}V_{dc} & for\ v_c < v_{ramp}\ \&\ \text{-}v_c \geq v_{ramp}\ \&\ i_a > 0 \\ 0 & elsewhere \end{cases} \tag{3.34}$$

$$\begin{aligned} &[v_a] = \frac{V_{dc}}{V_{ramp}} v_c \quad for\ \text{-}V_{ramp} \leq v_c \leq V_{ramp} \\ &-V_{dc} \leq [v_a] \leq V_{dc} \end{aligned} \tag{3.35}$$

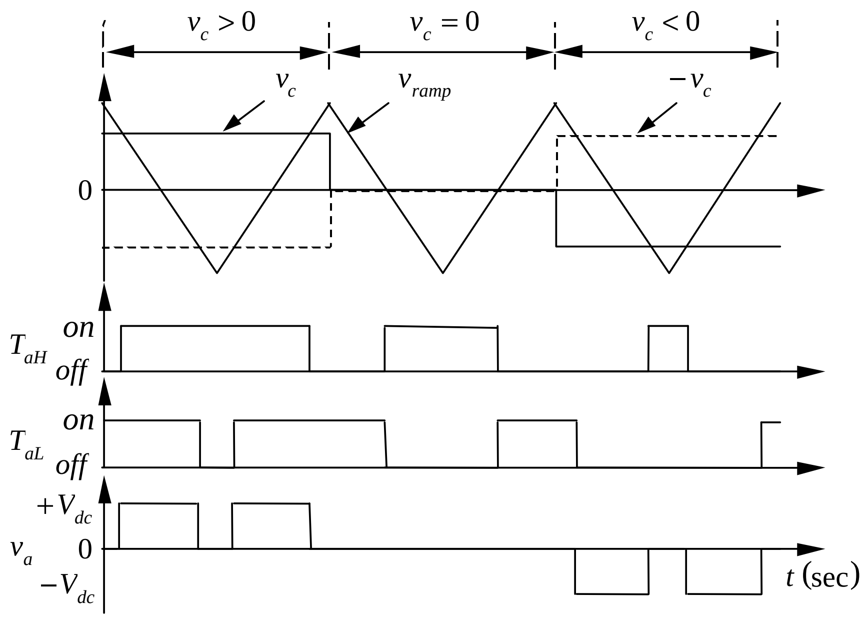

Fig. 3.11 Operational principle of the unipolar switching strategy

The unipolar switching strategy effectively doubles the switching frequency without increasing the actual switching frequency of the switches. This contributes to the mitigation of current ripple and hence to the reduction of the torque ripple. If current ripple is halved, the force ripple caused by this current ripple is reduced to one fourth of the original one because the generated force is proportional to the square of current. Moreover since the dynamics of mechanical system can be viewed as a low pass filter the dominant frequency of the force ripple is also important in that speed ripple is further deduced due to roll off over the cutoff frequency of the mechanical system. Due to these advantages, this switching strategy is applied in this research to achieve high performance in current control and thus, force control of the prototype LSRM for the elevator.

3.5 Dynamic Simulations and Experimental Results

To verify the force control algorithm using the proposed FDF along with current, velocity and position control strategies, dynamic simulations using MATLAB software and experiments using a TI TMS320F240 DSP-based control system have been exploited. The converter topology and switching strategy described in this chapter are applied for the simulations and experiments as well.

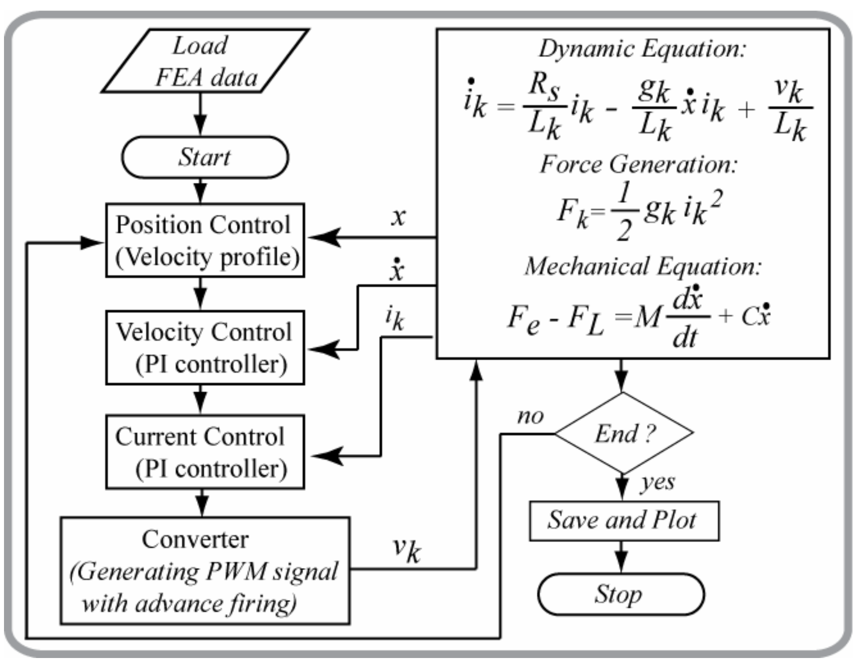

Fig. 3.12 Flow chart of the dynamic simulation

3.5.1 Dynamic Simulations

In this section, the prototype elevator using the designed LSRMs is simulated at different velocities with the proposed control strategy employed. Fig. 3.12 shows the simulation flow chart in using MATLAB software. The data for the dynamic simulation is obtained from finite element analysis (FEA) shown in Fig. 3.7. The other motor parameters and input specifications refer to the LSRM parameters summarized in the Appendix C. The deceleration command is given at 0.1m during descent and at 0.6m during ascent. The acceleration and deceleration set to 0.4g. Duration for halt at the stop position is set to one second.

Fig. 3.13 shows the simulation results for travel position, velocity, phase current and generated force of the designed LSRM at 0.15m/s with a payload of 11.5 kg per LSRM. Considering that the prototype elevator has the LSRM on each side, the total payload for the simulation is regarded as 23kg. From the results, the designed LSRM is verified that it can carry the payload of 23kg including the mass of vehicle (20.3kg) at 0.15m/s, producing excellent velocity and position control performance. For position control, the velocity profile presented in earlier section is applied, which consists of four periods: acceleration, coast, deceleration, and stay at stop position. In particular, Fig. 3.17 shows that 0.4g acceleration and deceleration of the velocity profile works well. Under continuous operation, each phase current is turned on in accordance with the FDF, and from Fig. 3.13(b) the current amplitude values during ascent and descent are 9.1A and 8.9A per phase, respectively. In addition, the average force produced is 116N during accent and 110N during descent. Fig. 3.13(b) also shows the maximum and minimum force that is produced during acceleration and deceleration. Fig. 3.14 through 3.16 show simulation results in the cases where the maximum velocity is changed from 0.2 m/s to 0.3 m/s and payload of the prototype elevator is changed from 23 kg to 32 kg in total. The simulations verify the operation of the prototype elevator under these conditions. The position where the elevator comes to a stop after deceleration is not set but depends on the velocity before deceleration. In Fig. 3.14 and 3.15 at 0.2m/s coasting velocity, the vehicle comes to a stop at 0.61m and 0.10m at top and bottom, respectively, while in Fig. 3.16 the vehicle stops at 0.61m and 0.09m at coasting velocity of 0.3m/s. The simulation results are summarized in Table 3.7.

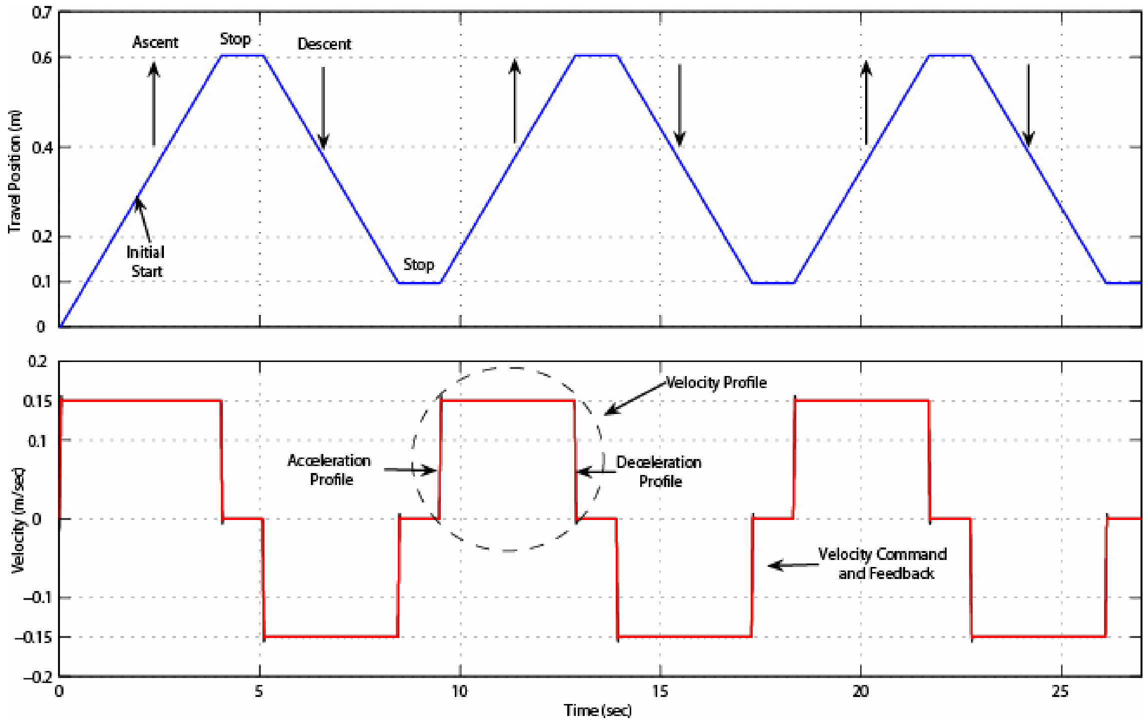

(a) Velocity and position control

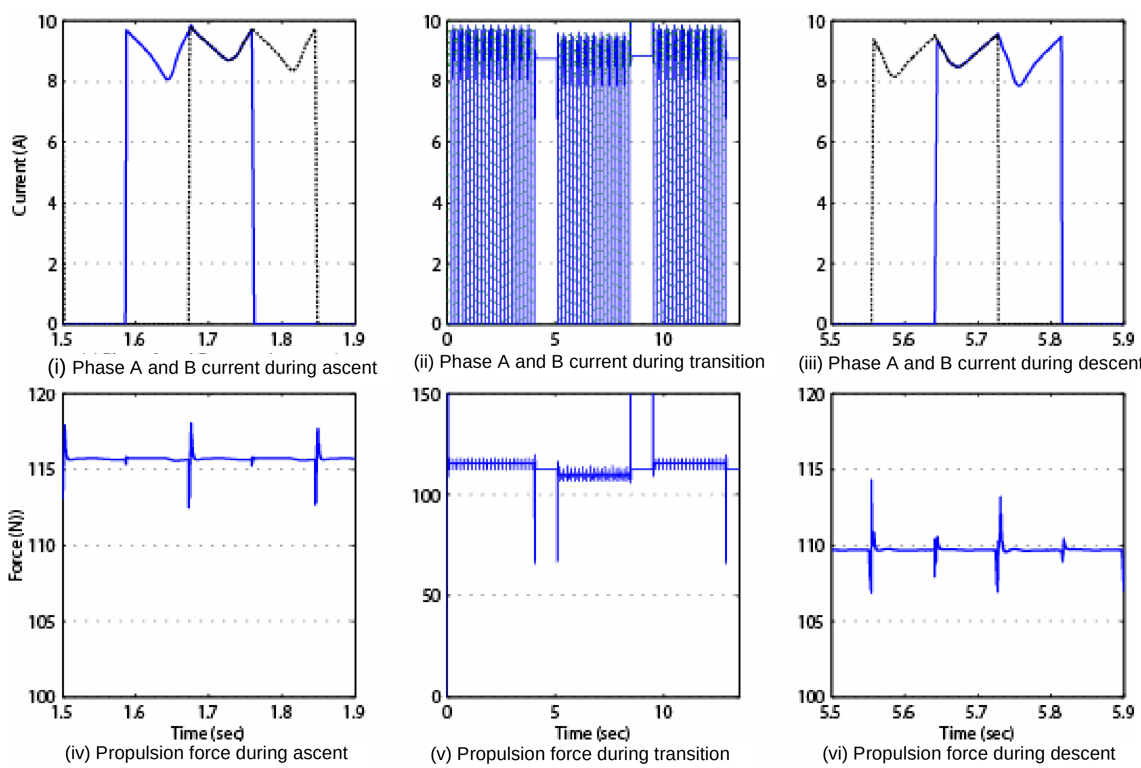

(b) Current and force control

Fig. 3.13. Simulation results using the proposed FDF at 0.15 m/s with a payload of 11.5kg *per LSRM* including the mass of the vehicle (carrying 23kg in total).

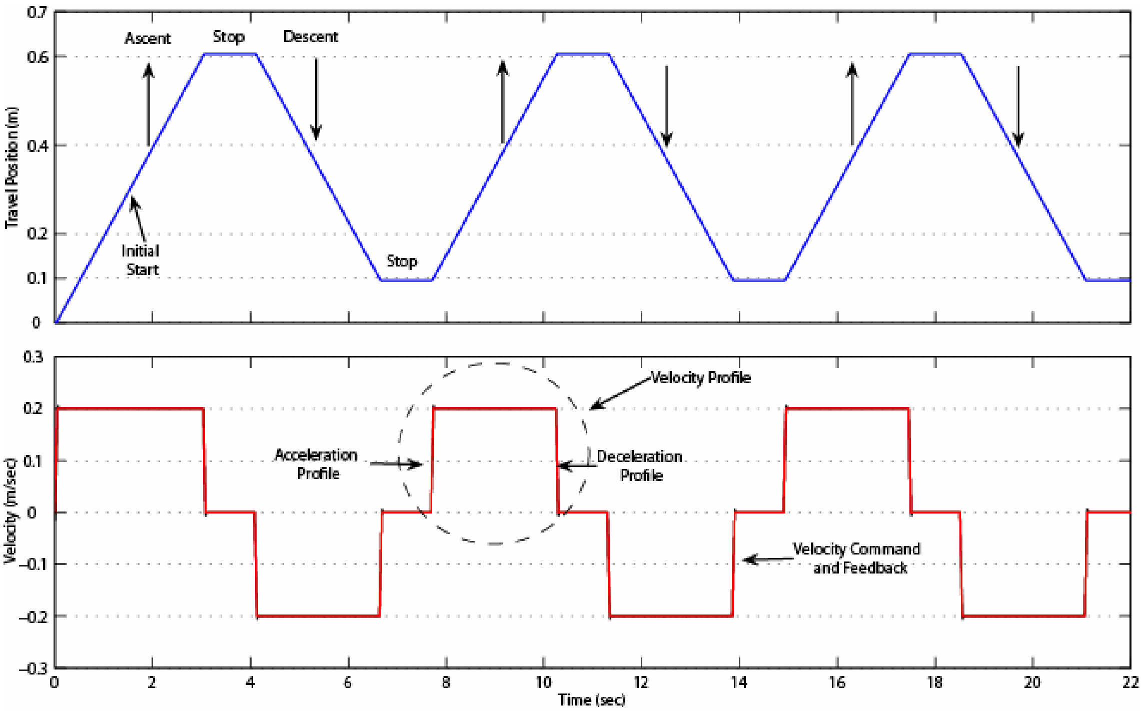

(a) Velocity and position control

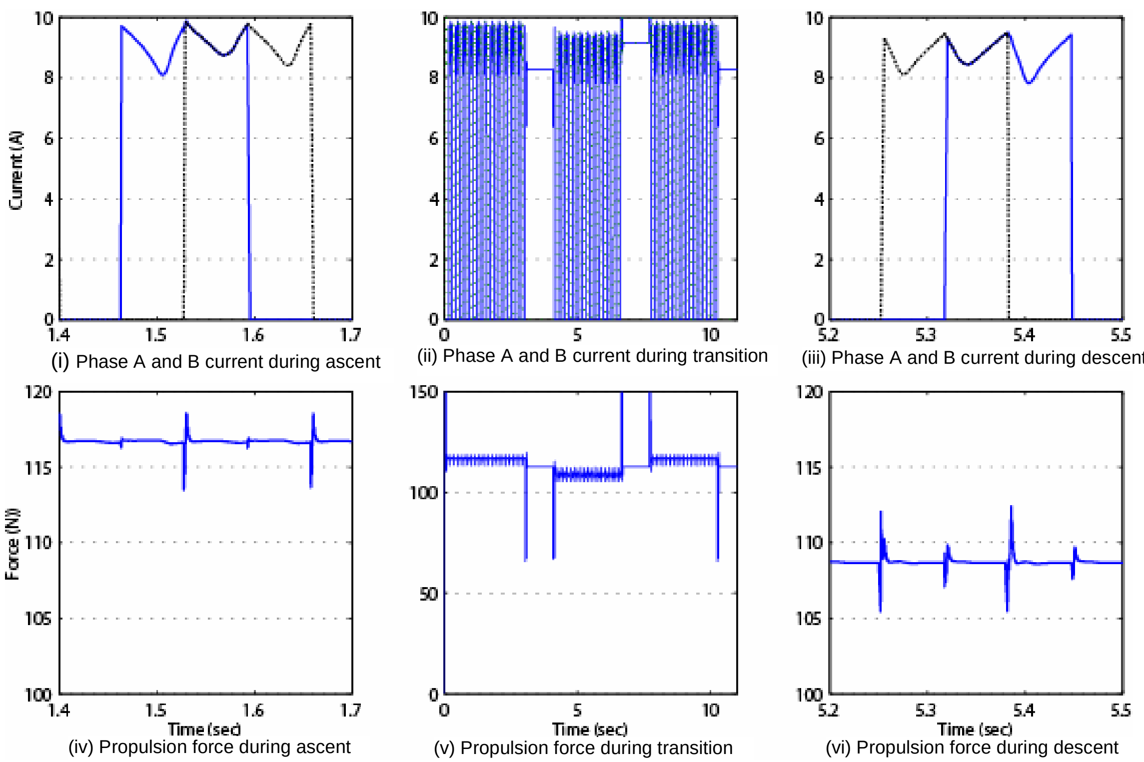

(b) Current and force control

Fig. 3.14. Simulation results using the proposed FDF at 0.2m/s with a payload of 11.5kg *per LSRM* including the mass of the vehicle (carrying 23kg in total).

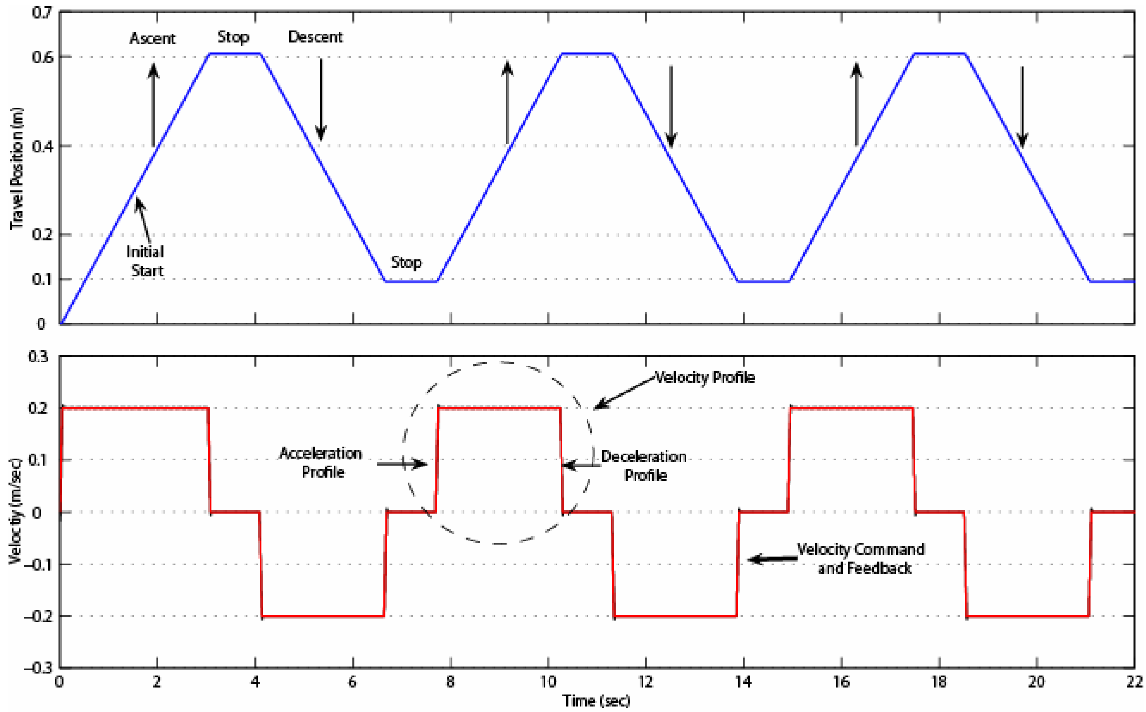

(a) Velocity and position control

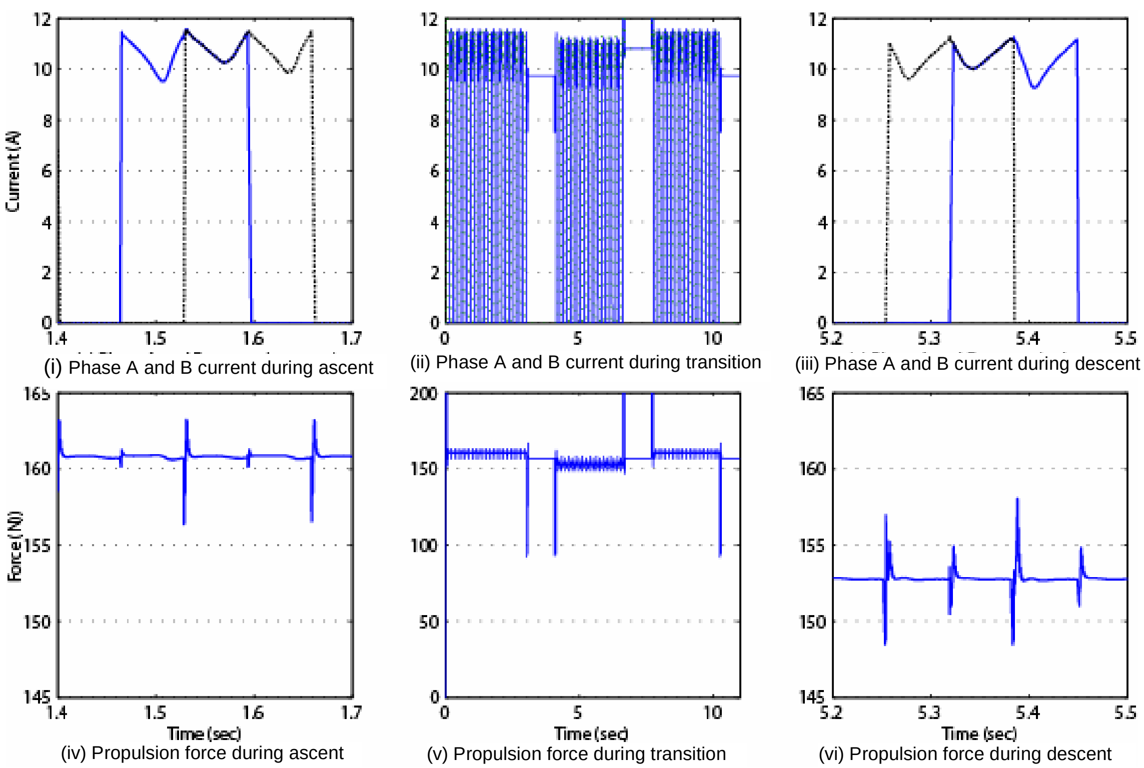

(b) Current and force control

Fig. 3.15 Simulation results using the proposed FDF at 0.2 m/s with a payload of 16kg *per LSRM* including the mass of the vehicle (carrying 32kg in total).

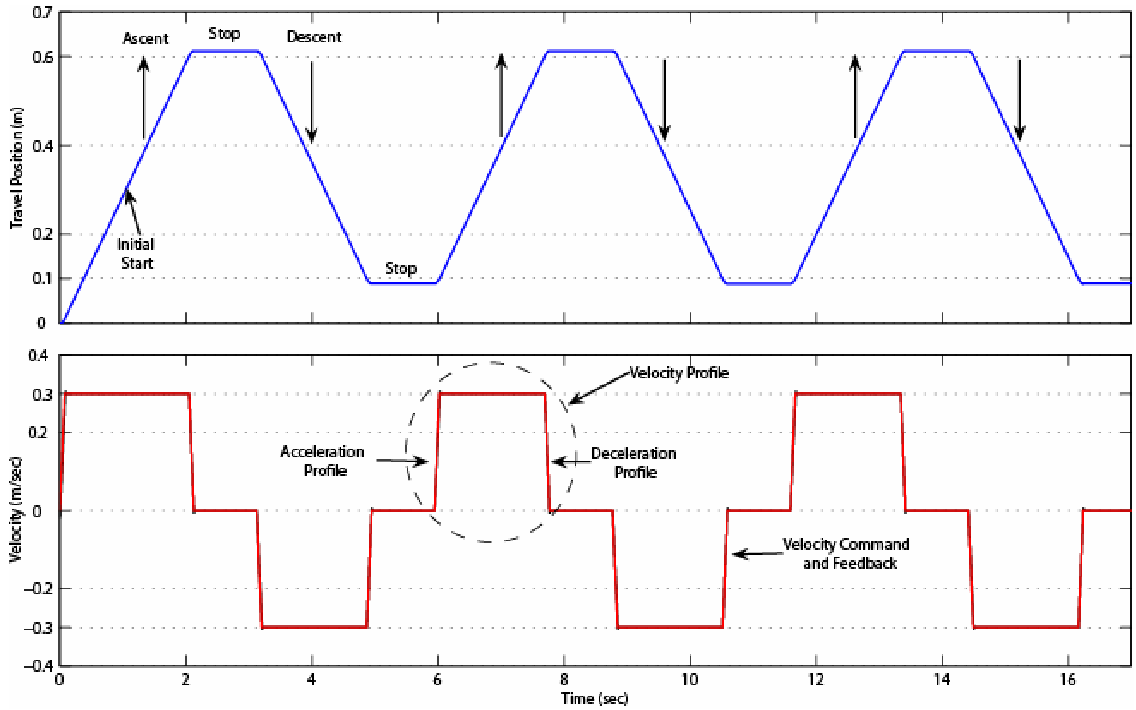

(a) Velocity and position control

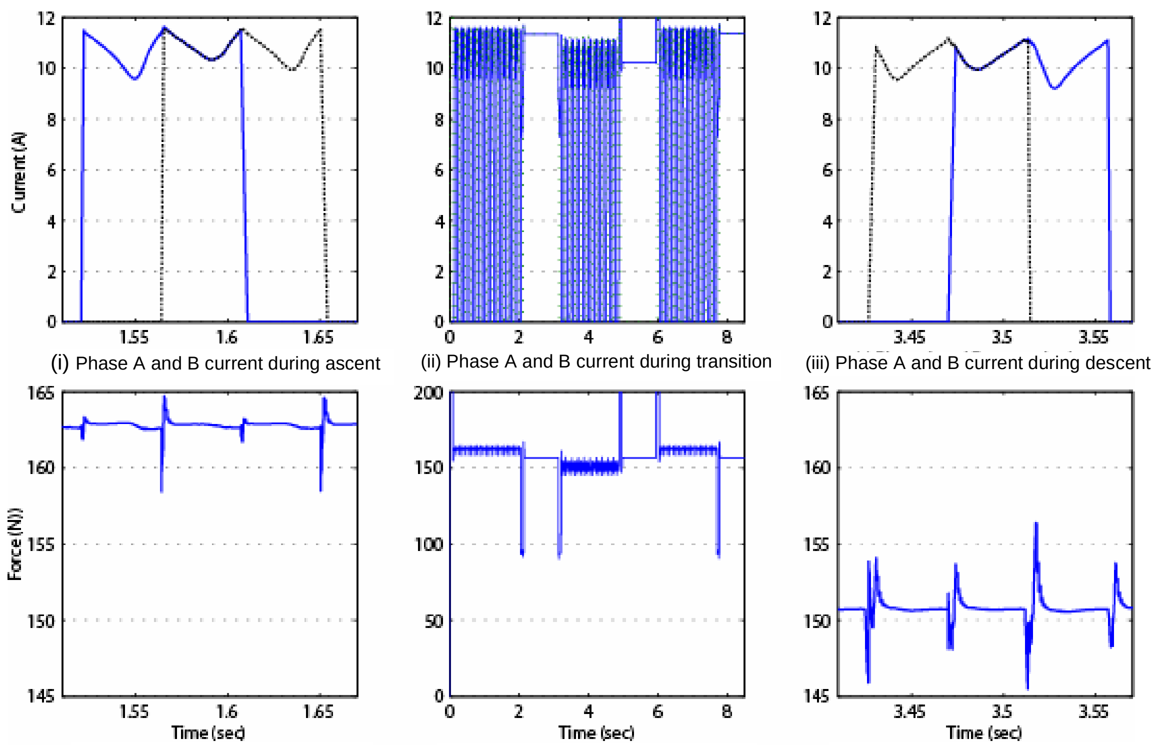

(i) Phase A and B current during ascent (ii) Phase A and B current during transition (iii) Phase A and B current during descent

(iv) Propulsion force during ascent (v) Propulsion force during transition (vi) Propulsion force during descent

(b) Current and force control

Fig. 3.16 Simulation results using the proposed FDF at 0.3 m/s with a payload of 16kg *per LSRM* including the mass of the vehicle (carrying 32kg in total).

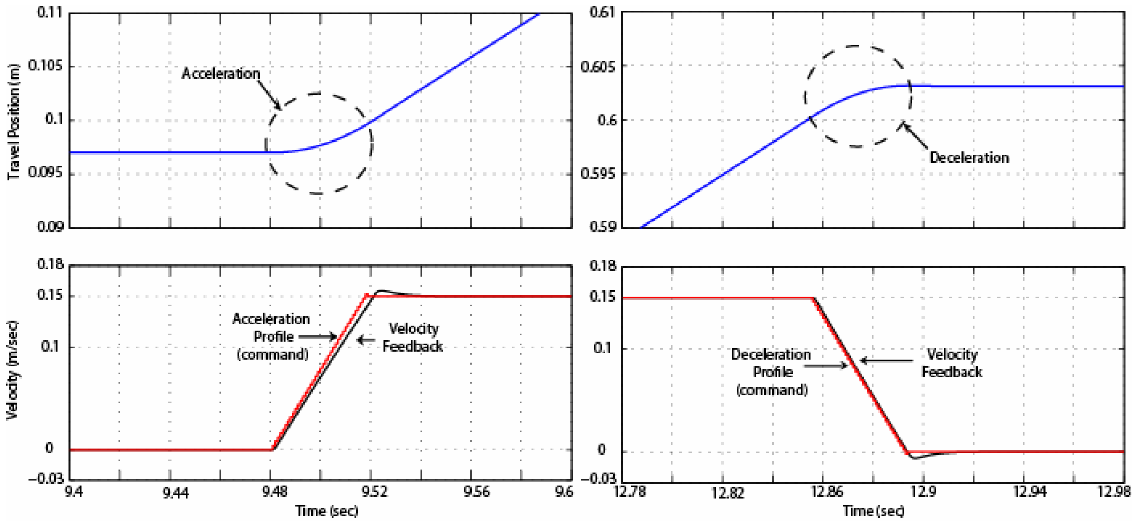

Fig. 3.17. Velocity profile using the proposed FDF at 0.15 m/s with a payload of 11.5kg *per LSRM* including the mass of the vehicle (carrying 23kg in total).

Table 3.7 Summary of the dynamic simulation results

Payload	11.5kg *per LSRM* (carrying 23kg in total)					
Velocity	0.15m/s			0.2m/s		
Period	ascent	stop	descent	ascent	stop	descent
Force (N) (Average)	116	113	110	117	113	109
Current (A) (Amplitude)	9.1	-	8.9	9.2	-	8.8
Payload	16kg *per LSRM* (carrying 32kg in total)					
Velocity	0.2m/s			0.3m/s		
Period	ascent	stop	descent	ascent	stop	descent
Force (N) (Average)	161	157	153	163	157	151
Current (A) (Amplitude)	10.7	-	10.5	10.8	-	10.4

3.5.2 Experimental Setup

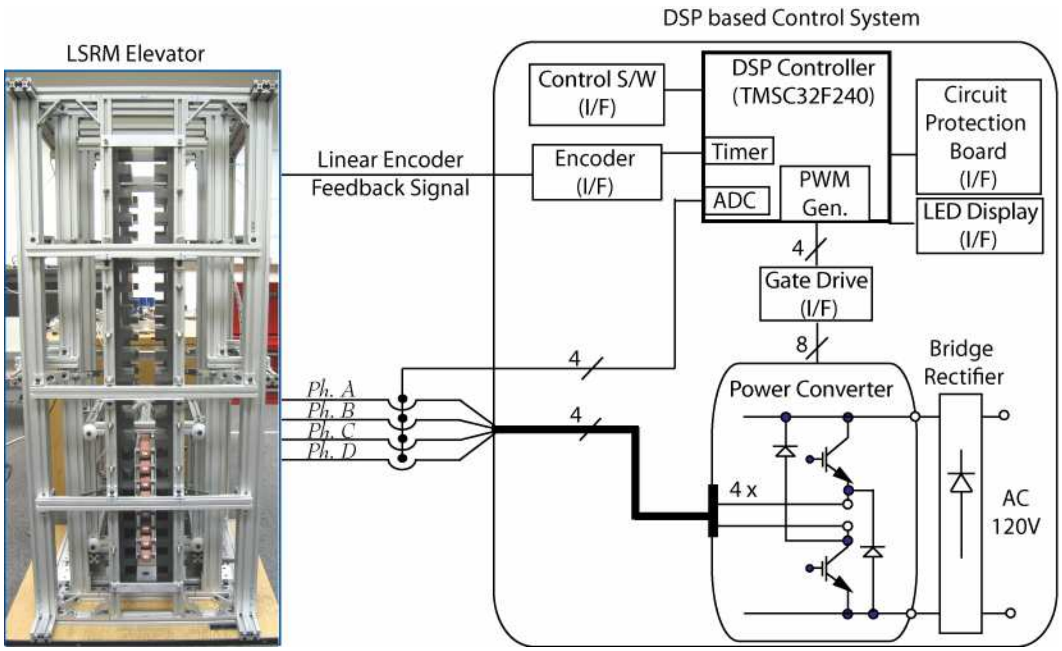

(a) Block diagram of the experimental setup

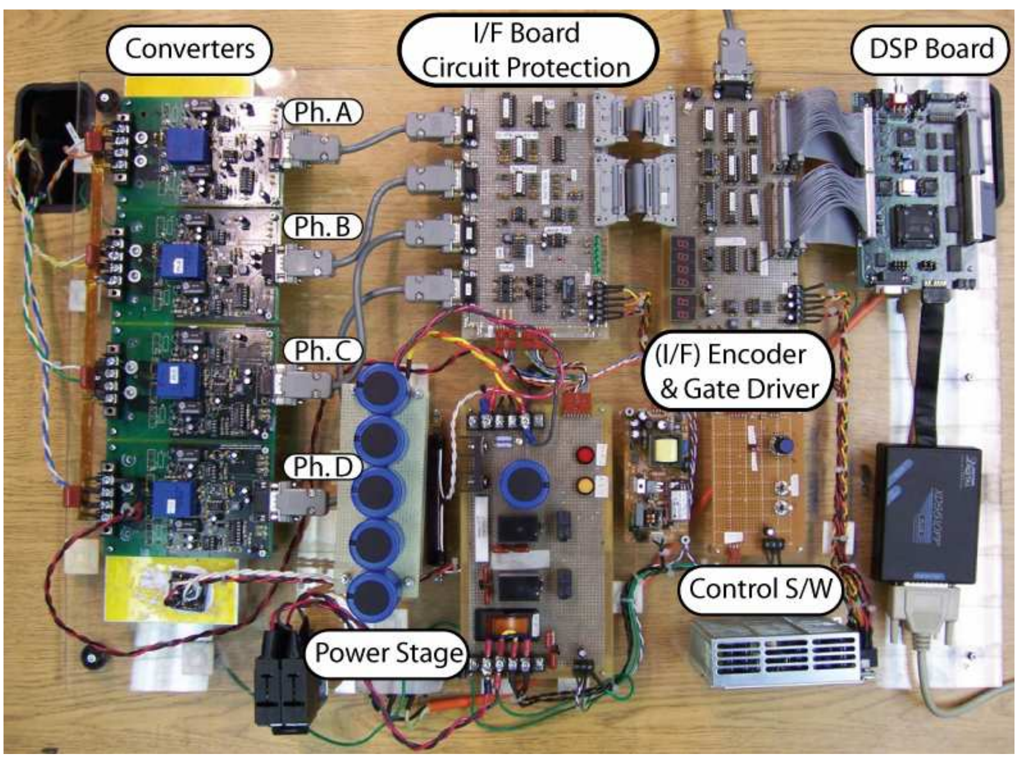

(b) Experimental setup of DSP based control system

Fig. 3.18 Experimental Setup

The actual experimental setup for the prototype elevator is shown in Fig. 3.18. The LSRM setup of the prototype elevator is described in Chapter 2 with figures of the structure and the designed LSRM. The controller is digitally implemented on a DSP-based control system and TI TMS320F240 DSP evaluation module running at 20MHz. Interface boards (I/F) are used to implement the control strategy discussed in earlier section. Asymmetric bridge converter is implemented for the experimental setup. Actual PWM signals for all converter boards are generated through an interface board after calculation of the duty ratio for PWM in the DSP in order to employ the unipolar PWM switching strategy presented in [22]. The carrier frequency of the PWM is 10KHz. A linear magnetic encoder sensor of 10um resolution runs alongside the stator, yielding position feedback signal to the DSP via the encoder interface board. Each phase current is measured by a current sensor (LEM LA-25NP transducer) and the current feedback is given to the DSP for current control. Experimental data are stored in the external memory of the DSP every 10ms and reconstructed from it. Thus, instantaneous velocity and position sampling data synchronized with each control loop time (1ms) can not be illustrated in following experimental results, except current data from an oscillator scope.

3.5.3 Experimental Results

The deceleration command is given at 0.624m (12-cycle distance, one cycle = 52mm) during ascent and at 0.104m (two-cycle distance) during descent while the dynamic simulation is at 0.6m and 0.1m, respectively. It stops at desired positions on top and bottom for one second just like the simulation. Velocity and payload applied to the prototype elevator are the same as the dynamic simulations. For comparison of the phase currents, a summarized table of results from the simulations and experimental tests is provided at the end of the experimental results.

Fig. 3.19 shows the experimental results at 0.15m/s with a payload of 23kg (11.5kg per LSRM) including the vehicle mass. The velocity profile and force control with the proposed FDF are exploited with current and velocity PI control. The measured velocity and position shown in Fig. 3.19(a) indicates that the controllers work successfully when the prototype elevator travels from 0.10m to 0.63m. The feedback of the velocity at 0.15m/s has some variation from the command due to the low speed which allows poor position information. In the case of the 10um linear sensor, when velocity loop is accessed every 1ms, it gives 75 counts to the DSP controller at 0.15m/s. Thus, higher velocity command yields a good velocity feedback as seen in the results at 0.2m/s and 0.3m/s. In Fig. 3.19(b), measured phase A and B currents are shown and their amplitudes vary according to the direction of motion due to the effect of gravity. During ascent the amplitude of 9.8A is required while during descent 9.0A is needed. In addition, the RMS value is 6.7A and 6.5A during ascent and descent, respectively. During halt on top and bottom, phase currents remain at a constant magnitude to hold the vehicle at the stop position because there is no mechanical brake system equipped to hold the elevator at the stop position as shown in Fig. 3.19 (b-iii).

Fig. 3.20 (a) shows the experimental results for position and velocity at 0.2m/s with a payload of 23kg including the vehicle mass. The feedback of the velocity shows less variation from the velocity command compared with the result at 0.15m/s. For phase current, Fig. 3.20 (b) shows phase A and B currents during ascent and descent as well as during transition for a few cycles of ascent and descent.

From Fig.3.21 and 3.22, payload is changed to 32kg and is experimentally tested at two different velocities, 0.2m/s and 0.3m/s. As expected, the results show increased current from the case with a lighter payload. At 0.2m/s the vehicle stops at 0.63m and 0.10m at top and bottom, respectively, while at 0.3m/s the stop position difference from the one at 0.2m/s is 10mm at top and 15mm at bottom. The amplitudes and RMS values of all measured and simulated phase currents are summarized in Table 3.8.

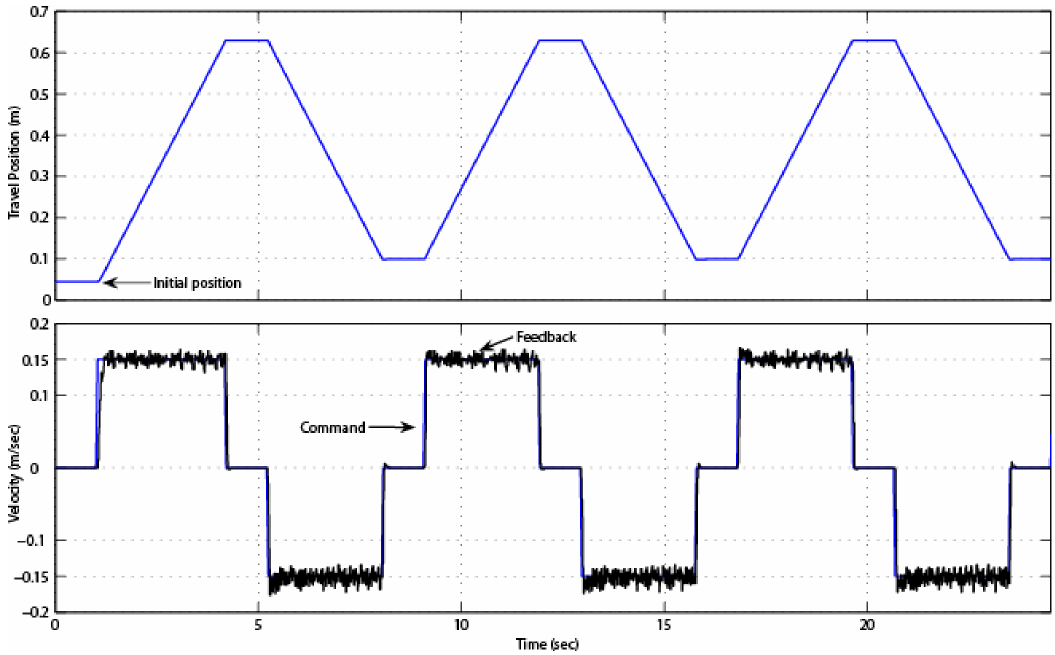

(a) position and velocity control

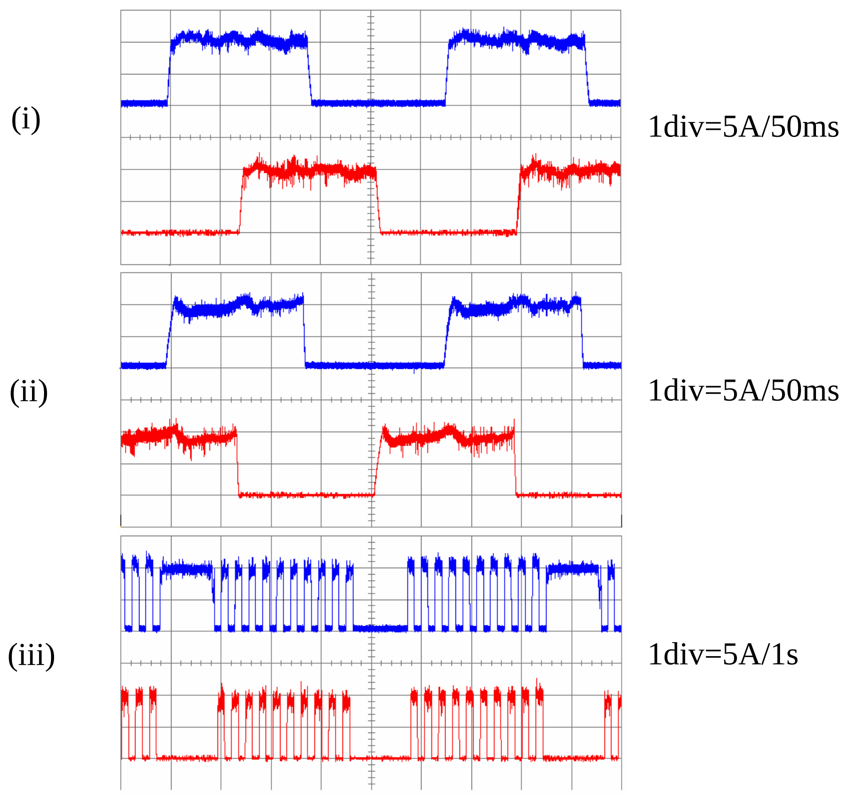

(b) Force and current control:

(i) Phase current in ascent, (ii) in ascent and (iii) during transition of direction

Fig. 3.19 Experimental results with a payload of 23kg (11.5kg *per LSRM*) at 0.15m/s

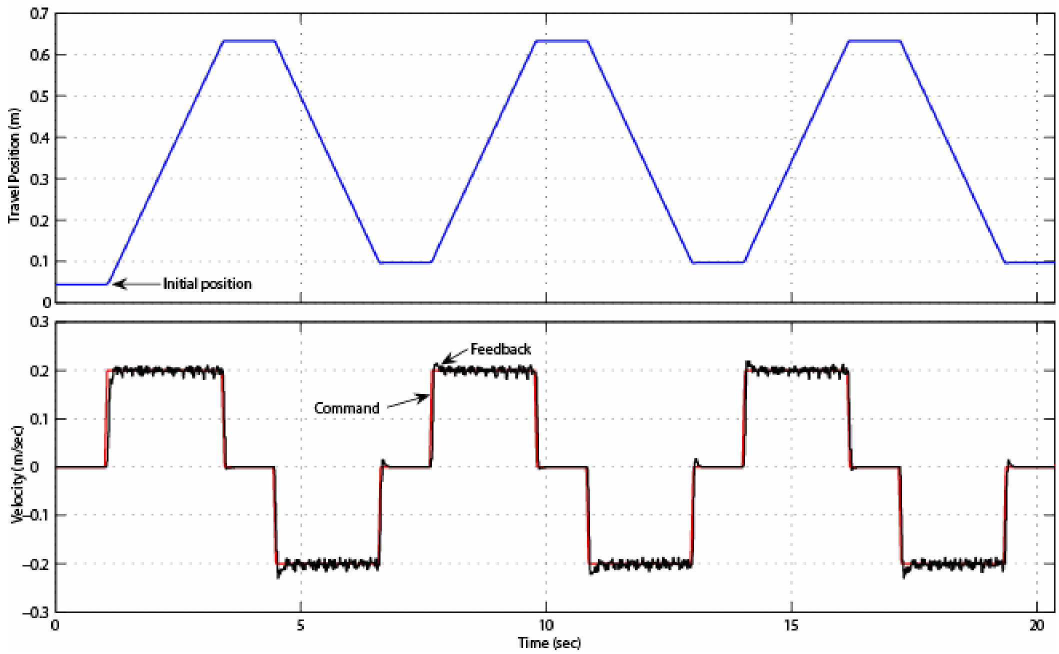

(b) position and velocity control

(i) 1div=5A/50ms

(ii) 1div=5A/50ms

(iii) 1div=5A/1s

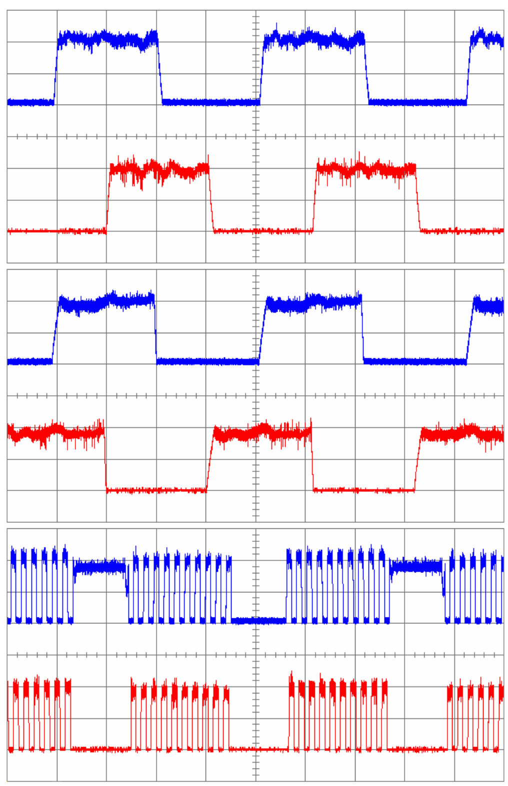

(b) Force and current control:

(i) Phase current in ascent, (ii) in ascent and (iii) during transition of direction

Fig. 3.20 Experimental results with a payload of 23kg (11.5kg *per LSRM*) at 0.2m/s

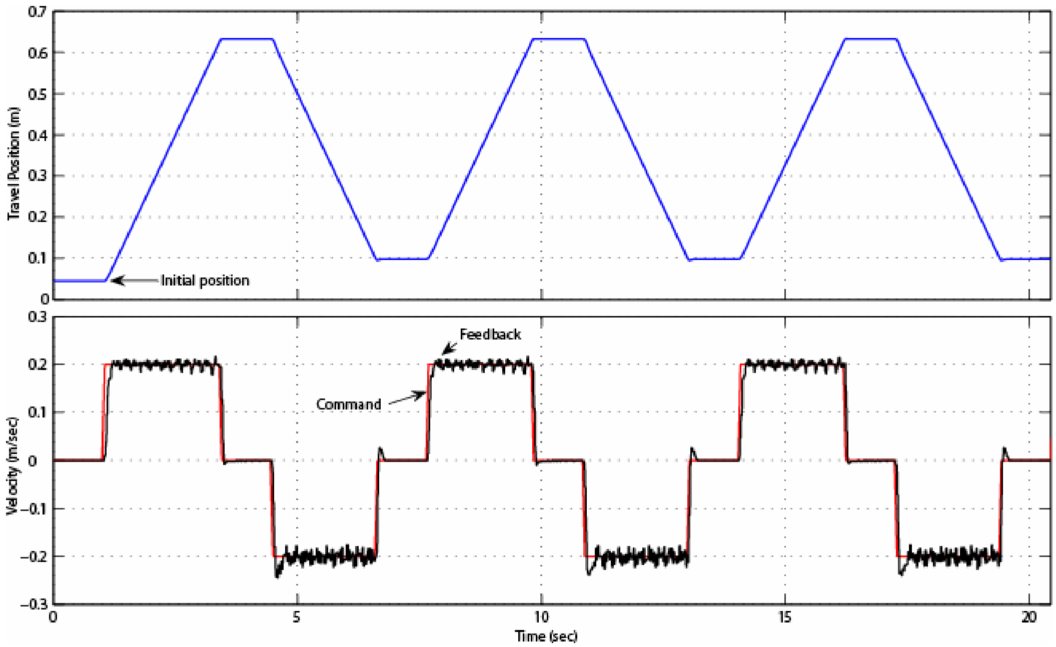

(c) position and velocity control

(i)

1div=5A/50ms

(ii)

1div=5A/50ms

(iii)

1div=5A/1s

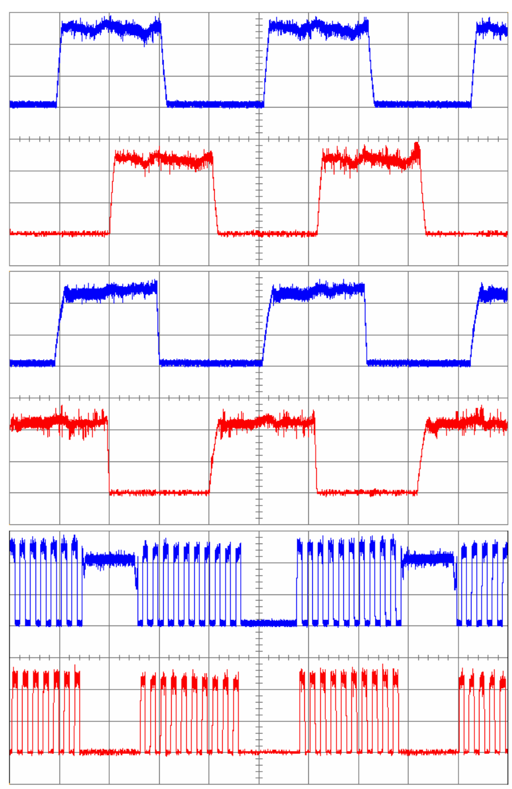

(b) Force and current control:

(i) Phase current in ascent, (ii) in ascent and (iii) during transition of direction

Fig. 3.21 Experimental results with a payload of 32kg (16kg *per LSRM*) at 0.2m/s

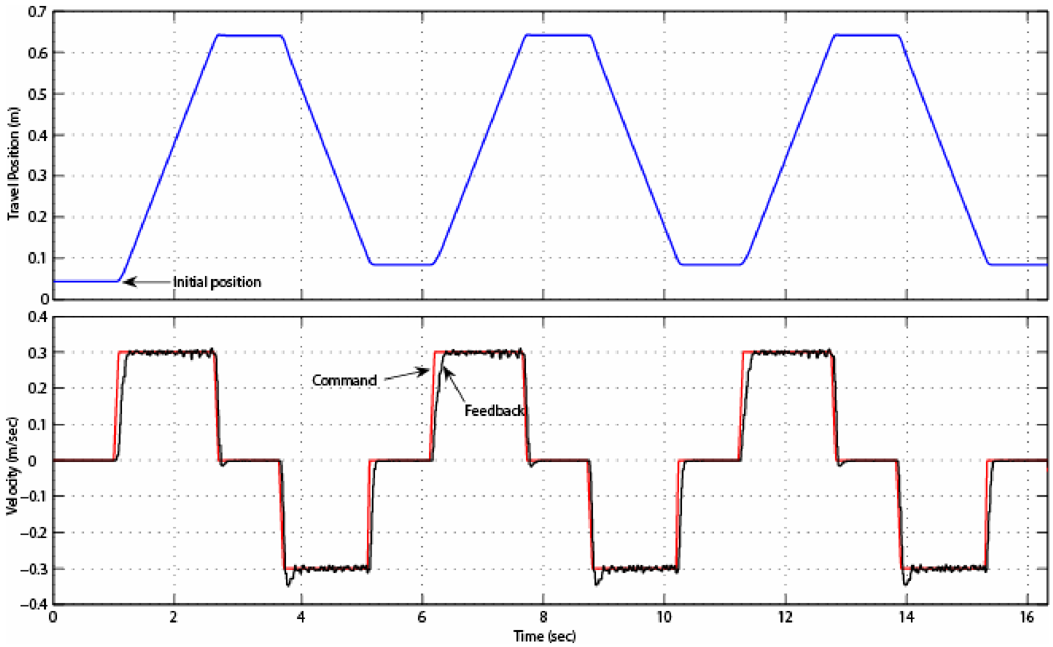

(d) position and velocity control

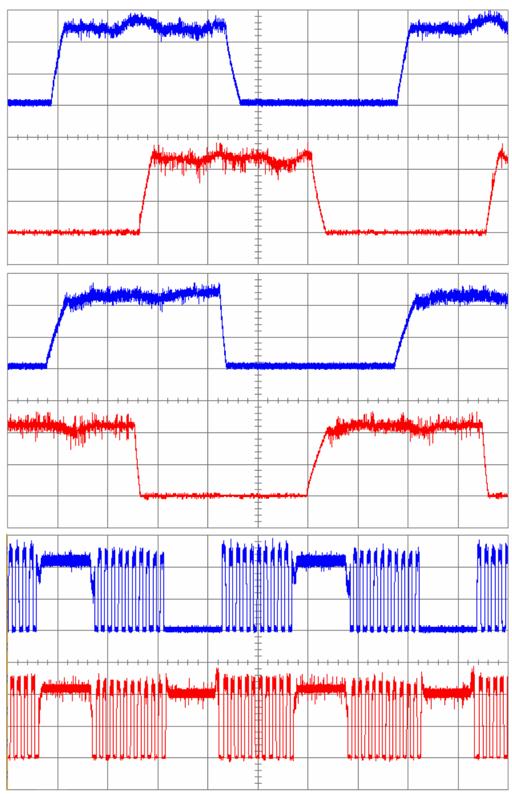

(i) 1div=5A/20ms

(ii) 1div=5A/20ms

(iii) 1div=5A/1s

(b) Force and current control:

(i) Phase current in ascent, (ii) in ascent and (iii) during transition of direction

Fig. 3.22 Experimental results with a payload of 32kg (16kg *per LSRM*) at 0.3m/s

Table 3.8 Comparison of the dynamic simulations and the experimental results.

Amplitude of phase A current, unit : A					
Velocity		**0.15m/s**		**0.2m/s**	
Period		ascent	descent	ascent	descent
Experimental results	**23kg**	9.8	9.0	9.8	9.0
Simulation Results	**23kg**	9.1	8.9	9.2	8.8
Velocity		**0.2m/s**		**0.3m/s**	
Period		ascent	descent	ascent	descent
Experimental results	**32kg**	11.7	10.9	11.7	10.9
Simulation results	**32kg**	10.7	10.5	10.8	10.4
RMS of phase A current, unit: A					
Velocity		**0.15m/s**		**0.2m/s**	
Period		ascent	descent	ascent	descent
Experimental results	**23kg**	6.7	6.5	6.3	6.8
Simulation Results	**23kg**	6.5	6.3	6.5	6.3
Velocity		**0.2m/s**		**0.3m/s**	
Period		ascent	descent	ascent	descent
Experimental results	**32kg**	7.5	8.3	7.4	8.3
Simulation results	**32kg**	7.6	7.3	7.7	7.3

3.5.4 Correlation between the Simulations and Experimental Results

Since experimental propulsion force data cannot be obtained during operation, the experimental force control performance can be measured by comparing phase currents between simulations and experiments. Table 3.8 shows the simulations and experimental tests with respect to the amplitude and RMS value of the phase current. With a payload of 23kg, the prototype elevator needs 9.8A during ascent and 9.0A during descent while the simulation results show that 9.1A and 8.9A, respectively. Thus, 0.7A in ascent and 0.1A in descent are the differences as shown in Table 3.8. In addition, the current results from the case of 23kg are well matched to the design point, 24kg at 10A. As the payload increases to 32kg, the phase current goes up to 11.7A during ascent and 10.9A during descent. In the experimental results, there is a 2A difference in the amplitude of current between 23kg and 32 kg while the simulation results show 1.6A difference. In RMS value, as seen in the table, the results of the experimental results and the dynamic simulation results shows only 0.2A difference, except the case of descent with 32kg which makes 1A difference. The differences between simulations and experiments are arising from the air gap variation due to manufacturing and assembly, and varying nonlinear parameters such as viscous constant with respect to positions. Air gap variation is between 1.2mm and 1.9mm at different positions when the phase current is not developed. In spite of these small discrepancies in the prototype, the experimental results closely mirror the simulation results, demonstrating the soundness of the proposed control strategy for the LSRM topology. Furthermore, the simulation, analysis and experimental verification indicate that the LSRM with the proposed control strategy in this research can be considered for vertical applications such as in elevators.

3.6 Conclusions

In this chapter, the prototype linear elevator using LSRMs has been experimentally validated with the proposed control strategy employed for the first time. The following contributions have been made in this chapter:

1) A dynamic voltage, current and force model of LSRM has been derived.
2) A superior force control technique with a proposed FDF method for a prototype elevator has been derived, analyzed, compared, implemented, and proved by way of the dynamic simulations and the experimental tests.
3) PI controllers for a current control loop and velocity control loop have been derived, analyzed, employed and validated via the dynamic simulations and the experimental tests. In addition, a trapezoidal velocity profile has been presented and applied to the prototype elevator to control position during moving as well as stop, and confirmed by extensive dynamic simulations and experiments.

4) The proposed LSRM technology for a ropeless prototype elevator has been experimentally demonstrated for the first time, and successfully verified at different velocities from 0.15m/s to 0.3m/s as well as with different payloads of 23kg and 32kg.
5) The correlation between dynamic simulation and experimental results has been established thus validating the proposed approach in the realization of the linear elevator, linear motor and system model and control strategies.
6) Converter topologies have been compared and asymmetric half-bridge converter topology has been chosen due to high control flexibility and fault tolerance and reliability. Asymmetric half-bridge converters have been implemented along with a unipolar switching strategy [5] for the test of the prototype LSRM elevator.
7) A DSP-based control system with TI TMS320F240 equipped has been realized to execute the proposed control strategy for the prototype LSRM elevator.

CHAPTER 4
NOVEL MEASUREMENT DISTURBANCE REJECTION CURRENT CONTROL

In previous chapter, effective control strategies are presented, especially concerning force control using a novel force distribution function (FDF). Force control is very important, especially in case of linear applications due to lack of any indirect coupling mechanism. If there is any force ripple, it directly affects the performance of the whole control system. As discussed and proved in the previous chapter, using the proposed FDF makes a remarkable difference in force control performance, especially during commutations between phases. As a result, velocity and position control can be successfully achieved. However, the force control is heavily dependent on the following loop, current control loop, which uses feedback currents through current sensors (transducers). In other words, corrupt feedback currents due to measurement errors with noise degrade current control performance and consequently force control performance. Up to present, however, conventional current controllers have not taken into account measurement disturbances mainly arising from noise and offset of current sensors, switching noise of PWM converters, DC-link voltage ripple, voltage drop of switching devices, variations in plant model parameters in SRMs as well as other motor drive systems. For a flux linkage control, a literature is presented by the author *et al.* [46] using a combination of voltage and current correction algorithm. Considering measurement disturbances on measured phase currents, a novel current control algorithm based on active disturbance rejection algorithm is proposed for the first time and verified by way of dynamic simulations and experiments in this chapter. For the novel current control, an extended state observer (ESO) is adopted to effectively estimate measurement disturbances on measured currents as well as to correct phase currents even in the presence of the measurement disturbances. Moreover, a nonlinear P controller (NLP) is proposed to control phase currents properly by compensating for disturbances. The proposed ESO and NLP are largely model-independent.

With previous literatures reviewed this chapter states measurement disturbance problem in motor drive systems, and describes a theoretical review of an ESO and NLP. In addition, conventional disturbance observers presented in many literatures are discussed with their advantages and disadvantages. Then, a novel current control technique based on the proposed ESO and NLP is presented. Dynamic simulations and experimental tests are performed and shown to validate the proposed current controller. In addition, FFT results on line and feedback phase currents are provided to support the excellence of the proposed current control method compared with a conventional PI controller at the end of this chapter.

4.1 Introduction

Current controller is very important because the propulsion force is generated directly by phase currents as given in (3.22). Current controller in LSRMs need correct feedback current signals to control each phase current properly reducing current ripple, and have been developed with various control techniques [47]-[50]. Bae *et al.* proposed a new switching scheme to reduce current and force ripple using a unipolar converter switching method with a decoupling of the induced emf [47] and also using a new dynamic FDF model with mutual inductance considered [48]. Lin *et al.* [49] proposed a high performance current control method using on-line parameter estimation, and consequently adjust the current control gain according to the estimated inductance value. Wei *et al.* [49] introduced another current control method called PSCC 90-degree phase-shift current control to reduce current ripple. It is similar to Bae *et al.* [47] in the sense of increasing a chopping frequency by double without increasing a physical converter switching frequency. The difference is that Wei *et al.* directly changed a DSP register value according to operation modes to make the switching strategy possible while Bae *et al.* [47] made a virtual opposite sign of voltage command to an actual voltage command from a current error and enabled the switching frequency to be effectively doubled. In these current control schemes, however, an ideal measurement of a current feedback signal is assumed and more importantly all of them did not consider the effect of measurement disturbances, mainly arising from noise and offset of a current sensor, switching noise at a fixed switching frequency of a PWM converter, and voltage drop of a switching device. Corrupted currents by measurement disturbances cause a current controller to generate a fluctuating current command due to a noisy feedback current and result in producing undesirable force ripple as presented by Lim *et al.* [46]. Therefore, unknown and uncertain measurement disturbances contained in feedback phase currents need to be compensated so that LSRM actuation systems are more reliable and acceptable for vertical as well as horizontal propulsion applications. Moreover, noisy currents increase acoustic noise which is one of main drawbacks of (L)SRMs. Therefore, the effect of measurement disturbances on phase currents is analyzed, and an effective phase current measurement disturbance rejection algorithm using an extended state observer (ESO) is proposed in this chapter.

Furthermore, some current controllers use a variable control gain in a proportional plus integral (PI) controller to achieve high performance SRM drives [48][50]. Variable control gains in SRMs need accurate nonlinear machine parameters, such as inductance with respect to position and current. If stored or estimated machine parameters are not correct, the controller cannot work properly and sometimes can cause high peak currents. As a result, the control system and SRMs can be damaged. In case of elevator applications, this problem should be prevented. Therefore, a largely model-independent NLP is proposed in this chapter as one part of the novel current control algorithm in order to achieve reliable and robust current control system.

Due to superior and robust current control performance, it is believed that the proposed method can be successfully applied into other motor drive systems in the presence of measurement disturbances.

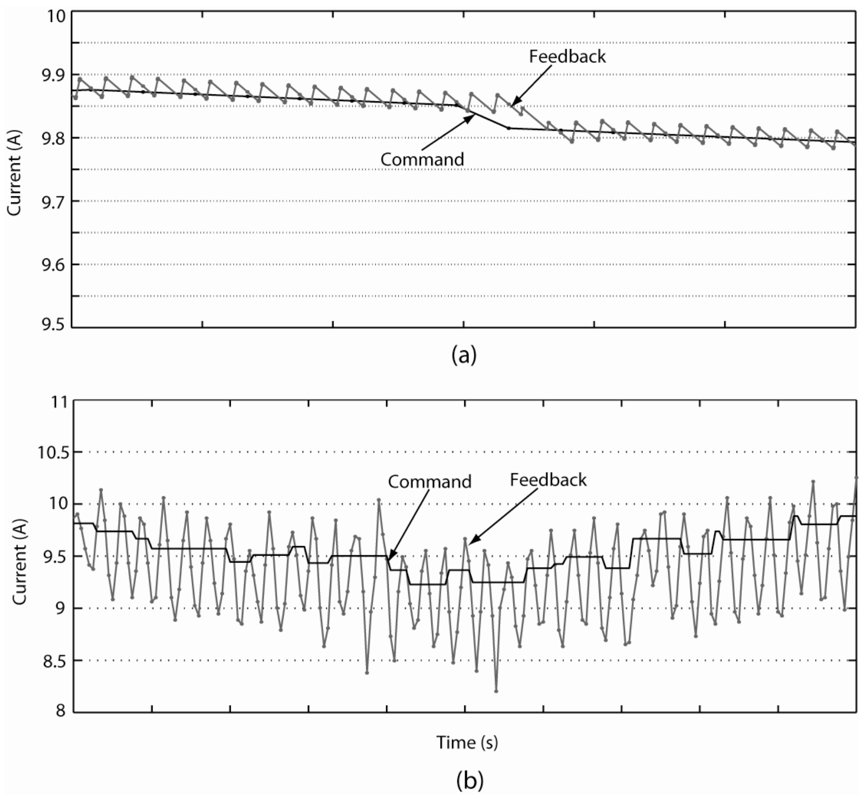

Fig. 4.1 Phase current sampled at every 100us:

(a) Simulated phase current and (b) Measured phase current.

4.2 Problem Statement

In motor drive systems, PWM converter switching is the main source of electromagnetic interference (EMI) emission [85][86]. In addition, measurement instruments such as a current sensor have their own sensor errors [87] and are very susceptible to EMI. Measurement disturbances cause feedback signals such as a phase current to become noisy and distorted as shown in Fig. 4.1. Corrupted current feedback increases torque or force ripple and generates increased acoustic noise. Thus, measurement disturbance should be prevented to enhance control performance, reduce acoustic noise and mitigate the effect of EMI on other electronic components. EMI issues of PWM-based motor drive systems have been studied in [85] and [88], and many hardware-based approaches have been explored to suppress the effect of EMI emission such as active filters [89]-[90] and multilayer PCB techniques [91]. For compensation of sensor noise and offset error, a sensor model-based error correction method was presented by Shestakov

[87]. However, dealing with measurement disturbances contained in sensed currents largely has not been explored with software algorithms. In particular, there are only a few papers focusing on the issue of measurement errors [87] [92]. Massicotte *et al.* [92] used a Kalman-filter method to correct a measured signal for spectrophotometric data. The algorithm has three assumptions and requires four numerical calculation steps to find the correction of the estimates. In addition, it needs a-priori knowledge of data to be corrected. These limitations preclude the use the Kalman-filter approach in practice.

In this chapter, a simple, effective and largely model-independent current control algorithm is presented to reject the measurement disturbances in motor drive systems. It is based on an ESO and NLP and proves to enhance current and force control performance through dynamic simulations and experiments. Furthermore, acoustic noise and EMI are expected to decrease because of ripple reduction in force and current. FFT analyses on measured currents captured via an oscilloscope are presented as one of evidences of reduction of force and current ripple as well.

4.3 Disturbance Observers

In almost all control system, the presence of disturbances, model uncertainties and nonlinear model parameters is inevitable. In general, disturbances are defined as external load, velocity, and position disturbances, and internal parameter variations. Model uncertainties and nonlinear parameters are concerned with developing a mathematical model of control systems. Assuming a system is well modeled in a mathematical form, control system needs to be robust against any disturbances. Recently, disturbance observers have been presented [56]-[62] to estimate disturbances and enhance robustness as well as performance of control by rejecting the estimated disturbances. The disturbance for disturbance observers is redefined as the sum of the external disturbance signals and all possible signals due to the difference between the actual plant and the nominal model such as parameter variations and modeling uncertainties. However, as the most important control loop, a current controller equipped with a disturbance observer to reject disturbances has rarely been explored in (L)SRM and other motor drives. As mentioned earlier, measurement disturbances are mainly arising from noise and offset of current sensors, switching noise of PWM converters, DC-link voltage ripple, voltage drop of switching devices, variations in plant model parameters. Since a contaminated current feedback signal affects the whole control performance causing current and force ripples from the command as shown in [46], the need of a robust current control algorithm against measurement disturbances has been raised. In this regard, conventional disturbance observers have been developed, presented in many literatures, and reviewed in the following section.

4.3.1 Conventional Disturbance Observer

Nonlinear disturbance observers have been presented in [56] and [57]. As one of the popular nonlinear observers, a variable structure system (VSS) sliding mode observer (SMO) is presented by Xinkai, *et al.* [56]. It is robust against disturbances, but requires an upper and lower boundary of disturbances and also has limits on measurement noises and the order of the systems. In addition, SMO has a chattering problem due to the nonlinear characteristics of sliding mode method. As another nonlinear alternative to SMO, a binary disturbance observer (BDO) is presented by Han *et al.* [57]. BDO shows a good performance against disturbances suppressing the chattering problem, but it has likewise a convergence problem due to dependence on the initial states of the control system. Error boundaries for SMO and BDO need to be chosen carefully to make control systems stable and fast enough to perform properly. Reference [58] and [59] apply adaptive disturbance observers to estimate disturbances and achieve a robust control system. Implementation of the disturbance observer based on adaptive control algorithm has some drawbacks, such as slow response and lack of robustness due to heavy calculations and the uncertainties of the control system, especially in case of rapid change of parameters during transient periods. In [60] through [62], disturbance observers based on the transfer function of plant models are explored to estimate disturbances, but they have stability problems. The preceding disturbance observers are highly dependent on an accurate mathematical representation of the plant, but there are always limitations in modeling plants without the uncertainties and complicated nonlinear terms which cause problems in robust control. Therefore, a nonlinear model-independent extended state observer (ESO) has been introduced and is explained in the next section.

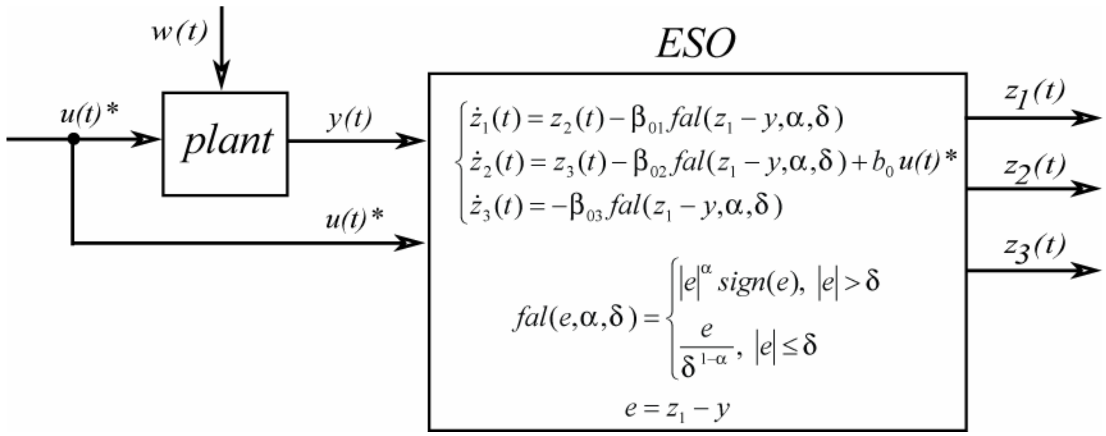

(a) 3rd order extended state observer (ESO)

Fig. 4.2 Block diagram of a general extended state observer (ESO).

4.3.2 Extended State Observer (ESO)

The idea of the extended state observer (ESO) is to estimate the system's unmodeled dynamics and external disturbances as an additional or extended state. An ESO was first proposed by Han [63] as a unique observer based on a nonlinear continuous structure of an output error. Since the first presentation, ESO-based control methods have been tested and verified in many applications [64]-[78]: Noise cancellation [64], motion control [66], [68], [71]-[74], [76]-[78], truck anti-lock brake system (ABS) [69], wind energy conversion system [70], DC-DC converter [75]. Motion control applications with ESO include a robotic system [68], an induction motor [71], a permanent magnet linear motor [72]-[73], [78], and a planar switched reluctance motor [74], an AC servo system [76]-[77]. In those applications, a nonlinear feedback controller is employed with ESO to compensate disturbances estimated by ESO. A nonlinear controller will be discussed in detail in the following section. A general ESO with a feedback controller proposed by Han [63] and [79] is shown in Fig. 4.2.

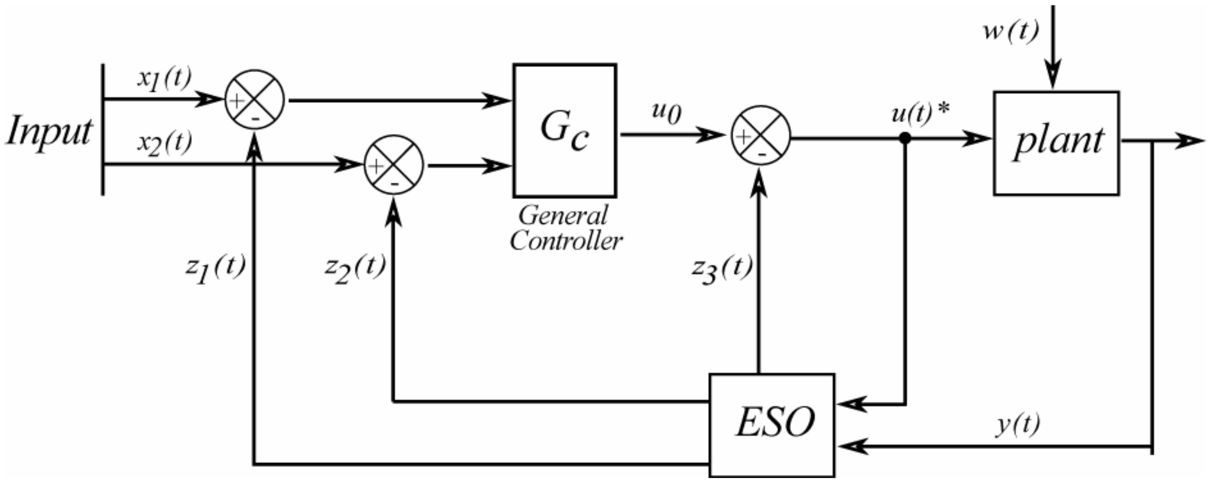

(b) 3rd order extended state observer (ESO) with a feedback controller

Fig. 4.2 Block diagram of a general extended state observer (ESO) (continued).

A class of nonlinear SISO system is described as follows with an extended state:

$$\begin{cases} \dot{x}_1 = x_{2,} \\ \dot{x}_2 = x_3 + bu(t),\ \ x_3 = a(t) \equiv f(x_1, x_2, w(t)) \\ \dot{x}_3 = h(t),\ \ h(t) = \dot{a}(t) \\ y = x_1 \end{cases} \tag{4.1}$$

where *y*, *u* and *x* are the output, input, and state variables, respectively; $f(\bullet)$ is the plant uncertainties including external disturbances *w(t)*; x_3 is the extended state of *h(t)*, which is the derivative of the $f(\bullet)$. Here both $f(\bullet)$ and *h(t)* are assumed to be unknown. Conventional state observers mentioned in previous section depend on the knowledge of plant dynamics, $f(\bullet)$. However, by making $f(\bullet)$ a state, it is now possible to estimate $f(\bullet)$ even though $f(\bullet)$ contains unknown parameters and uncertainties along with disturbances. This is the basic idea of using ESO, making it unique compared with conventional disturbance observers. Now, an ESO for the plant of (4.1) is formulated as

$$\begin{cases} \dot{z}_1(t) = z_2(t) - \beta_{01}\,fal(z_1 - y, \alpha, \delta) \\ \dot{z}_2(t) = z_3(t) - \beta_{02}\,fal(z_1 - y, \alpha, \delta) + bu(t) \\ \dot{z}_3(t) = -\beta_{03}\,fal(z_1 - y, \alpha, \delta) \end{cases} \tag{4.2}$$

$$fal(e, \alpha, \delta) = \begin{cases} |e|^{\alpha} sign(e), & |e| > \delta \\ \dfrac{e}{\delta^{1-\alpha}}, & |e| \le \delta \end{cases} \tag{4.3}$$

$$e = z_1 - y$$

$$\begin{aligned} fal_2(e, \alpha, \delta) &= g(e, \alpha, \delta) \\ &= \begin{cases} k_2 e + sign(e)(k_1 - k_2)\delta, & |e| > \delta \\ k_1 e, & |e| \le \delta, \delta > 0 \end{cases} \end{aligned} \tag{4.4}$$

$$e = z_1 - y, k_1 = \delta(\alpha - 1)$$

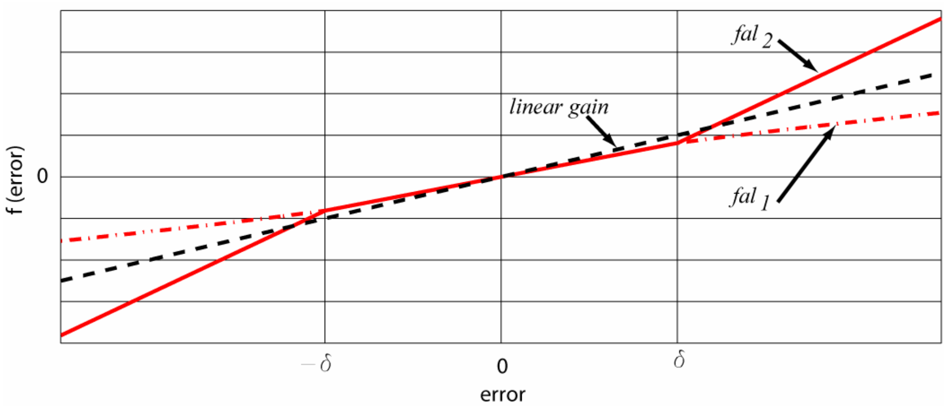

Fig. 4.3 Comparison of linear and nonlinear gains.

where z_1 and z_2 are the estimated state of x_1 and x_2, respectively; z_3 is the estimate of the extended state x_3 and represents the overall uncertainties of the plant and external disturbances; β_{0i}, k_i, α, and δ are tunable constants of the observer ESO; b is assumed to be given as a constant plant parameter; and the nonlinear function $fal_i(\bullet)$ consists of error between the estimate z_1 and the output y, with two constants, α and δ. Interestingly, if the nonlinear function fal_i is of the form $k_e e$, the ESO takes the form of a classical Luenberger observer. On the other hand, if a function of the form $\beta_{0k}(e+k_e sign(e))$ is used instead of the $fal_i(\bullet)$, then it is considered a variable structure observer [79]. In Fig. 4.3, fal_2 shows better transient performance avoiding significant transient error for a plant with unknown initial conditions [67] and is used for this research. The ESO can be expanded to an (n+1)th-order system according to the plant.

4.3.3 Proposed Extended State Observer (ESO)

The proposed current control algorithm takes advantages of ESO in order to develop a general method to address unknown measurement disturbances irrespective of the LSRM model and specific tasks to be fulfilled.

A. Extended State Equation of an LSRM with a Disturbance State

The proposed ESO is derived from the simplified LSRM dynamic voltage equation as below.

$$\begin{aligned} v(t) &= Ri(t) + \frac{d\lambda(x,i)}{dt} \\ &= Ri(t) + L(x,i)\frac{di(t)}{dt} + i(t)\frac{dL(x,i)}{dt} \\ &= (R_m + \Delta R)i(t) + (L_m + \Delta L(x,i))\frac{di(t)}{dt} + i(t)\frac{d(L_m + \Delta L(x,i))}{dt} \\ &= \left[\left(R_m + \Delta R + \frac{d(\Delta L(x,i))}{dt}\right)i(t) + \Delta L(x,i)\frac{di(t)}{dt}\right] + L_m\frac{di(t)}{dt} \\ &= [w(t)] + L_m\dot{i}(t) \end{aligned} \tag{4.5}$$

where $v(t)$ = phase voltage, R = phase resistance, $i(t)$= phase current, x = position, $\lambda(x,i)$ = flux linkage, $L(x,i)$ = phase inductance, $R_m =$ constant phase resistance, $\Delta R =$ unknown variable phase resistance, $L_m =$ average phase inductance, $\Delta L(x,i) =$ unknown variable phase inductance, $w(t)$= unknown measurement disturbance term.

The system in (4.5) can be written in the form of an extended state equation with the disturbance $w(t)$ comprising an extended state:

$$\dot{i}(t) = \frac{1}{L_m}\overline{w}(t) + \frac{1}{L_m}v(t) \quad \leftrightarrow \quad \begin{cases} \dot{x}_1(t) = x_2(t) + bu(t) \\ \dot{x}_2(t) = h(t), h(t) = \dot{a}(t) \\ y(t) = x_1(t) \end{cases} \tag{4.6}$$

where $x_1(t)=i(t)$, $x_2(t)=a(t)=b\,\overline{w}(t)$, $h(t)=b\,\dot{\overline{w}}(t)$, $\overline{w}(t)=-w(t)$, $u(t)=v(t)$, and $b=1/Lm$.

B. Proposed Extended State Observer (ESO)

From (4.6) the proposed ESO is given as

$$\begin{aligned} \dot{z}_1(t) &= z_2(t) + bu(t) - \beta_{01} g(e, \alpha_o, \delta_o) \\ \dot{z}_2(t) &= -\beta_{02} g(e, \alpha_o, \delta_o) \end{aligned} \tag{4.7}$$

$$\begin{gathered} g(e, \alpha_o, \delta_o) = \begin{cases} k_{o2} e + sign(e)(k_{o1} - k_{o2})\delta_o, & |e| > \delta_o \\ k_{o1} e, & |e| \le \delta_o, \delta_o > 0 \end{cases} \\ e = z_1 - y, k_{o1} = \delta_0(\alpha_o - 1) \end{gathered} \tag{4.8}$$

where z_i is the estimate of the state x_i and β_{0i}, k_{oi}, α_o, and δ_o are tunable constants in the ESO. The extended state z_2 estimates measurement disturbances arising from sensor noise, measurement error and parameter variations.

The proposed ESO takes a very simple form compared with other conventional nonlinear observers. Furthermore, it can effectively estimate the states without heavy calculations and estimation errors because it is a largely model-independent observer. Since z_2 estimates measurement disturbances containing unknown parameter variations, the estimation performance of the ESO is robust against parameter variations such as changes in phase inductance and resistance during operation. This is an attractive benefit of using the ESO; conventional observers are very sensitive to the parameter variations. Once the extended state of the measurement disturbance is successfully estimated, errors in measured currents due to the disturbance are compensated for by a simple and effective nonlinear P controller (NLP) discussed in the following section.

4.4 Nonlinear Controller

As a challenging control trend, nonlinear controllers have been emerging and established since 1980. Some reasons for the interests in nonlinear control methodologies can be listed below [80]:

(1) Linear controllers depend on the key assumption of local range operation for the linear model to be valid. Thus, a linear controller is likely to function properly or to be unstable, because the nonlinearities in the system cannot be properly compensated for. On the other hand, nonlinear control methods may directly deal with the nonlinearities in large range operation.

(2) Linear control methods assume that the system model is indeed realizable. However, in control systems there are many nonlinearities that cannot be allowed to be linearized such as Coulomb friction, saturation, dead-zones, backlash, and hysteresis. These nonlinearities render undesirable behavior of the control systems, such as instabilities or spurious limit cycles and hence their effects must be considered and properly compensated for.

(3) Assuming that the parameters of the system model are reasonably well known is usually necessary in designing linear controllers. In reality, however, many control problems involve uncertainties in the mathematical representation of the plant. As a result of the uncertainties in the system, linear controllers based on inaccurate or obsolete values of the model parameters may yield significant performance degradation or even instability. In this regard, nonlinear controllers intentionally include the uncertainties into the controller part so that model uncertainties can be compensated.

(4) Design of nonlinear controllers is based on the physics of the plant and hence nonlinear control methods are more intuitive and simple than linear counterparts.

(5) Nonlinear controllers can achieve an acceptable control performance with less expensive components with nonlinear characteristics while linear controllers need high quality actuators and sensors to yield linear behavior in the specified operation range. Thus, nonlinear control methods are more cost effective than linear controllers.

With these advantages over linear controllers, several nonlinear control methodologies have been introduced, such as back stepping, feedback linearization, sliding mode, Lyapunov method and adaptive control [80]-[82]. However, most of all nonlinear controllers are deeply rooted in accurate system model representations. Theses control theories based on an accurate model of system have fundamental limitations, mostly robust issues in the presence of model uncertainties and external and internal disturbances. Model-based control theory is called “model theory” by Han [63] and a model-free nonlinear control is proposed in [65]. The model-free nonlinear control method comes with an extended state observer (ESO) which is mentioned in previous section.

From (4.1), a motion control system can be described as,

$$\begin{cases} \dot{x}_1 = x_{2,} \\ \dot{x}_2 = a(t) + u(t),\ a(t) \equiv f(x_1, x_2, w(t)) \\ y = x_1 \end{cases} \tag{4.9}$$

Where x_1 and x_2 and *a(t)* are position, velocity and “inherent acceleration”, respectively, and *u(t)* is the control input. In many applications, *a(t)* can be regarded as a nonlinear function of many variables as shown in (4.8). In this case, *a(t)* consists of position and velocity, and internal and external disturbances, *w(t)*. The system representation shown in (4.9) is very simple and intuitive like design of a linear control system, but is not dependent on accurate model behaviors of the system which need in designing linear controllers and conventional nonlinear controllers. Since classical PID control methods have been chosen as the most common controller in over 90% of industrial applications [83], Han proposed a nonlinear feedback controller suitable for a model-free control system: a generic nonlinear proportional-integral-derivative (PID) control scheme [65]. A classical PID controller has three parts: current (P), past (I), and future (D) of error, and is shown below.

$$u(t) = K_P e(t) + K_I \int_0^t e(t)dt + K_D \frac{de(t)}{dt} \tag{4.10}$$

Here the error is defined as the difference of the desired output and the measured output, $y_d(t)$-$y(t)$. K_P, K_I and K_D are PID controller gains that can be obtained or tuned intuitively. For the nonlinear PID controller, Han proposed a new control law in a nonlinear form given as

$$u(t) = K_P |e|^{\alpha_P} sign(e) + K_I |e|^{\alpha_I} sign\left(\int_0^t e dt\right) + K_D |e|^{\alpha_D} sign\left(\frac{de}{dt}\right) \tag{4.11}$$

The nonlinear terms in (4.11) produce better performance compared to the linear one in (4.9). When $0<\alpha<1$, the nonlinear part provide higher gain when the error is small and lower gain when error is large. In addition, as $\alpha \rightarrow 0$, this bound of the error will be zero which is the case of the well-known variable structure control (or sliding mode control). In this sense, the nonlinear PID controller is very intuitive, simple and practical method, and embraces the benefits of the nonlinear controllers, such as sliding mode, fuzzy logic and gain scheduling controllers, but does not have complicate implementation problems. In addition to the benefits of simple PID controllers, a nonlinear function was proposed to enhance the nonlinear mechanism instead of the nonlinear term, $|e|^{\alpha} sign(e)$, and is given as,

$$fal(e,\alpha,\delta) = \begin{cases} |e|^{\alpha} sign(e), & |e| > \delta \\ \dfrac{e}{\delta^{1-\alpha}}, & |e| \le \delta \end{cases} \tag{4.12}$$

The above nonlinear function can be replaced with other nonlinear functions suitable for control systems. The reason of using nonlinear functions according to the size of the error is to prevent chattering problems due to high gain when the error is small.

4.4.1 Proposed Nonlinear P Controller (NLP)

Based on nonlinear PID controllers discussed in the previous section, a new nonlinear P (NLP) controller is proposed to compensate for measurement disturbance estimated by the proposed ESO.

A. Proposed Nonlinear P controller (NLP)

A new nonlinear P controller (NLP) based on the classical PID controller with nonlinear function, shown in (4.4), is proposed to compensate for measurement disturbances estimated by the proposed ESO. The plant of (4.2) can be simplified with the control input $u(t)$ given as

$$u(t) = \left(u_0(t) - z_2(t)\right)/b \tag{4.13}$$

where $u_0(t)$ is a new control input which is generated by the NLP. Assuming that the proposed ESO shown in (4.7) successfully estimates the measurement disturbance state $x_2(t)$, then $x_2(t) = z_2(t)$. Using (4.13) as the control input $u(t)$, the original plant is simplified to a single integrator control problem of

$$\begin{aligned} \dot{x}_1(t) &= u_0(t) \\ y(t) &= x_1(t) \end{aligned} \tag{4.14}$$

As a result, an integral part in the controller is not required and the proposed NLP produces the new control input $u_0(t)$ as

$$\begin{aligned} u_0 &= K_{pc} \cdot e \\ &= \left[k_{pc}\, fal(e, \alpha_{pc}, \delta_{pc})\right] \end{aligned} \tag{4.15}$$

where,

$$\begin{gathered} g(e, \alpha_{pc}, \delta_{pc}) = \begin{cases} k_{pc2}e + sign(e)(k_{pc1} - k_{pc2})\delta_{pc}, & |e| > \delta_{pc} \\ k_{pc1}e, & |e| \le \delta_{pc}, \delta_{pc} > 0 \end{cases} \\ e = x_1 - z_1, k_{pc1} = \delta_{pc}(\alpha_{pc} - 1) \end{gathered} \tag{4.16}$$

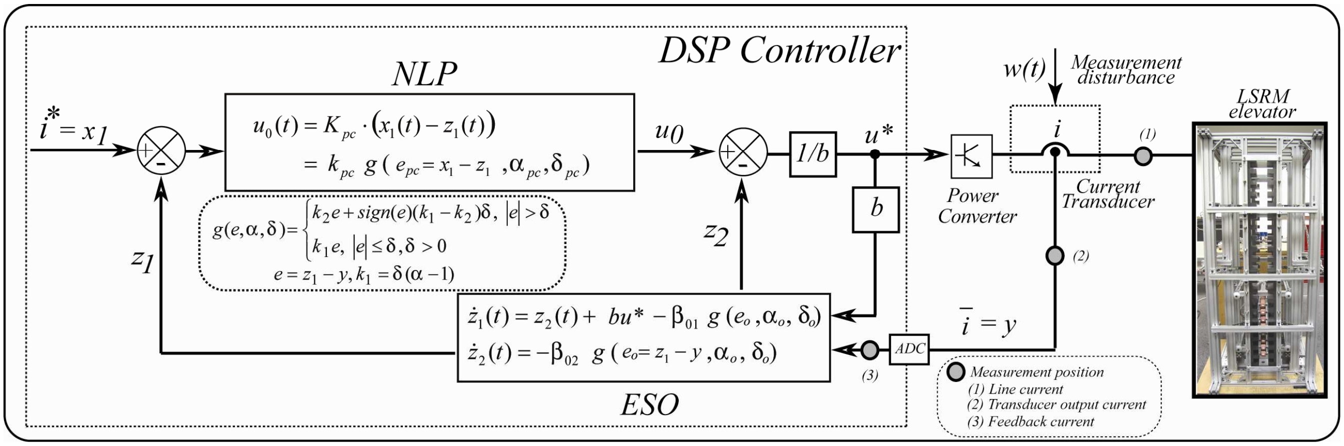

Fig. 4.4 Block diagram of the proposed current control based on the ESO (4.7) and NLP (4.15).

4.5 Proposed Current Control based on the ESO and NLP

With the ESO in (4.7) and the NLP in (4.15), the proposed current control is now complete and the control block diagram is shown in Fig. 4.4. This control scheme is called active disturbance rejection control (ADRC) proposed by Han [63]. The general ADRC configuration has three parts [63]: a profile generator, an ESO and a nonlinear PID controller. The profile generator is used to generate position and velocity trajectories. Based on the ADRC configuration, many motion control applications have been presented [66], [68], [71]-[74], [76]-[78]. For this research, the proposed current control scheme takes advantages of the ADRC to deal with unknown measurement disturbances mainly caused by sensor noise and offset, PWM switching noise of PWM converter, and plant parameter variations. As shown in Fig. 4.4, only each phase current is used as the input state and the other state is an extended state representing total measurement disturbances. The total measurement disturbances are actively detected by the proposed ESO and compensated for by the proposed NLP. Therefore, this current control method can be successfully used to achieve high performance current control in the presence of measurement disturbances. In particularly, DSP-based motor drive control systems generate switching noises of PWM converters which degrade current feedback signals. In this sense, the proposed current control strategy based on the ESO and NLP shown in Fig. 4.4 is expected to become one of the most effective and robust current control methods in motor drive control systems. In next section, the proposed current controller is validated through extensive dynamic simulations and experiments.

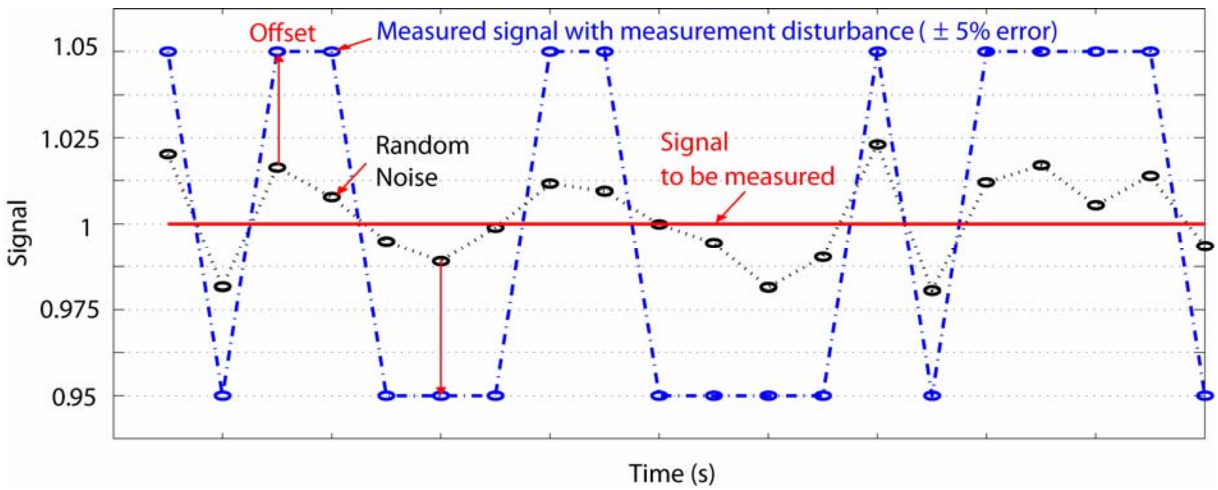

Fig. 4.5 Measurement error signal generator with noise: 5% measurement error.

4.6 Dynamic Simulations

In this section, simulation results of the proposed ESO+NLP current controller and a conventional PI controller are shown and compared in terms of position, velocity, force and current control performance of the prototype LSRM elevator, which is simulated with a 23kg payload at speed of 0.2 m/s. The ESO and NLP parameters used in this simulation are summarized in Table I; the motor parameters and input specifications are summarized in the Appendix C. In particular, current control simulations are the main validation of the proposed current controller's robustness against measurement disturbance. Force control is performed using multi-phase excitation to minimize force ripple during commutation [1]. Position control of the elevator is achieved using the simple trapezoidal

Table 4.1

ESO and NLP parameters used in Simulations

k_{o1}	k_{o2}	α_o	δ_o	β_{o1}	β_{o2}	b_o
1.0353	12	0.95	0.5	1200	250	50
k_{pc1}	k_{pc2}	α_{pc}	δ_{pc}	b_{pc}	k_{pc}	
0.9718	1.5	0.7	1.1	50	285	

controller. Details of the control loops are presented in the previous chapter. Finally, phase current feedback is "corrupted" with a measurement disturbance generator, shown in Fig. 4.5, which adds an offset and random noise to the feedback signal. Based on Fig. 4.1(b), the error range of the disturbance generator is set to 5%

The simulation results reveal marked differences between the PI and the ESO+NLP current controller, as evidenced by the line and feedback current in Fig. 4.6. In Fig 4.6(a)-(d): the "Line current" trace indicates the actual phase current at measurement point (1) in Fig. 4.4 and the "Feedback" trace represents the corrupted current given to the current controller. Thus, feedback currents has more noise and consequently causes a degradation of the PI current controller output (that is, line currents their associated propulsion forces) performance as shown in Fig 4.6(a) and (c).

In contrast, the ESO+NLP controller effectively estimates and compensates for measurement disturbances, tracking the current command with the NLP. Fig. 4.6 (e) and (g) shows the estimate z_1 of the actual line current rejecting measurement disturbance, thereby recovering the true line current. The estimated measurement disturbance, z_2 , is shown in Fig. 4.6 (f). Fig. 4.6(h) shows that the ESO successfully estimates the actual line current. Thus the error between line current and estimate z_1 is much less than the error between line current and feedback current which contains measurement disturbance. As a result, the experimental implementation of the ESO+NLP current controller should reject measurement disturbances and demonstrate superior current control performance

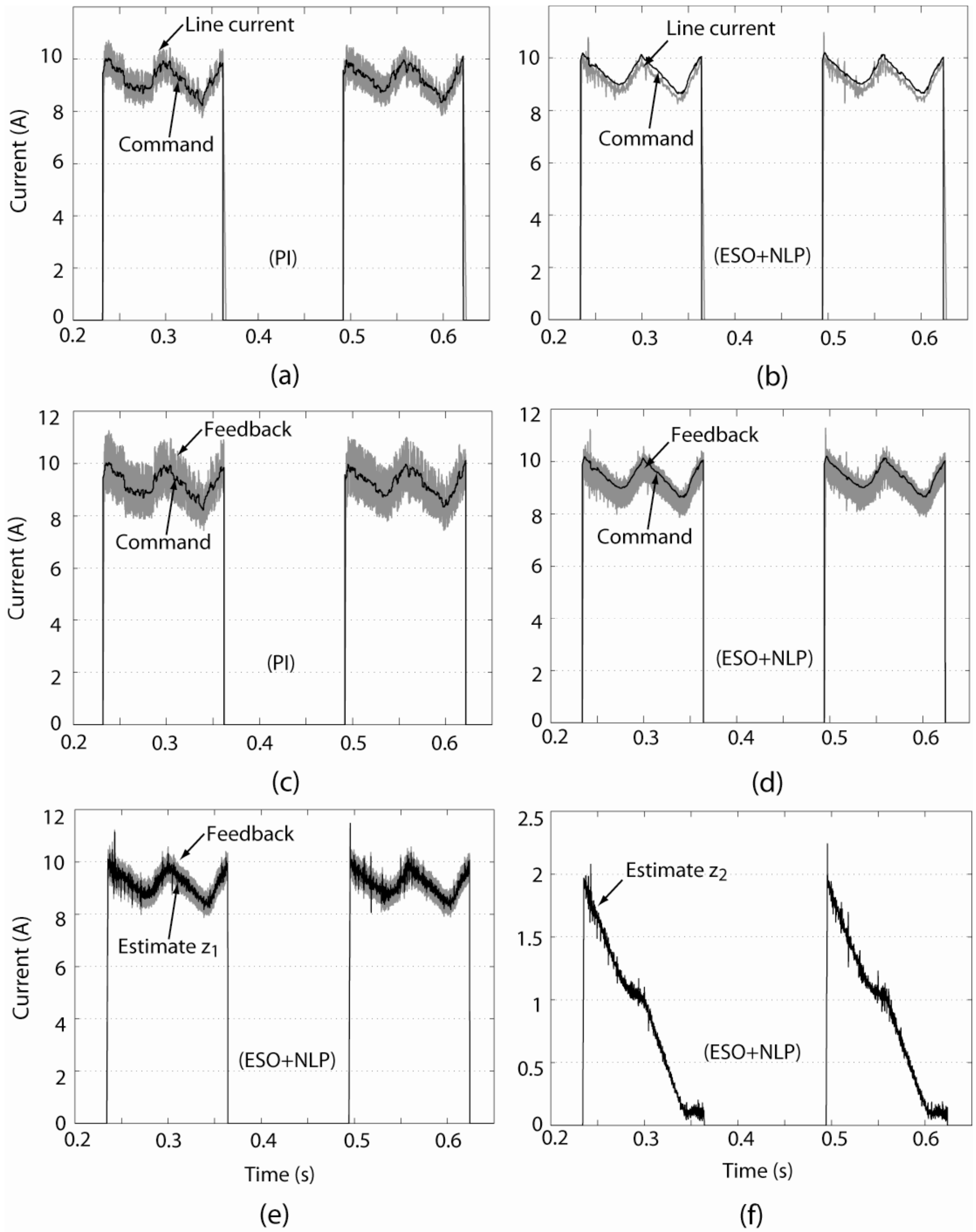

Fig. 4.6 Simulation comparison results of phase current:

(a)-(b) Phase line current: (a) PI, (b) ESO+NLP

(c)-(d) Phase feedback current: (c) PI, (d) ESO+NLP

(e) Feedback current w/ estimate z_1 , (f) Estimated disturbance z_2.

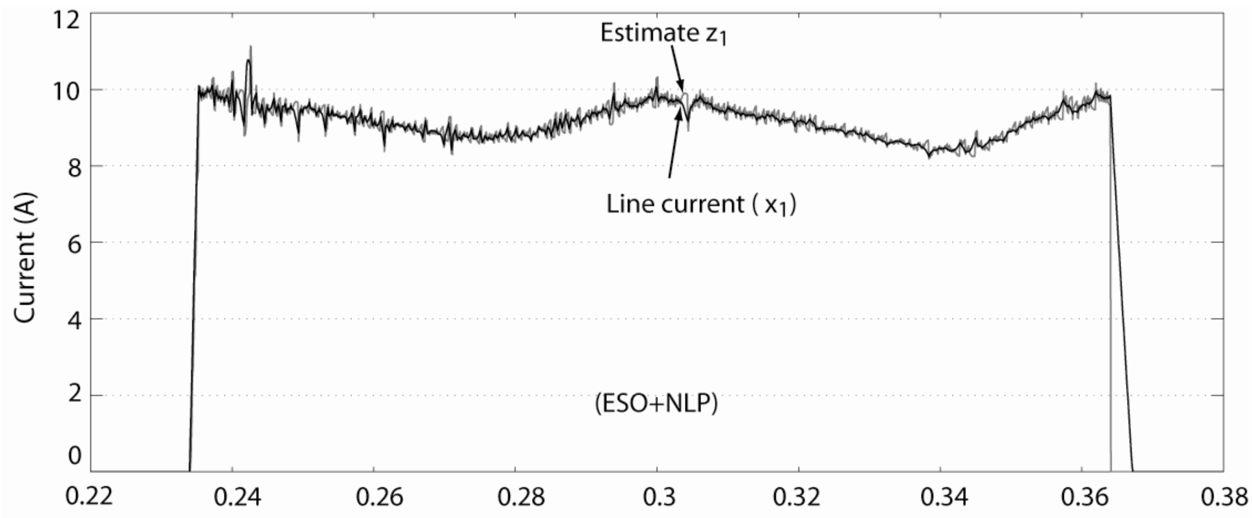

(g)

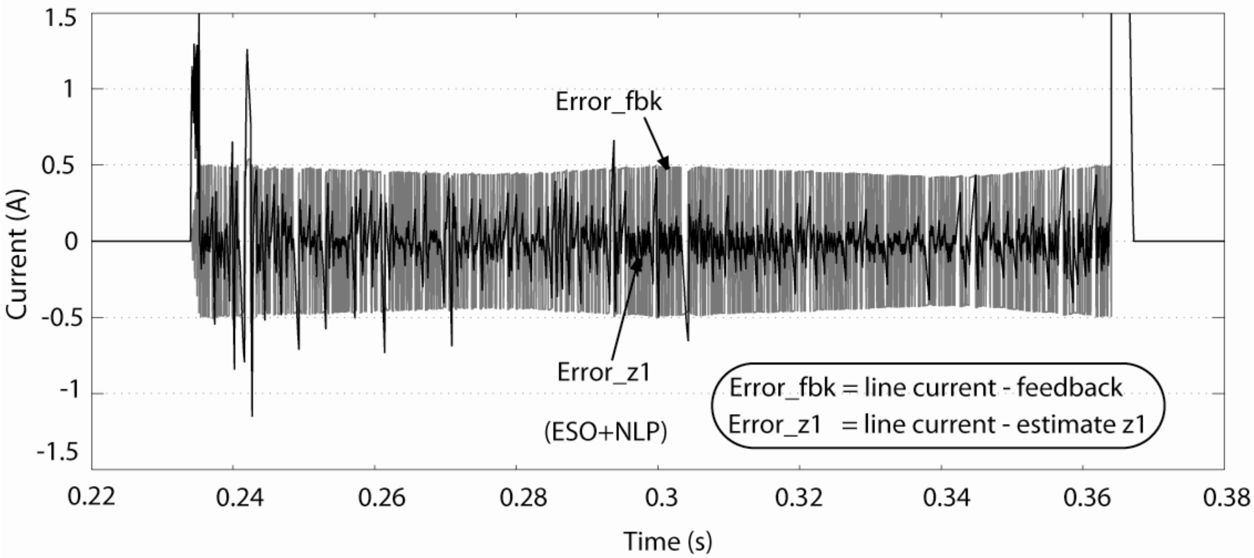

(h)

Fig. 4.6 Simulation comparison results of phase current (continued):

(g) Line current w/ estimate z_1, (h) Errors from line current (x_1).

As expected, force control is largely improved as shown in Fig. 4.7(a). Force ripple should be suppressed, especially in vertical applications such as elevators, which makes the ESO+LNP current control method highly desirable. On the other hand, position and velocity control shown in Fig. 4.7(b) and (c) present no difference between two controllers due to a large mechanical time constant of the elevator. The force ripple is at a very high frequency (*L/R*) compared to the large mechanical time constant of the elevator, *M/*C, where *M* is the mass and *C* is the frictional coefficient. In this simulation, the friction coefficient *C* is 20N/m/sec and mass *M* is 23kg, giving a mechanical time constant of 1.15sec, while a phase inductance of 55mH and the phase resistance of 2.2 Ω give an electrical time constant of 0.025sec. Moreover, position is obtained by integration of velocity, which works as a low pass filter. In this respect, the current measurement disturbance has little effect on the position and velocity control performance.

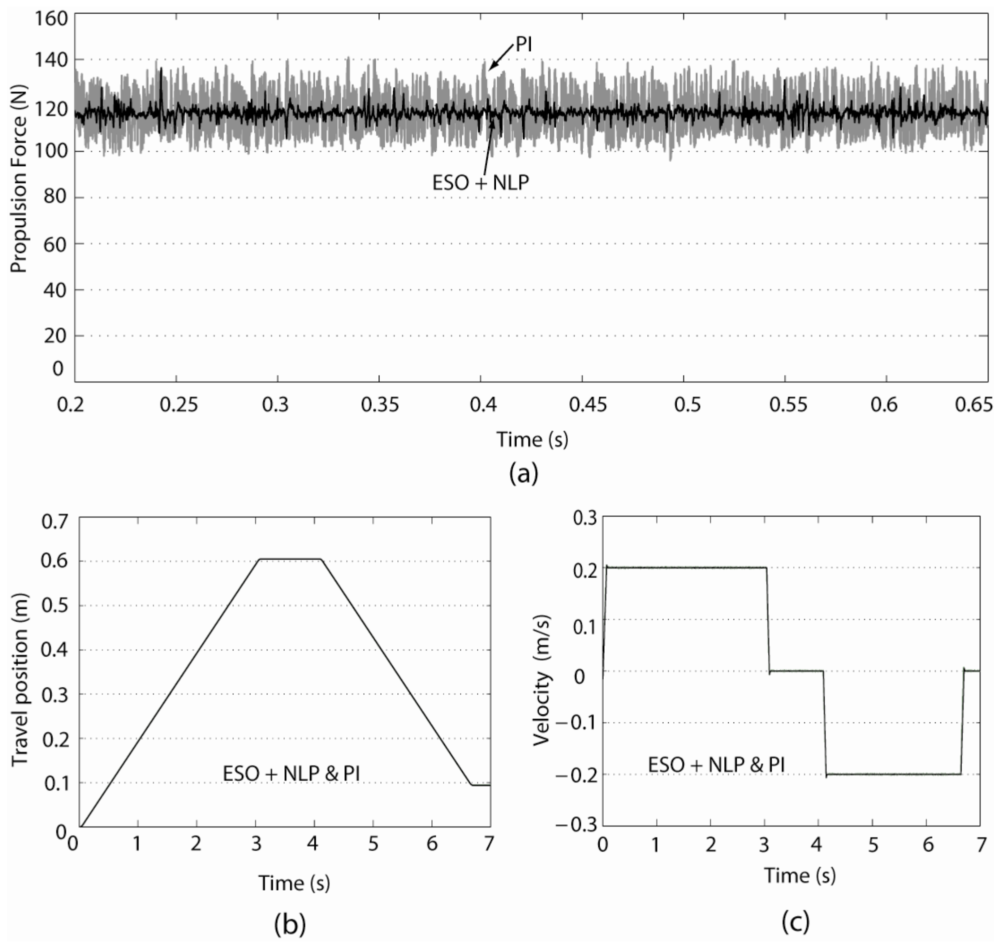

Fig. 4.7 Simulation comparison results: PI vs. ESO+NLP.

(a) Force, (b) Position, and (c) Velocity.

4.7 Experimental results and analysis

A. Experimental Setup

Experimental setup is the same as one presented in Chapter 4. The control strategy discussed in Section 4.5 and simulated in Section 4.6 are implemented on a DSP-based control system with a TI TMS320F240 DSP (10-bit A/D) evaluation module running at 20MHz. PWM duty ratios and gating signals are determined at every 100us by the current controller in the DSP and transferred to each phase's converter boards through an interface board, employing the unipolar PWM switching strategy presented in [22]. A linear incremental magnetic encoder sensor with 10um resolution is used to provide position information to the DSP controller. Current feedback is accomplished by connecting current transducer outputs to the DSP's analog inputs via the interface board, as shown in Fig. 4.4. The parameters of the ESO and NLP in Table 1 are not changed.

B. Experimental Results

Fig. 4.8 compares the performance of the current controllers with measurement disturbance in the prototype LSRM elevator. Line currents are measured through an oscilloscope at 50us sampling rate and shown in Fig. 4.8(a) and (b). The line current noise is much less in applying the ESO+NLP controller because measurement disturbance in the feedback, shown in Fig. 4.8(c), is successfully suppressed by the proposed controller as shown in Fig. 4.8(d). These results correlate well with the simulation results. Fig. 4.8 (e) and (f) show that the ESO effectively estimates the actual line current and measurement disturbance state using z_1 and z_2, respectively. As shown in Fig. 4.4, the estimated states z_1 and z_2 are used in the NLP to compensate for the measurement disturbance and track the current command. The difference in the estimated measurement disturbance, z_2, between the simulation in Fig. 4.6(f) and the experiment in Fig. 4.8(f) comes from uncertain or unmodeled factors such as device voltage drops (IGBT and diode), parameter variations, sensor offsets and ADC conversion errors. Consequently, there is an offset between the simulation and experiment of z_2.

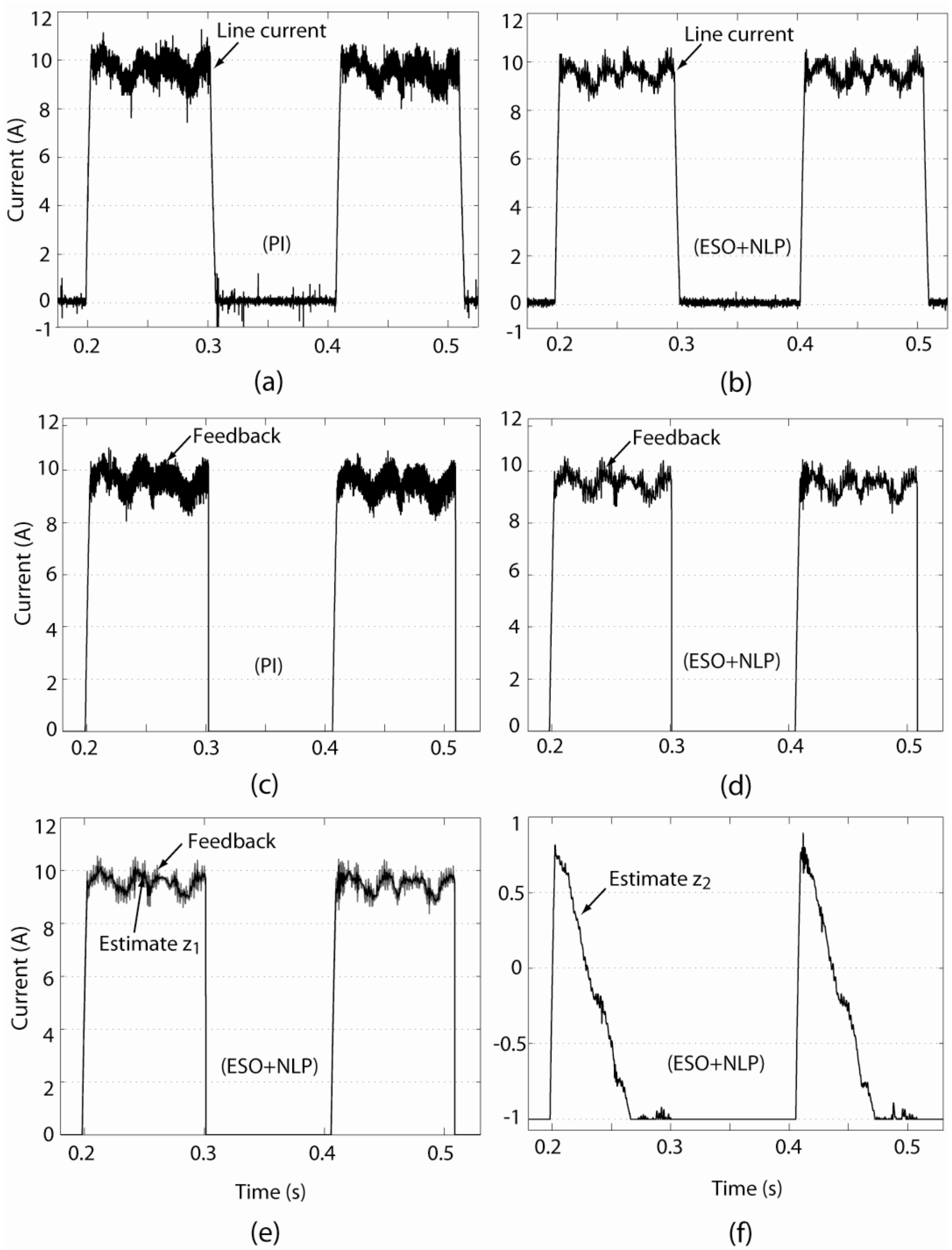

Fig. 4.8 Experiment comparison results of phase current: PI vs. ESO+NLP.

(a) - (b) from oscilloscope (50us sampling) ;(c) - (f) from DSP memory (100us sampling);

(a)-(b) Line current: (a) PI, (b) ESO+ NLP ;

(c)-(d) Feedback current: (c) PI, (d) ESO+ NLP ;

(e) Feedback and estimated current z_1 , (f) Estimated disturbance z_2.

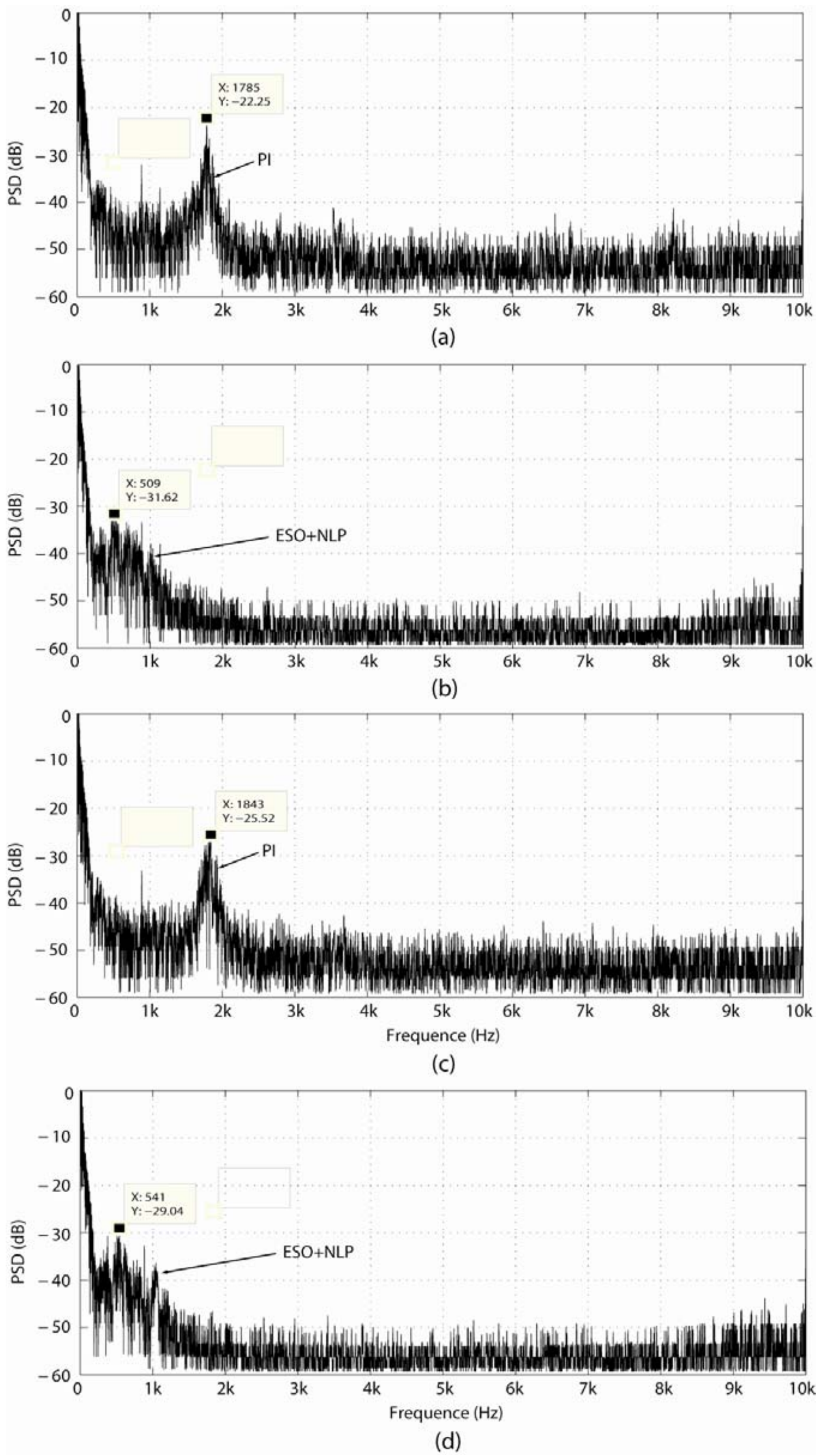

Fig. 4.9 Experiment results of FFT using oscilloscope: PI vs. ESO+NLP. (a)-(b) Line current, (c)-(d) Transducer output current (refer to Fig. 4.4).

In order to demonstrate the ability of the ESO+NLP controller to reduce EMI and acoustic noise, FFT analysis was performed and presented in Fig. 4.9. The proposed current controller suppresses the magnitude of the dominant frequency (~1.8KHz) present in the PI controller, shifting it to a lower frequency (~500Hz). In addition, the FFT magnitude (dB) is decreased up to 10dB with the proposed current controller. As a result, the prototype elevator runs more quietly, which is evidence that force ripple is reduced as in the simulation result of Fig. 4.7(a). Quantitative EMI and sound pressure level measurements are beyond this research and not discussed.

Fig. 4.10 shows experimental results of position and velocity control when applying the PI and ESO+NLP current control method. As shown in simulation results of Fig. 4.7(b) and (c),

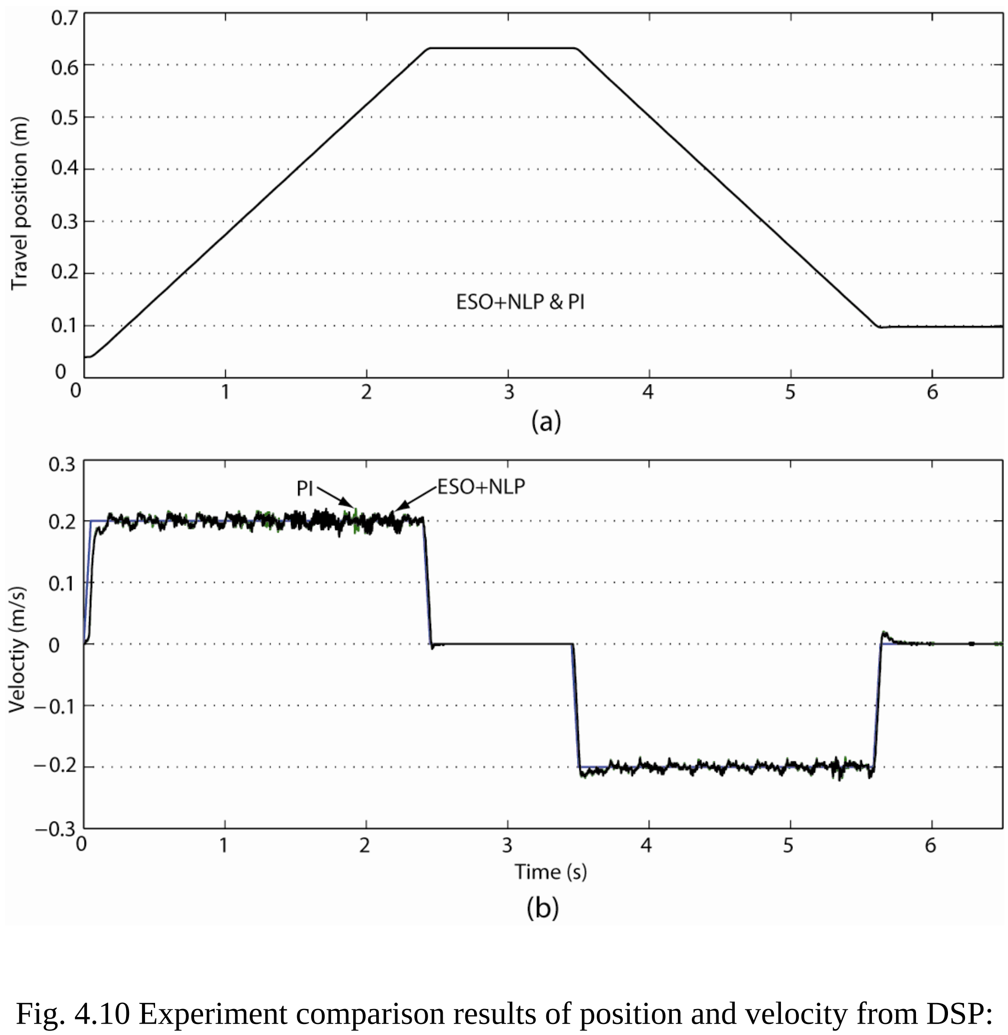

Fig. 4.10 Experiment comparison results of position and velocity from DSP:
(a) Position, (b) Velocity.

position and velocity control performance do not show much difference between two current control strategies because of the large mechanical time constant of the moving vehicle of the elevator. A few papers have proposed velocity and position control methods to improve velocity and position control robustness and performance in the presence of mechanical noise, load disturbances and friction [71]-[74].

4.8 Conclusions

A linear switched reluctance motors (LSRMs) elevator needs an efficient current controller to ensure safety and to reduce force ripple and acoustic noise during vertical operation in the presence of measurement disturbance. In this paper, measurement disturbances caused by factors which corrupt feedback current, such as noise and offset of current sensors, EMI due to PWM converter switching, and voltage drop of switching devices. Therefore, a novel and model-independent measurement disturbance rejection current control method based on an ESO and NLP is proposed to reject measurement disturbances. The following contributions have been made in this chapter:

1) Nonlinear disturbance observers and controllers have been described and reviewed.
2) A novel robust current control technique to reject measurement disturbances in an LSRM drive system for an elevator application is derived, analyzed, simulated, and experimentally verified for the first time. It is based on the ESO and NLP which are largely model-independent and suitable for low cost DSP controllers.
3) Detailed comparison of results from simulations and experiments between a conventional PI and the ESO+NLP current controller are presented with phase currents measured at three different positions: Line, feedback and transducer output current (refer to Fig.4.4). Force, velocity and position control results are also given.
4) FFT analyses are provided to demonstrate the superiority of the ESO+NLP current controller in the presence of measurement disturbances. From the FFT results, it is expected that acoustic noise and EMI are decreased due to enhancement of force control and current control, respectively.

It is believed that the proposed current control technique can be successfully applied into other motor drive systems to suppress measurement disturbances without extra hardware.

CHAPTER 5
CONCLUSIONS

5.1 Conclusions

A ropeless prototype elevator with linear switched reluctance motor (LSRM) drive actuation system has been explored and validated as an alternative linear vertical transverse in this research. Designs of the LSRM for the prototype elevator, analytical aspects of modeling and dynamics of the vehicle, and closed-loop control with a conventional PI method have been presented and verified with comprehensive simulations and experimental results. Furthermore, a novel current control based on an extended state observer (ESO) and nonlinear P controller (NLP) has been proposed to reject measurement disturbances contained in measured phase currents, which are mainly arising from sensor noise and PWM switching noise, DC-link ripple, voltage drop of switching devices, and variations in plant model parameters. The proposed current control algorithm has proven to enhance total current and force control performance through dynamic simulations and experiments, resulting in a reduction of force ripple and acoustic noise. The major contributions of this study are summarized as follows:

1) A novel LSRM topology for a prototype elevator has been proposed and designed using the current knowledge and design procedure of rotating switched reluctance machine [6]. The prototype LSRMs are scaled down from the designed ship elevator presented by the author [1] and optimized to be suitable for the prototype elevator with propulsion force of 300N. Experimental correlation of inductances and propulsion force to FEA simulation results has confirmed the validity of the proposed design procedure.

2) A prototype elevator with a size of 22 x 26 x 50 (WxLxH) inches and a travel length of 0.67m has been built using two assembled LSRMs. Translators are installed on a moving vehicle whose size is 12 x 12 x 14 (WxLxH) inches and total weight is 20.3 kg. The rate velocity is set to 0.2m/s and the rated payload 24kg at 10A including vehicle weight.

3) A novel force distribution functions (FDF) have been proposed, analyzed and compared with conventional FDFs through dynamic simulations. In addition, the superior force control with the proposed FDF for the prototype elevator has been implemented and successfully verified by way of the dynamic simulations and the experimental tests.

4) PI controllers for the current control loop and velocity control loop have been explained, employed and validated via the dynamic simulations and the experiments. A trapezoidal velocity profile has been also applied to the prototype elevator to control position during moving as well as stop. The simulations and experiments have been successfully performed at different velocities from 0.15m/s to 0.3m/s as well as with different payloads of 23kg and 32kg. Moreover, the correlation of results between the dynamic simulations and the experiments has been established.

5) A DSP-based control system with TI TMS320F240 has been realized to execute the control strategy for the prototype LSRM elevator. For converter side, four asymmetric half-bridge converters have been implemented along with a unipolar switching strategy [3] for the test of the prototype LSRM elevator. The asymmetric half-bridge converter topology has high control flexibility, fault tolerance and reliability of which features need to be ensured for elevator applications.

6) A novel robust current control technique to reject measurement disturbances on phase currents in this LSRM elevator application is derived, analyzed, simulated, and experimentally verified for the first time. It is based on the ESO and NLP which are largely model-independent and suitable for low cost DSP controllers.

7) FFT analyses are provided to demonstrate the superiority of the ESO+NLP current controller in the presence of measurement disturbances. From the FFT results, it is expected that acoustic noise and EMI are decreased due to enhancement of force control and current control, respectively. It is believed that the proposed current control technique can be

successfully applied into other motor drive systems to suppress measurement disturbances without extra hardware.

5.2 Papers published in Journals and Conference Proceedings

Out of this research, the following papers have been published and accepted for publication in IEEE journals and conference proceedings.

[1] H.S. Lim, R, Krishnan and N.S. Lobo, "Design and Control of a Linear Propulsion System for an Elevator Using Linear Switched Reluctance Motor Drives," accepted for publication in *IEEE Trans. on Industrial Electronics,* August 2007.

[2] H.S. Lim and R, Krishnan, "A Ropeless Elevator with Linear Switched Reluctance Motor Drive Actuation Systems," accepted for publication in *IEEE Trans. on Industrial Electronics,* 2007.

[3] N.S. Lobo, H.S. Lim and R. Krishnan, "Comparison of Linear Switched Reluctance Machines for Vertical Propulsion Application: Analysis, Design and Experimental Correlation", under review for publication in *IEEE Trans. on Industry Applications,* 2007.

[4] H.S. Lim and R, Krishnan, "Novel Measurement Disturbance Rejection Current Control for Linear Switched Reluctance Motor Drives," prepared for publication in *IEEE Trans. on Industry Applications,* 2007.

[5] H.S. Lim, R, Krishnan and N.S. Lobo, "Design and Control of a Linear Propulsion System for an Elevator Using Linear Switched Reluctance Motor Drives," *Proc. of IEEE Int. Electric Machines and Drives Conf.*, pp. 1584-1591, May 2005.

[6] N.S. Lobo, H.S. Lim and R. Krishnan, "Comparison of Linear Switched Reluctance Machines for Vertical Propulsion Application: Analysis, Design and Experimental Correlation", *Rec. of IEEE Industry Applications Society Annual Meeting*, vol.1, pp. 385-392, October 2006.

[7] H.S. Lim and R, Krishnan, “Novel Measurement Disturbance Rejection Current Control for Linear Switched Reluctance Motor Drives,” accepted for presentation at *IEEE Industry Applications Society Annual Meeting,* September 2007.

5.3 Recommendations for Future Work

The following avenues of research are to be considered for elevator applications suitable for implementation in industries with the LSRM technologies proposed in this research:

1) **Safety**: Elevator applications are all about safety. Emergency cases must be taken into consideration to prevent from stopping in the middle of floors or dropping on the ground: For example, power failure and operation failure (due to malfunction of position sensors and/or controllers). Thus, DC batteries or self-sustaining power units are required to be ready for a power-off case and break system must be reliable in case of emergency. In addition, a monitoring and back-up control system would be necessary to secure control systems during operation.

2) **Power Efficiency**: Ropeless elevators do not use counter weights. As a result, their power efficiency is known to be lower by 50% than conventional traction geared rope elevators which have counter weights. In this regard, home elevators are largely considered as a appropriate application area at present. In order to extend its application area as a potential alternative to elevators in commercial and business buildings, increasing energy efficiency must be taken into account as one of most important factors.

3) **Construction**: As other linear motors, the proposed LSRM topology has a large normal force between stators and translators even though it is balanced due to twin stators and double-sided translator poles in between stators. Therefore, a careful design of stator configuration for ropeless LSRM elevators is required to securely install on the surface of wall in a building or house, resulting in overcoming such a high normal force, and hence maintaining air gap during operation. Furthermore, in order to prevent translators from hitting stators during operation, a long-lasting plastic type of material may be helpful as a air gap spacer. In

this research, white thin plastic bars are attached on the sides of translator poles. Refer to Fig. 2.7 in Chapter 2.

4) **Maintenance**: Translator assemblies can be made in a type of module consisting of eight translator poles, for example in case of 8/6 type of LSRM. In this research, two translator modules are used on each side. Thus, they can be easily dismantled and replaced with another module in case of repairment of translators. In full-scale elevators, several translator modules can be placed in between twin stators to generate demanded propulsion forces. A number of translator modules will share a total demanded propulsion force with each translator module.

Concerning the proposed current control, it is believed that a universal measurement disturbance current control derivation based on the proposed current control algorithm will gain a lot of interest from drive and instrument companies and be adopted. To this end, following studies are suggested.

1) Dynamic simulations using main two AC motors to prove the methodology; they are Permanent Magnet and induction motors.

2) Experimental verification of the proposed current control algorithm applied to AC motors.

APPENDIX A:

Derivation of K_p and K_i

For a given system transfer functions $G_c(s)$,

$$G_c(s) = \frac{2\zeta_c \omega_n s + \omega_n^2}{s^2 + 2\zeta_c \omega_n s + \omega_n^2} \tag{A.1}$$

where

$$\begin{aligned} 2\zeta_c \omega_n &= K_1 K_p \\ \omega_n^2 &= K_1 K_p K_i \end{aligned} \tag{A.2}$$

the system bandwidth ω_c is the frequency at which the magnitude of $G_c(j\omega)$ drops to $1/\sqrt{2}$ of its zero-frequency value. Thus we have

$$\left| G_c(j\omega) \right|_{\omega=\omega_c} = \sqrt{\frac{\left(\omega_n^2\right)^2 + \left(2\zeta_c \omega_n \omega_c\right)^2}{\left(-\omega_c^2 + \omega_n^2\right)^2 + \left(2\zeta_c \omega_n \omega_c\right)^2}} = \frac{1}{\sqrt{2}} \tag{A.3}$$

By rearranging Eq. (A.3), we have

$$\omega_c^4 - 2\left(1 + 2\zeta_c^2\right)\omega_n^2 \omega_c^2 - \omega_n^4 = 0 \tag{A.4}$$

This equation leads to

$$\omega_c^2 = \left(1 + 2\zeta_c^2\right)\omega_n^2 \pm \sqrt{\left(1 + 2\zeta_c^2\right)^2 + 1} \cdot \omega_n^2 \tag{A.5}$$

Since ω_c is a positive real value for any ζ_c, the plus sign should be chosen in Eq. (A.5). Therefore the bandwidth ω_c of the second order system is determined as,

$$\omega_c = \sqrt{\left(1 + 2\zeta_c^2\right) + \sqrt{\left(1 + 2\zeta_c^2\right)^2 + 1}} \cdot \omega_n \tag{A.6}$$

By rearranging Eq. (A.2) for the controller gains K_p and K_i, we have

$$K_p = \frac{2\zeta_c \omega_n}{K_1}$$
$$K_i = \frac{\omega_n^2}{K_1 K_p} = \frac{\omega_n^2}{K_1 \frac{2\zeta_c \omega_n}{K_1}} = \frac{\omega_n}{2\zeta_c} \tag{A.7}$$

Substituting Eq. (A.6) into Eq. (A.7) yields

$$K_p = \frac{2\zeta_c \omega_c}{\sqrt{\left(1+2\zeta_c^2\right)+\sqrt{\left(1+2\zeta_c^2\right)^2+1}}} \cdot \frac{1}{K_1}$$
$$K_i = \frac{\omega_c}{2\zeta_c \sqrt{\left(1+2\zeta_c^2\right)+\sqrt{\left(1+2\zeta_c^2\right)^2+1}}} \tag{A.8}$$

Hence, for a given set of the bandwidth ω_c and the damping ratio ζ_c, the controller gains K_p and K_i are calculated algebraically as above.

APPENDIX B:

Convergence Proof of the Closed-loop Based on the Proposed ESO and NLPD

The convergence proof for a second order ESO is already given by Huang, *et. al* in [84]. In addition, the convergence of a second order closed-loop system based on an ESO is proved in [68]. Since the application is changed, the convergence problem is redefined as below. Then, the proof is described based on the given control system. Considering a generalization of the proposed measurement disturbance rejection control, a nonlinear proportional plus derivative controller (NLPD) is taken into account for the proof, instead of NLP.

For the given system as described in (4.6) of Chapter 4,

$$\begin{cases} \dot{x}_1(t) = x_2(t) + bu(t) \\ \dot{x}_2(t) = a(t), \;\; a(t) \equiv f(x_1, x_2, w(t)) \\ y(t) = x_1(t) \end{cases} \tag{B.1}$$

the proposed ESO is given as,

$$\begin{aligned} \dot{z}_1(t) &= z_2(t) + bu(t) - \beta_{01} fal(e, \alpha, \delta) \\ \dot{z}_2(t) &= -\beta_{02} fal(e, \alpha, \delta) \end{aligned} \tag{B.2}$$

where,

$$\begin{aligned} & fal(e, \alpha, \delta) = \begin{cases} |e|^{\alpha} sign(e), \;\; |e| > \delta \\ \dfrac{e}{\delta^{1-\alpha}}, \;\; |e| \le \delta \end{cases} , (0 < \alpha < 1, \delta > 0) \\ & e = z_1 - y \end{aligned} \tag{B.3}$$

The plant of (B.1) can be simplified with the control input $u(t)$ given below,

$$u(t) = \left(u_0(t) - z_2(t)\right)/b \tag{B.4}$$

where $u_0(t)$ is a new control input which is generated by the NLPD. Assuming that the proposed ESO shown in (B.2) successfully estimates the disturbance state $x_2(t)$ and using (B.4) as the control input, the original plant is simplified to a single integrator control problem of

$$\begin{aligned}\dot{x}_1(t) &= u_0(t)\\ y(t) &= x_1(t)\end{aligned} \tag{B.5}$$

The proposed NLPD is given below to produce the new control input $u_0(t)$,

$$\begin{aligned}u_0 &= K_{pc} \cdot e_{ierr\_p} + K_{dc} \cdot e_{ierr\_d}\\ &= \left[k_{pc}\, fal(e_{ierr\_p}, \alpha_{pc}, \delta_{pc})\right] + \left[k_{dc}\, fal(e_{ierr\_d}, \alpha_{dc}, \delta_{dc})\right]\end{aligned} \tag{B.6}$$

where,

$$\begin{aligned}&e_{ierr\_p} = x_1 - z_1, e_{ierr\_d} = \frac{de_{ierr\_p}}{dt} = \dot{x}_1 - \dot{z}_1\\ &fal(e,\alpha,\delta) = \begin{cases}|e|^{\alpha}\, sign(e), |e| > \delta\\ \dfrac{e}{\delta^{1-\alpha}}, |e| \le \delta\end{cases} ,(0 < \alpha < 1, \delta > 0)\\ &e = e_{ierr\_p} \text{ or } e_{ierr\_d}\end{aligned} \tag{B.7}$$

where α and δ are constants to be tuned for each control gain.

Now the convergence of the system given in (B.1) based on the ESO (B.2) and NLPD (B.6) is given by the following theorem.

Theorem [68]: *For any bounded integrable function* $x_1^*(t)$ *and any constant T > 0, solution of system (B.5) satisfies*

$$\lim_{k_{pc}\&k_{dc}\to\infty} \int_0^T \left|x_1(t) - x_1^*(t)\right| dt = 0 \tag{B.8}$$

which means $x_1(t)$ *can track* $x_1^*(t)$ *as the NLPD controller gains,* k_{pc} *and* k_{dc}*, go to infinity.*

Proof: (1) If $x_1^*(t)$ is a constant, then $\dot{x}_1^*(t)$ =0 and $\dot{x}_1(t) = \dot{x}_1(t) - \dot{x}_1^*(t)$. Let $m(k_x t) = x_1(t) - x_1^*(t)$. Substituting it into (B.5) along with (B.6) yields

$$\begin{aligned}\dot{m}(k_x t) &= u_0(t)\\ &= K_{pc}\cdot e_{ierr\_p} + K_{dc}\cdot e_{ierr\_d}\\ &= \left[k_{pc}\, fal(e_{ierr\_p},\alpha_{pc},\delta_{pc})\right] + \left[k_{dc}\, fal(e_{ierr\_d},\alpha_{dc},\delta_{dc})\right]\\ &= \left[k_{pc}\, fal(x_1^*(t)-x_1(t),\alpha_{pc},\delta_{pc})\right] + \left[k_{dc}\, fal(\dot{x}_1^*(t)-\dot{x}_1(t),\alpha_{dc},\delta_{dc})\right]\\ &= \left[k_{pc}\, fal(-m(k_x t),\alpha_{pc},\delta_{pc})\right] + \left[k_{dc}\, fal(-\dot{m}(k_x t),\alpha_{dc},\delta_{dc})\right]\end{aligned} \tag{B.9}$$

where k_x represents the NLPD controller constant gains, k_{pc} and k_{dc}. Since the nonlinear function $fal(e,\alpha,\delta)$ is an odd function with respect to the error term e as shown in (B.7), the above (B.9) can be rewritten as

$$\dot{m}(k_x t) = -\left[k_{pc}\, fal(m(k_x t),\alpha_{pc},\delta_{pc})\right] - \left[k_{dc}\, fal(\dot{m}(k_x t),\alpha_{dc},\delta_{dc})\right] \tag{B.10}$$

Define the Lyapunov function for the system (B.10) as $V = \frac{1}{2} m^2(k_x t)$. Differentiating the Lyapunov function with respect to time, t, yields

$$\dot{V} = m(k_x t)\cdot \dot{m}(k_x t) \tag{B.11}$$

Then, substituting (B.10) into (B.11) produces

$$\dot{V} = m\cdot\dot{m} = -m\left(\left[k_{pc}\, fal(m,\alpha_{pc},\delta_{pc})\right] + \left[k_{dc}\, fal(\dot{m},\alpha_{dc},\delta_{dc})\right]\right) \tag{B.12}$$

The nonlinear function $fal(e,\alpha,\delta)$ can be simplified as

$$\begin{aligned} fal(e,\alpha,\delta) &= \begin{cases} |e|^{\alpha}\, sign(e), & |e| > \delta \\ \dfrac{e}{\delta^{1-\alpha}}, & |e| \le \delta \end{cases} \quad ,(0<\alpha<1,\delta>0)\\ &\equiv \begin{cases} K_1\cdot e, & |e|>\delta, K_1 = |e|^{\alpha}\Big|_{\alpha\&\delta=fixed} \\ K_2\cdot e, & |e|\le\delta, K_2 = \delta^{\alpha-1}\Big|_{\alpha\&\delta=fixed} \end{cases}\\ &\cong K\cdot e, K>0 \end{aligned} \tag{B.13}$$

Substituting (B.13) into (B.12) yields

$$\begin{aligned}\dot{V} = m \cdot \dot{m} &= -m\left(\left[k_{pc}\, fal(m, \alpha_{pc}, \delta_{pc})\right] + \left[k_{dc}\, fal(\dot{m}, \alpha_{dc}, \delta_{dc})\right]\right) \\ &= -m\left[k_{pc} K_P m\right] - m\left[k_{dc} K_D \dot{m}\right] \\ &= -k_{pc} K_P m^2 - k_{dc} K_D m \cdot \dot{m}\end{aligned} \tag{B.14}$$

Rearranging (B.14) for $m \cdot \dot{m}$ gives

$$m \cdot \dot{m} = -\frac{k_{pc} K_P m^2}{1 + k_{dc} K_D} \tag{B.15}$$

From (B.15), since constants, k_{pc}, k_{dc},K_P, and K_D are positive, the Lyapunove function V is negative:

$$\dot{V} = m \cdot \dot{m} = -\frac{k_{pc} K_P m^2}{1 + k_{dc} K_D} < 0 \tag{B.16}$$

Therefore, (B.10) is convergent as described below,

$$\lim_{k_x t \to \infty} m(k_x t) = 0\,. \tag{B.17}$$

As a result, for any 0 < t < T, we have

$$\lim_{k_x \to \infty} \int_0^T \left|m(k_x t)\right| dt = \lim_{k_{pc} \& k_{dc} \to \infty} \int_0^T \left|x_1(t) - x_1^*(t)\right| dt = 0 \tag{B.18}$$

(2) From this part on, the second proof part in reference [68] is excerpted. If $x_1^*(t)$, $t \in [0, T]$, is a bounded integrable function, then $\forall \varepsilon > 0$, there exists a continuous $\phi(t)$ satisfying

$$\int_0^T \left|x_1^*(t) - \phi(t)\right| dt < \frac{\varepsilon}{4} \tag{B.19}$$

For the function $\phi(t)$, there exits a sequence of functions $\varphi_n(t), (n = 1, 2, \ldots)$, converging to $\phi(t)$ consistently. Thus $\exists N_0$, a sufficiently large positive integer, when M > N_0, $\left|\phi(t) - \varphi_M(t)\right| < \dfrac{\varepsilon}{4T}$. Then,

$$\int_0^T \left| x_1^*(t) - \varphi_M(t) \right| dt < \int_0^T \left| x_1^*(t) - \phi(t) \right| dt + \int_0^T \left| \phi(t) - \varphi_M(t) \right| dt < \frac{\varepsilon}{2} \tag{B.20}$$

Since $\phi(t)$ is a continuous function, $\varphi_M(t)$ divides the region [0,T] into a finite number of smaller regions where $\varphi_M(t)$ has constant values in each small region. From the first part of the proof, we know that the following inequality holds for a sufficiently large k_x,,

$$\int_0^T \left| x_1^*(t) - \varphi_M(t) \right| dt < \frac{\varepsilon}{2} \tag{B.21}$$

Thus for a sufficiently large k_x,

$$\int_0^T \left| x_1(t) - x_1^*(t) \right| dt < \int_0^T \left| x_1(t) - \varphi_M(t) \right| dt + \int_0^T \left| \varphi_M(t) - x_1^*(t) \right| dt < \varepsilon \tag{B.22}$$

Therefore, (B.22) proves (B.8) and hence gives a complete proof for the above Theorem.

APPENDIX C:

LSRM PARAMETER OF THE PROTOTYPE LINEAR ELEVATOR

Power capacity	24 W
Rated velocity	0.2 m/s
Rated force	120 N
Rated phase current	10 A
Number of turns per phase	396, AWG #18
L_{min} at rated current (measured)	52.5mH
L_{max} at rated current (measured)	20.7mH
Phase resistance	2.2 Ω
Mass of the vehicle	20.3kg
Air gap length	1.5 mm

REFERENCES

[1] H.S. Lim, R, Krishnan and N.S. Lobo, "Design and Control of a Linear Propulsion System for an Elevator Using Linear Switched Reluctance Motor Drives," accepted for publication in *IEEE Trans. on Industrial Electronics,* August, 2007.

[2] P.-K. Budig, "The application of linear motors," in *Proc. 3rd IEEE Int. Power Electronics and Motion Control Conf.*, vol.3, pp. 1336 –1341, August 2000.

[3] I. Boldea and S. A. Nasar, "Linear Motion Electromagnetic Devices," USA, Taylor & Francis, 2001.

[4] T. Ishii, "Elevators for skyscrapers," in *IEEE Spectrum*, vol. 31, pp. 42-46, September 1994

[5] H.K. Bae, B.S. Lee, P. Vijayranghavan, and R. Krishnan, "A Linear Switched Reluctance Motor: converter and control", in *IEEE Trans. on Industry Application,* vol.36, pp. 1351 – 1359, Sept./Oct. 2000.

[6] W.C. Gan; N.C. Cheung; L. Qiu; "Position control of linear switched reluctance motors for high-precision applications", in *IEEE Trans. on Industry Application*.vol.39, pp. 1350 – 1362, Sept./Oct., 2003.

[7] J. Corda and E. Skopljak, "Linear switched reluctance actuator," in *Proc. 6th IEEE Int. Electric Machines and Drives Conf.*, pp. 535-539, September 1993.

[8] B.S. Lee, H.K. Bae, P. Vijayranghavan, and R. Krishnan, "Design of a linear switched reluctance machine," in *IEEE Trans. on Industry Application.*, vol.36, pp. 1571 – 1580, Nov./Dec. 2000.

[9] C.T. Liu and J.L. Kuo, "Experimental investigation and 3-D modeling of linear variable-reluctance machines with magnetic flux decoupled windings", in *IEEE Trans. on Magnetics*., vol.30, pp. 4737 – 4739, November 1994.

[10] U.S. Deshpande, J.J. Cathey, and E. Richter, "High-force density linear switched reluctance machine," in *IEEE Trans. on Industry Applications*, vol. 31, no. 2, pp. 345-352, March/April 1995.

[11] B.S. Lee, *Linear Switched Reluctance Machine Drives with Electromagnetic Levitation and Guidance Systems*, Ph. D. Thesis in The Bradley Department of Electrical & Computer Engineering, Virginia Tech. Blacksburg, Virginia, November, 2000

[12] C.T. Liu and T.S. Chiang, "On the magnetic saturation analyses of a micro linear switched-reluctance motor," in *IEEE Trans. on Magnetics*, vol. 40, Issue 4, Part 2, pp. 2861 – 2863, July 2004

[13] J.F. Gieras, P.D. Hartzenberg, I.J. Magura, and M. Wing, "Control of An Elevator Drive With A Single-sided Linear Induction Motor," European Power Electronics Association EPE, pp 353 – 357, September 1993.

[14] H. Yamada, Y. Nakamura, and T. Nakada, "Vertical Motion Analysis of a Linear Induction Motor Elevator," in *Proc. 1st International Symposium on Linear Drives for Industry Applications LDIA*, pp. 77-80, 1995.

[15] K. Toida, T. Honda, H. Kim, M. Watada, S. Torii, and D.Ebihara, "The Positioning Control with Velocity Feed-Forward for the Rope-less Elevator using Linear Synchronous Motor", in Conf. Rec.IEEE Elec. Mach. and Driv. , pp. 18-21, May 1997.

[16] H. J. Kim, I. Muraoka, S. Torii, M. Watada, and D. Ebihara, "The Study of the Control System for Ropeless Elevator with Vertical Linear Synchronous Motor," in *Proc. 1st International Symposium on Linear Drives for Industry Applications LDIA*, pp. 69-72, 1995.

[17] M. Miyatake, N. Ishkawa, T. Koseki, and S. Sone, "Experimental and Operational Study on Vertical Transportation System Driven by a Linear Synchronous Motor Using Permanent Magnets," in *Proc. 1st International Symposium on Linear Drives for Industry Applications LDIA*, pp. 73-76, 1995.

[18] K. Yoshida and H. Matsumoto, "Propulsion and Guidance Simulation of a High-Temperature Superconducting Bulk Ropeless Linear Elevator," in *IEEE Trans. on Magnetics*, vol. 40, No. 2, pp. 615 –618, March 2004.

[19] N.S. Lobo, H.S. Lim and R. Krishnan, “Comparison of Linear Switched Reluctance Machines for Vertical Propulsion Application: Analysis, Design and Experimental Correlation”, in *Rec. of IEEE Industry Applications Society Annual Meeting*, vol.1, pp. 385-392, October 2006.

[20] R. Krishnan, “Switched Reluctance Motor Drives: Modeling, Simulation, Analysis, Design, and Applications,” USA, CRC Press LLC, June 2001.

[21] D.S. Schramm, B.W. Williams, and T.C. Green, “Torque ripple reduction of switched reluctance motors by phase current optimal profiling,” in *Proc. IEEE Annual Power Electronics Specialists Conference,* 1992, pp. 857–860.

[22] H.K. Bae and R. Krishnan, “A study of current controllers and development of a novel current controller for high performance SRM drives,” in *Conf. Rec. IEEE-IAS Annu. Meeting*, 1996, pp. 68-75.

[23] K. Adamiak, D. Barlow, C.P. Choudhury, P.M. Cusack, G.E. Dawson, A.R. Eastham, B. Grady, E. Ho, Y. Hongping, L. Pattison, and J. Welch, “The switched reluctance motor as a low-speed linear drive,” in *Intl. Conf. on Maglev and Linear Drives*, Las Vegas, NV, pp. 39-43, May 1987.

[24] K. Takayama, Y. Takasaki, R. Ueda, T. Sonoda, and T. Iwakane, “A new type switched reluctance motor,” in *Conf. Rec. of the IEEE IAS Ann. Mtg.*, Pittsburgh, PA, vol. 1, pp. 71-78, October 1988.

[25] K. Takayama, Y. Takasaki, R. Ueda, and T. Sonoda, “Thrust force distribution on the surface of stator and rotor poles of switched reluctance motor,” in *IEEE Trans. on Magnetics*, vol. 25, no. 5, pp. 3997-3999, September 1989.

[26] P.M. Cusack, G.E. Dawson, and T.R. Eastham, “Design, control and operation of a linear switched reluctance motor,” in *Canadian Conf. on Electrical and Computer Eng.*, Quebec, CA, pp. 19.1.1-19.1.5, September 1991.

[27] C.T. Liu and Y.N. Chen, “On the feasible polygon classifications of linear switched reluctance machines,” in *IEEE Intl. Electric Machines and Drives Conf. Rec.*, Milwaukee, WI, pp. TB1/11.1-TB1/11.3, May 1997.

[28] C.T. Liu, K.S. Su, and M.H. Lee, "Three dimensional field and side-force design analyses of a transverse flux linear switched-reluctance machine," in *IEEE Trans. on Magnetics*, vol. 34, no. 4, pp. 2132-2134, July 1998.

[29] C.T. Liu and N. Sheu, "Optimal pole arrangement design of a linear switched-reluctance machine for magnetic levitation and propulsion system," in *IEEE Trans. on Magnetics*, vol. 32, no. 5, pp. 5067-5069, September 1996.

[30] U. Deshpande, "Two-dimensional finite-element analysis of a high-force-density linear switched reluctance machine including three-dimensional effects," in *IEEE Trans. on Industry Applications*, vol. 36, no. 4, pp. 1047-1052, July/August 2000.

[31] J. Corda, and M. Wilkinson, "Prediction and measurement of magnetic parameters of cylindrical linear switched reluctance actuator," in *Proc. of Intl. Conf. on Electrical Machines*, Paris, Fr., vol. 3, pp. 479-484, September 1994.

[32] J. Corda and M. Wilkinson, "Modelling of static thrust characteristics of cylindrical linear switched reluctance actuator," in *Seventh Intl. Conf. on Electrical Machines and Drives*, Durham, UK, IEE Conference Publication, no. 412, pp. 354-358, September 1995.

[33] D. Matt, R. Goyet, J. Lucidarme, and C. Rioux, "Longitudinal-field multi-airgap linear reluctance actuator," in *Electric Machines and Power Systems*, vol. 13, no. 5, pp. 299-313, 1987.

[34] J. Lucidarme, A. Amouri, and M. Poloujadoff, "Optimum design of longitudinal field variable reluctance motors-application to a high performance actuator," in *IEEE Trans. on Energy Conversion*, vol. 8, no. 3, pp. 357-361, September 1993.

[35] I. Boldea and S.A. Nasar, *Linear Electric Actuators and Generators*, Cambridge University Press, UK, pp. 163-178, 1997.

[36] Han-Kyung Bae, *Control of Switched Reluctance Motors Considering Mutual Inductance*, Ph. D. Thesis in The Bradley Department of Electrical & Computer Engineering, Virginia Polytechnic Institute & State University, Blacksburg, Virginia, August 2000.

[37] C.T. Liu, K.S. Su and J.W. Chen, "Operational stability enhancement analysis of a transverse flux linear switched-reluctance motor," in *IEEE Trans. on Magnetics,* vol. 36, Issue 5, Part 1, pp.3699 – 3702, September 2000

[38] C.T. Liu and S.Y. Lin, **"**An orthogonal control scheme of linear switched-reluctance motor for magnetic levitated vehicle applications," in *IEEE Power Engineering Society Winter Meeting,* , vol. 1, pp. :249 – 252, January 2000

[39] P.C.K. Luk; P. Jinupun, "Instantaneous thrust control for a linear switched reluctance motor," in *IEEE 35th Annual Power Electronics Specialists Conference*, vol. 3, pp. 2265 – 2269, June 2004

[40] J. L. Domingos, D. A. Andrade, M.A.A. Freitas, and H.De Paula, "Four-quadrant operation drive strategy for a linear switched reluctance motor," in *IEEE International Symposium on Industrial Electronics*, vol. 1, pp. 210 – 215, June 2003

[41] I. Husain and M. Ehsani, "Torque Ripple minimization in Switched Reluctance Motor Drives by PWM Current Control," in *IEEE Transactions on Power Electronics*, vol. 11, no.1, pp. 83-88,1996.

[42] M. Ilic-Spong, T.J.E. Miller, S.R. Macminn, and J. S. Thorp, "Instantaneous Torque Control of Electric Motor Drives," in *IEEE Transactions on Power Electronics*, vol. 2, no.1, pp. 55-61,1987.

[43] R.S. Wallace and D.G. Taylor, "A Balanced Commutator for Switched Reluctance Motors to Reduce Torque Ripple," in *IEEE Transactions on Power Electronics*, vol. 7, no.4, pp. 617-626,1992.

[44] C.H. Kim and I.J. Ha, "A New Approach to Feedback-Linearizing Control of Variable Reluctance Motors for Direct-Drive Applications," in *IEEE Transactions on Control Systems Technology*, vol. 4, no. 4, pp. 348-362, 1996.

[45] P. Pillay, Y. Liu, W. Cai, and T. Sebastian, "Multiphase operation of Switched Reluctance Motor Drives," in *Rec. of IEEE Industry Applications Society Annual Meeting*, pp. 310-317, 1997.

[46] H.S. Lim, D.G. Roberson, N.S. Lobo and R. Krishnan, "Novel flux linkage control of switched reluctance motor drives using observer and neural network-based correction methods," in *IEEE Industrial Electronics 32nd Annual Conference,* pp. 1431 – 1436, November 2005.

[47] H.K. Bae and R. Krishnan, "A study of current controllers and development of a novel current controller for high performance SRM drives**,"** in *Conf. Rec. of IEEE Industry Applications Conference,* vol.1*,* pp. 68-75, October 1996

[48] H.K. Bae and R. Krishnan, **"**A novel approach to control of switched reluctance motors considering mutual inductance," in *IEEE Industrial Electronics 26th Annual Conference,* vol.1, pp. 369-374, October 2000.

[49] Z. Lin, D. S. Reay, B. W. Williams, X. He, "High performance current control for switched reluctance motors with on-line modelling," in *IEEE 35th Annual Power Electronics Specialists Conference,* vol. 2, pp. 1246- 1251, June 2004

[50] Guo Wei; Zhan Qianghua; Ma Zhiyuan," A new current control mode for switched reluctance motor drive with DSP controller", in *Proc. of IEEE Fifth International Conference on Electrical Machines and Systems,* vol. 2, pp. 1017-1021, August 2001

[51] R. Krishnan, R. Arumugam, and J.F. Lindsay, "Design procedure for switched-reluctance motors," in *IEEE Trans. on Industry Applications*, vol. 24, no. 3, pp. 456-461, May/June 1988.

[52] K.-S. Ha; S.-G. Oh, B. MacCleery, and R. Krishnan, "An automated reconfigurable FPGA-based magnetic characterization of switched reluctance machines," in *Proc. of the IEEE International Symposium on Industrial Electronics*, vol. 2, pp. 839 – 844, June 2005.

[53] P.C. Krause, *Analysis of Electric Machinery*, McGraw-Hill, 1986.

[54] M. Barnes and C. Pollock, "Power Electronic Converters for Switched Reluctance Drives," in *IEEE Transactions on Power Electronics*, vol. 13, no. 6, pp. 1100-1111, 1998.

[55] R. D. Peters, *Ideal Lift Kinematics: Formula for the Equations of Motion of a Lift*, Brunel Univ., 1993.

[56] Chen Xinkai, S. Komada, and T. Fukuda, " Design of a nonlinear disturbance observer,' in IEEE Transactions on Industrial Electronics, vol. 47, pp. 429 – 437, April 2000.

[57] Yoon-seok Han, Young-seok Kim, Jung-soo Choi, and Ho-whan Woo, " The position control of induction motors using the binary disturbance observer," in *IEEE Industrial Electronics 24th Annual Conference*, vol. 3, September 1998, pp. 1457 – 1463.

[58] W.–T. Su and C. –M. Liaw, "Adaptive Positioning Control for a LPMSM Drive Based on Adapted Inverse Model and Robust Disturbance Observer" in *IEEE Transactions on Power Electronics*, vol. 21, March 2006, pp. 505 – 517.

[59] Jong Sun Ko, Young Seok Jung, Sung Kwun Kim, and Myung Joong Youn, "MRAC load torque observer for position control of brushless DC motor," in *Proc. of International Conference on Power Electronics and Drive Systems*, vol. 2, February 1995, pp. 622 – 627.

[60] S. Komada, M. Ishida, K. Ohnishi, and T. Hori, **"**Disturbance observer-based motion control of direct drive motors," in *IEEE Transactions on Energy Conversion*, vol. 6, September 1991, pp. 553 – 559.

[61] Bong Keun Kim; Wan Kyun Chung, "Advanced disturbance observer design for mechanical positioning systems," in *IEEE Transactions on Industrial Electronics*, vol. 50, December 2003, pp. 1207 – 1216.

[62] Kok Kiong Tan, Tong Heng Lee; Hui Fang Dou, Shok Jun Chin, and Shao Zhao, "Precision motion control with disturbance observer for pulsewidth-modulated-driven permanent-magnet linear motors," in *IEEE Transactions on Magnetics*, vol. 39, May 2003, pp. 1813 – 1818.

[63] J. –Q. Han, "" The extended state observer of a class of uncertain systems," Control Decis., vol. 10, 1995, pp. 85-88.

[64] Zeng-Guang Hou; Yuancan Huang; Jing-Qing Han, "Active noise cancellation with a nonlinear control mechanism," in *Proc. of IEEE Conference on Decision and Control*, vol. 2, December 1998. pp. 1577 – 1578.

[65] Zhiqiang Gao, Yi Huang, and Jingqing Han, "An alternative paradigm for control system design," in *proc. of IEEE Conference on Decision and Control*, vol. 5, December 2001. pp. 4578 – 4585.

[66] Zhiqiang Gao, Shaohua Hu, and Fangjun Jiang, "A novel motion control design approach based on active disturbance rejection," in *proc. of IEEE Conference on Decision and Control*, vol. 5, December 2001, pp. 4877 – 4882.

[67] Weiwen Wang; Zhiqiang Gao, "A comparison study of advanced state observer design techniques," in *proc. of American Control Conference*, vol. 6, June 2003, pp. 4754 – 4759.

[68] Jianbo Su; Hongyu Ma; Wenbin Qiu; Yugeng Xi, "Task-independent robotic uncalibrated hand-eye coordination based on the extended state observer," in *IEEE Transactions on Systems, Man and Cybernetics, Part B*, vol. 34, August 2004, pp. 1917 – 1922.

[69] F. Jiang and Z. Gao, "An adaptive nonlinear filter approach to Vehicle Velocity Estimation for ABS", *IEEE CCA/CACSD conference*, September 2000.

[70] Ping Dong, Gang-jian Ye, Jie Wu, Jin-Ming Yang, and Yuan-Rui Chen, "Auto-disturbance rejection controller in the wind energy conversion system," in International Power Electronics and Motion Control Conference (IPEMC), vol. 2, August 2004, pp. 878 – 881.

[71] Kai Sun, Lipei Huang, and Guang Feng, "Speed control of induction motors using a nonlinear auto-disturbance rejection controller," in *IEEE Industrial Electronics 27th Annual Conference*, vol. 2, November 2001, pp. 1412 – 1416.

[72] Jinming Yang, N. C. Cheung, and Jie Wu, "The auto-disturbance rejection controller for speed regulation in permanent-magnet linear motors," in *IEEE Industrial Electronics 30th Annual Conference*, vol. 2, November 2004, pp. 1123 – 1127.

[73] Chunlin Lei, Jie Wu, Yuanrui Chen, and Jinming Yang, "Permanent-magnet linear motor control system based on the auto-disturbance-rejection controller (ADRC)," in *Sixth International Conference on Electrical Machines and Systems (ICEMS)*, vol. 1, November 2003, pp. 62 – 65.

[74] J.F. Pan, N. C. Cheung, and J. M. Yang, "Auto-disturbance rejection controller for novel planar switched reluctance motor," in *Proc. IEE Electric Power Applications*, vol. 153, March 2006, pp. 307 – 316.

[75] Li Qiao and Wu Jie, "Implementation of a new nonlinear controller for DC-DC converter using Matlab and DSPACE DSP," in *Proc. of the IEEE International Symposium on Industrial Electronics (ISIE)*, vol. 2, June 2005, pp. 621 – 625.

[76] Y.X. Su, B.Y. Duan, and Y.F. Zhang, "Robust precision motion control for AC servo system," in *Proc. of the 4th World Congress on Intelligent Control and Automation*, vol. 4, June 2002, pp. 3319 – 3323.

[77] Y.X. Su, B.Y. Duan, and Y. F. Zhang, "Auto disturbance rejection motion control for direct-drive motors," in *IEEE Industrial Electronics 28th Annual Conference*, vol. 3, November 2002, pp. 2073 - 2078.

[78] Xizhe Liu, Jie Wu, and Chunlin Lei, "Speed distinguish and control of PMSLM using expand state observer," in *Proc. of the 5th World Congress on Intelligent Control and Automation*, vol. 5, June 2004, pp. 4568 – 4572.

[79] Zhiqiang Gao; Yi Huang; Jingqing Han, "An alternative paradigm for control system design", in *Proc. of IEEE Conference on Decision and Control*, vol. 5, December 2001, pp. 4578 – 4585.

[80] Jean-Jacques E. Slotine and Weiping Li, "Applied Nonlinear Control," USA, Prentice Hall Inc., 1991.

[81] Riccardo Marino and Patrizio Tomei, "Nonlinear Control Design," USA, Prentice Hill Inc., 1995.

[82] M. Kristic, I. Kanellakopoulos, and P. Kokotovic, "Nonlinear and Adaptive Control Design," USA, John Wiley & Sons Inc., 1995.

[83] K.J. Astrom and T. Hagglund, “ PID Control,” The Control Handbook, Editor W.S. Levine, p. 198, CRC Press and IEEE Press, 1996.

[84] Y. Huang and J.-Q. Han, “Analysis and design for the second order nonlinear continuous extended states observer,” in Chinese Science Bulletin, vol. 45, no. 21, November 2000, pp. 1938-1944.

[85] Q. Liu, W. Shen, F. Wang, D. Borojevich, and V. Stefanovic, “On discussion of motor drive conducted EMI issues,” in Power Electronics and Motion Control Conference IPEMC, vol.3, pp.1515 – 1520, August 2004.

[86] S. Chen, “Generation and suppression of conducted EMI from inverter-fed motor drives”, in Conf. Rec. IEEE IAS Annu. Meeting, vol. 3, pp. 1583 – 1589, October 1999.

[87] A. L. Shestakov, “Dynamic error correction method,” in IEEE Trans. instrumentation and Measurement, vol. 45, pp. 250 – 255, February 1996.

[88] G. L. Skibinski, R. J. Kerkman, and D. Schlegel, **“**EMI emissions of modern PWM AC drives,” in IEEE Industry Applications Magazine, vol. 5, pp. 47 – 80, Nov.-Dec. 1999.

[89] S. Ogasawara, H. Ayano, and H. Akagi, **“**An active circuit for cancellation of common-mode voltage generated by a PWM inverter,” in IEEE Trans. Power Electronics, vol. 13, pp. 835-841, September 1998.

[90] Y.-C. Son and Seung-Ki Sul, “A new active common-mode EMI filter for PWM inverter,” IEEE Trans. Power Electronics, vol. 18, pp. 1309 – 1314, November 2003.

[91] Mutoh, N.; Nakanishi, M.; Kanesaki, M.; Nakashima, J. “EMI noise control methods suitable for electric vehicle drive systems,” in IEEE Trans. Electromagnetic Compatibility, vol. 47, pp. 930-937, November 2005.

[92] D. Massicotte, R. Z. Morawski, and A. Barwicz, “Incorporation of a positivity constraint into a Kalman-filter-based algorithm for correction of spectrometric data,” in IEEE Trans. instrumentation and Measurement, vol. 44, pp. 2-7, June 1994.

[93] I. Boldea and S. A. Nasar, “Linear Motion Electromagnetic Devices,” USA, Taylor & Francis, 2001.

VITA

Mr. Hong Sun Lim was born in Korea in 1973. He received the B.S. in electrical engineering department from Korea University and M.S. degree in electrical engineering from Seoul National University, Seoul, Korea, in 1996 and 1998, respectively. He joined the Ph.D. program in the Bradley Department of Electrical and Computer engineering at Virginia Polytechnic Institute and State University (Virginia Tech), Blacksburg, in fall 2003.

From 1998 to 2003, he worked with the Power System R&D Center, Samsung Techwin Ltd., Changwon, Korea, on design and development of electronic gas turbine engine controllers based on DSP. He also designed and developed a gas turbine engine simulator using Data Acquisition Systems (DAS). His interests are analysis, design, and control of linear switched reluctance motor actuation systems, propulsion systems, ac machine drives, power electronics, DSP-based motion control, and nonlinear system control.